Syracuse University

SURFACE at Syracuse University

Dissertations - ALL

SURFACE at Syracuse University

Summer 8-27-2021

Multimode Circuit Quantum Electrodynamics With Superconducting Metamaterial Resonators

. Indrajeet

Syracuse University

Follow this and additional works at: https://surface.syr.edu/etd

Part of the Physics Commons

Recommended Citation

Indrajeet, ., "Multimode Circuit Quantum Electrodynamics With Superconducting Metamaterial Resonators" (2021). *Dissertations - ALL*. 1397.
https://surface.syr.edu/etd/1397

This Dissertation is brought to you for free and open access by the SURFACE at Syracuse University at SURFACE at Syracuse University. It has been accepted for inclusion in Dissertations - ALL by an authorized administrator of SURFACE at Syracuse University. For more information, please contact surface@syr.edu.

ABSTRACT

Superconducting devices in circuit quantum electrodynamics (cQED) systems are one of the leading approaches for realizing scalable quantum information processors. The combination of cQED architectures with multimode resonator systems can provide a flexible platform for performing analog quantum simulations, storing quantum information, and generating complex entangled states. Metamaterial resonant structures made from arrays of superconducting lumped circuit elements can exhibit microwave mode spectra with left-handed dispersion, resulting in a high density of modes in the same frequency range where superconducting qubits are typically operated, as well as a bandgap at lower frequencies that extends down to dc. In this thesis, we present a brief review of the design, fabrication, and circuit properties of superconducting metamaterial resonators. Through a series of low-temperature measurements, we study the coupling of a flux-tunable transmon qubit to a dense spectrum of microwave modes generated by a superconducting metamaterial resonator. We measure the interaction between the transmon and metamaterial by both direct microwave transmission through the metamaterial resonator and qubit spectroscopy and manipulation through a separate readout cavity. We study the qubit decay and decoherence as a function of frequency in the presence of the dense mode spectrum. We also investigate the ac Stark shift of the qubit as the photon number in the various metamaterial modes is varied. Additionally, we compare these measurements with analytical and circuit simulation results.

MULTIMODE CIRCUIT QUANTUM ELECTRODYNAMICS WITH SUPERCONDUCTING METAMATERIAL RESONATORS

By

Indrajeet

BS-MS, Indian Institute of Science Education and Research (IISER) Mohali, 2014

Dissertation
Submitted in Partial Fulfillment of the Requirements
for the degree of
Doctor of Philosophy in Physics

Syracuse University
August 2021

Copyright © 2021 Indrajeet
All rights reserved.

ACKNOWLEDGMENTS

I would like to first thank my advisor, Prof. Britton Plourde for being an ideal advisor. Despite the challenges due to Covid pandemic in last mile, this PhD journey has successfully come to fruition only due to his constant support and mentorship. No matter if a research topic being discussed is fundamental or advanced, he always patiently answers all the questions.

I thank former group members Dr. Haozhi Wang and Dr. Matthew Hutchings, who showed and trained me on all the different aspects of the metamaterial project. Dr. JJ Nelson also helped with the fabrication of the devices. I thank my colleagues Tianna McBroom, Bradley Cole and Dr. Jaseung Ku who are currently working on the next phase of the metamaterial project. I also extend many thanks to rest of my colleagues Kenneth Dodge, Yebin Liu, Dr. Caleb Howington, Michael Senatore and Dr. Daniela Bogorin with whom I have shared the Physics sub-basement all these years. Without their help, it would have been challenging to learn and perform so many tasks like keeping the wet dilution refrigerator cold for several months continuously. I also thank Dr. Matt LaHaye, Dr. Yu Hao, Dr. Frank Wilhelm and Dr. Bruno Taketani for important discussions and analysis of the measurements. I appreciate all the help provided by CNF and Machine shop staff.

I thank my friends Steven and Frank who helped me navigate through the first two years of coursework and later forcing me to get out of sub-basement to get fresh air regularly. I am grateful for my friends Amrish, Rupan, Selma and Nejla for their support outside of my research, while I lived in Syracuse.

Lastly and most importantly, I thank my family for their constant love and support during the PhD, even when separated by thousands of miles. I wish you all the best.

Contents

List of Tables **viii**

List of Figures **xviii**

xix

1 Introduction **1**

2 Background: Superconducting Qubits and Circuit Quantum Electrodynamics **4**

2.1 Qubits 4

2.2 Superconducting qubits 5

2.2.1 Josephson junctions 5

2.2.2 Transmons 7

2.3 Circuit Quantum Electrodynamics 8

2.3.1 Jaynes-Cummings Hamiltonian 8

2.4 Superconducting cavities 10

2.4.1 Transmission line half-wave resonator 10

2.5 Qubit decoherence 14

3 Metamaterial transmission lines **15**

3.1 Metamaterials 15

3.2 Left handed transmission lines (LHTL) 17

3.2.1 LHTL: circuit model 17

3.2.2 Stray reactances in LHTL 21

3.3 Left-handed transmission line resonator 23

    3.3.1 Ideal LHTL resonator 24
    3.3.2 Effects of stray reactance: LHRH resonator 25
    3.3.3 LHRH impedance and transmission $S_{21}(\omega)$ 25
    3.3.4 Coupling quality factor for discrete transmission line resonators 27
  3.4 Coupling a transmon qubit to a metamaterial resonator 29

4 Device Design 33
  4.1 LHTL Design 33
  4.2 Qubit design 36
  4.3 Readout resonator 37
  4.4 Metamaterial coupled to a transmon 38
  4.5 Fabrication Details 41

5 LHTL resonator measurements 42
  5.1 Measurement setup 42
  5.2 Mode structure of a LHTL resonator 44
  5.3 Coupling and Internal Losses 46
  5.4 LSM imaging of mode structure 49

6 Measurements of a qubit coupled to a metamaterial resonator 54
  6.1 Measurement setup 54
  6.2 Mode structure of hybrid LHTL-RHTL metamaterial resonators . . . 57
  6.3 Probing metamaterial modes coupled to a qubit 61
  6.4 Dispersive readout of the qubit 66
  6.5 Purcell losses in a multimode enviroment 68
  6.6 Qubit decoherence 70
  6.7 Stark shift measurements 71

7 Numerical Simulations 75
  7.1 Numerical simulations of mode structure of metamaterials 76
    7.1.1 Effects of staggered inductor layout 76
    7.1.2 Effects of imperfect grounding 78
  7.2 Extraction of qubit-metamaterial mode couplings from spectra . . . 79
  7.3 Calculation of qubit-metamaterial mode couplings 81

7.4 Approaches for increasing qubit-metamaterial mode couplings 83
7.5 Calculation of Purcell loss 87

8 Ongoing and Future Work **91**
8.1 Next-generation devices and preliminary results 91
8.2 Ring resonators and preliminary results 93
8.3 Outlook 95

Appendices **96**

A Fabrication **97**
A.1 Fabrication of Device A 97
A.2 Fabrication of Device B 98

List of Tables

1 Metamaterial parameters determined by finite element simulations of circuit layout. 34
2 Qubit and readout resonator design parameters. 38
3 Qubit and readout resonator parameters. 65
4 Modified metamaterial parameters for hypothetical device with enhanced coupling strength used in AWR simulation. 84

List of Figures

1 (a) Circuit diagram of a quantum harmonic oscillator represented as a parallel LC oscillator; (b) Energy potential and energy levels for a quantum harmonic oscillator; (c) circuit representation of a transmon qubit. (d) The Josephson inductance reshapes the quadratic energy potential (dashed blue) into cosine (solid red), resulting in nonequidistant energy levels. Figure concept adapted from Ref. [43]. 6

2 A plot of the avoided crossing in the transition frequency from the ground state in the one-excitation manifold. The dashed lines show the uncoupled resonator frequency, ω_c (black dashed line) and qubit frequency, ω_q (green dashed line). Qubit-cavity hybridized levels shown in red and blue. 9

3 CPW geometry: (a) Top view of a CPW with center conductor width w and slot width s; (b) side view of a CPW with film thickness of t on top of a substrate with thickness of h. 11

4 Circuit schematic of a TL half-wave resonator with external power source and load. C_c is the input/output coupling capacitance, and R_0 is the source/load resistance of the external circuitry. 12

5 Diagram of a loaded parallel LCR resonator circuit. 13

6 A diagram of of how EM waves refracts between two media with the incident wave (red $\vec{k}$ and $\vec{S}$), the reflected wave (blue $\vec{k'}$ and $\vec{S'}$) and the refracted wave (orange $\vec{k''}$ and $\vec{S''}$). (a) permittivity ϵ_2 and permeability μ_2 for medium 2 are both positive. (b) permittivity ϵ_2 and permeability μ_2 for medium 2 are both negative. Figure adapted from Ref. [59]. . 16

7 LHTL circuit model: (a) array of series capacitors C_l with shunt inductors L_l to ground; (b) definition of current and voltage in the LHTL at cell m. 18

8 Circuit diagram of discrete right-handed transmission line. 20

9 Dispersion relation of ideal LHTL (blue solid line) with $\omega_{IR}/2\pi = 6$ GHz. Due to its left-handed nature, k is negative, but here we plot the absolute value of k. Dispersion relation of a discrete RHTL (red solid line). 21

10 (a) The circuit diagram of a LHRH transmission line, which is the LHTL with stray reactances included. (b) Voltage and current in a unit cell. 21

11 Calculated dispersion relations for ideal LHTL (dashed blue line) [Eq. 3.15] and composite LHTL (solid black line) [Eq. 3.29] using circuit parameters described in text. Figure adapted from Ref. [39]. 22

12 (a) Schematic of an ideal LHTL terminated by coupling capacitors C_C. (b) Dispersion relation of a LHTL resonator with normalized wavenumber. The blue points here correspond to the resonant modes where $k\Delta x = n\pi/N$, while the solid black line is the dispersion relation calculated using (Eq. 3.15) for the parameters N =42, C_l =250 fF and L_l=0.625 nH. Figure adapted from Ref. [59]. 24

13 (a) Schematic of a composite LHRH resonator with stray reactances including coupling capacitances C_c at each end. (b) Plot of mode frequencies vs. wave number computed for for a composite LHRH resonaotr with 42 cells . The solid line is the dispersion relation obtained from [Eq. (3.29)] using circuit parameters described in text. Figure adapted from Ref. [39]. 26

14 The circuit diagram of a lossless LHRH transmission line with load impedance Z_l on the right end. Figure adapted from Ref. [39]. . . . 27

15 $S_{21}(f)$ calculated for the $n = 23$ mode of a 42-cell LHRH metamaterial resonator using Eq. (3.34) (solid red line) and simulated using AWR Microwave Office (blue points). Unit cell parameters are: $C_l = 266$ fF, $L_L = 0.6$ nH, $C_r = 21.806$ fF and $L_r = 0.595$ nH, chosen based on the discussion in Chapter 4. Figure taken from Ref. [39]. 28

16 Coupling loss comparison for an LHTL resonator for analytic expression from Eq. (3.35)(Solid black line), AWR Microwave Office circuit simulation (Red stars), and linewidth extraction for $S_{21}(\omega)$ expression from Eq. (3.34) (blue circles). The parameters for the LHTL are: $C = 250$ fF, $L = 0.625$ nH, $C_c = 10$ fF, $N = 40$. Figure taken from Ref. [39]. 29

17 Coupling loss comparison between calculation for an ideal LHTL resonator using Eq. (3.35) with an LHRH resonator with non-zero stray reactances from linewidth extractions using Eq. (3.34). The parameters for the LHTL are: $C = 250$ fF, $L = 0.625$ nH, $C_c = 10$ fF, $N = 40$ $C_r = 16.211389$ fF, $L_r = 0.0334947$ nH, corresponding to self resonance frequencies of 50 GHz and 55 GHz. Figure taken from Ref. [39]. 30

18 LHTL coupled to a continous RHL. Qubit can be coupled near the end of RHTL. Figure adapted from Ref. [33]. 31

19 The standing wave patterns of the first three modes of a hybrid transmission line cavity counting from low frequency end. Figure taken from Ref. [33]. 31

20 Optical micrographs of LHTL resonator device (Device A): (a) zoomed-out image of entire chip, (b) input coupling capacitor Cc and first few unit cells, (c) meanderline inductor of first unit cell, (d) detail of input coupling capacitor and connection between inductor and capacitor of first unit cell, (e) interdigitated capacitors in several unit cells, (f) detail of interdigitated capacitor. 35

21 Layout of the transmon used in the device showing the shunt capacitor pads (blue) and coupler to the metamaterial(yellow) and the coupler to readout resonator (green) and ground plane(red) 37

22 Circuit schematic of the device. 38

23 (a-g) Optical micrographs of metamaterial resonator device B: (a) zoomed-out image of entire chip, (b) section of metamaterial resonator containing several unit cells of inductors and capacitors, (c) detail of interdigitated capacitor, (d) detail of meander-line inductor, (e) transmon qubit with coupling capacitors to metamaterial resonator and readout resonator,(f) SQUID loop of the transmon, (g) Scanning electron microscope (SEM) image of one of the transmon junctions. . . . 39

24 Transmission spectrum calculated from circuit simulation using AWR for a hybrid LHTL-RHTL resonator with parameters of the designed device B. 40

25 Optical micrographs of metamaterial resonator device with inductors on one side of the LHTL (Device C). 41

26 Schematic of a two port device under test (DUT). 43

27 (a) Zoomed-out image of the chip fitting in the sample holder and the wirebonds; (b) the entire sample holder with chip bonded in place and input/output connections marked. 44

28 Transmission measurement setup including the wiring inside the ADR. 45

29 (a) Measurements of the magnitude of the microwave transmission $|S_{21}(f)|$ on the ADR at two different temperatures: 65 mK (solid black line); 3 K (blue dashed line); Sonnet simulation (red dashed line) offset by 20 dB; (b) an enlarged plot in the vicinity of $n = 38$ mode near 5.41 GHz. Figure taken from Ref [39]. 46

30 (a) Plot of mode frequency vs. normalized wavenumber for ADR measurements, LSM images, Sonnet simulations; the solid black curve corresponds to dispersion relation of Eq. (3.29). (b) Closeup of behavior near $\omega_{IR}/2\pi$. Figure taken from Ref [39]. 47

31 (a) Comparison of internal loss and coupling loss extracted from measured $S_{21}(f)$; (b) The external loss plot on a log scale for the measurement at 65 mK compared with AWR simulation, Sonnet simulations of both staggered and non-staggered inductor configuration, and theoretical dependence calculated from Eq. (5.4) Figure taken from Ref [39]. 48

32 LSM reflectivity image with the arrow indicating the direction of 1D line scans. (b) Microwave transmission (not normalized) $|S_{21}(f)|$ measured on LSM. (c) Average LSM photoresponse $\overline{\mathscr{R}}(y_0, f)$ along 1D line scans. (d) 1D line scans $\mathscr{R}(x, y_0, f)$ vs. frequency; dashed horizontal lines indicate location of input and output coupling capacitors. Figure taken from Ref [39]. 50

33 (a) LSM photoresponse for mode 23 with the arrow indicating the location of subsequent line cut. Bright (dark) regions correspond to large (small) PR signal. (b) Plot of the square root of LSM photoresponse signal along line cut. (c) Standing-wave pattern of voltage across capacitors computed with Eq. (E3) in Ref. [39] for mode 23 of a 42-cell LHTL resonator. Figure taken from Ref [39]. 51

34 Array of LSM images of metamaterial for different modes, labeled by mode number and frequency. Bright (dark) regions correspond to large (small) PR signal. Amplitudes of photoresponse signal are normalized for best contrast. Figure taken from Ref [39]. 53

35 (a) Aluminum sample box with the device wirebonded in the center. (b) Top view of the lid of the sample box; SMA port is used to connect the DC bias of the superconducting coil. (c) Bottom view of the lid. In the center superconducting coil can be seen which is made from 150 turns of NbTi wire. 55

36 Wiring inside the dilution refrigerator. The input for metamaterial resonator and input resonator, each go thorough 50 dB of attenuation and a low pass filter. The output signal from the device go through a low pass filter, a microwave switch, isolators and a HEMT amplifier mounted at 4 K stage. 56

37 Transmission measurement for initial characterization of device spectra setup using a network analyzer. 57

38 Measurement setup for qubit spectroscopy and characterization. . . . 58

39 Measured transmission spectrum (black line) for Device B compared with spectrum from circuit simulation using AWR (blue dashed line, with -50 dB for clarity). Figure adapted from Ref. [97]. 59

40 Dispersion relation obtained from S_{21} measurement of Device B compared with dispersion obtained from AWR simualtion with same parameters. 59

41 Measured total quality factor of metamaterial modes as function of frequency. The presence of the RHTL segment that is used to couple the metamaterial to the qubit results in the non-monotonic behavior of the mode quality factor vs. frequency through the variation in the standing-wave pattern in the RHTL portion with frequency; by contrast, a simple LHTL resonator exhibits a monotonic decrease in quality factor for increasing frequency (Fig. 31). Figure taken from Ref. [97]. 60

42 Density plot of magnitude of transmission through metamaterial resonator vs. qubit flux bias, showing vacuum Rabi splittngs for all of the modes that the qubit tunes through. Dashed line indicates flux tuning of bare transmon energy band from fits to splitting location. (Insets) closeup of splittings and fits for 5.81 GHz and 8.52 GHz modes. Figure taken from Ref. [97]. 61

43 Detail of splittings for four adjacent modes between 7.1 and 7.9 GHz. Figure taken from Ref. [97]. 62

44 (a) Extracted coupling strength between qubit and each metamaterial mode vs. frequency. (b) Simulated coupling strengths vs. frequency using AWR Microwave Office and circuit model approach described in text. Figure taken from Ref. [97]. 63

45 Pulse sequences used for different qubit characterization experiments. 65

46 Density plot of magnitude of transmission through readout resonator vs. qubit flux bias. Red (blue) circle are the extracted resonance frequencies extracted from Lorentzian fit of 1D vertical slices of the density plot. Red and blue dashed lines are the eigensolutions of the Hamiltonian of a qubit coupled to one mode of a resonator. The faint blue feature shows up due to the leakage of lower sideband from the mixer used for heterodyne detection. 66

47 (a) Density plot of magnitude of transmission through metamaterial resonator vs. qubit flux bias in vicinity of upper sweetspot. (b) Spectroscopy of qubit 0-1 transition vs. flux bias near the upper sweetspot measured using readout resonator. (c) Rabi spectroscopy of qubit for flux bias near upper sweet spot, around 9.235 GHz, measured using readout resonator. Figure taken from Ref. [97]. 67

48 Plots of two example measurements of qubit relaxation measured for a bias point below f_{IR} of the metamaterial and a bias point in between two modes at higher frequencies. Figure taken from Ref. [97]. 68

49 (a) T_1 vs. frequency measured over span of 6.5 GHz. Vertical dashed lines indicate the loaction of the two T_1 decay curves shown in Fig. 48. (b) Transmission spectrum of metamaterial resonator for comparison with structure in $T_1(f)$ plot. (c, d) zoomed-in $T_1(f)$ plots of data from (a) with red vertical dashed lines indicating location of metamaterial resonator modes. (e) Calculated $T_1(f)$ from multi-mode Purcell loss simulation of qubit coupled to metamaterial resonator. Figure adapted from Ref. [97]. 69

50 (a) Qubit T_2 and T_2^* measured as function of flux. (b) Qubit dephasing measured as a function of D_Φ. 71

51 (a-f) Stark shifts of qubit transition through driving of 6 different metamaterial modes at a range of microwave powers for a flux bias corresponding to the unshifted qubit transition at 6.275 GHz; Stark shift theoretical curves shown by blue dashed lines. For the 6 plots, 0 dB attenuation corresponds to a power at the chip of (a) -86 dBm, (b) -126 dBm, (c) -128 dBm, (d) -123 dBm, (e) -121 dBm, and (f) -113 dBm. (g) $|S_{21}(f)|$ measured through metamaterial to indicate the 6 modes driven in (a-f) (blue dots and dotted lines) and the bias point of the qubit (red dashed line). Plots of qubit spectroscopy frequency vs. Stark drive frequency for fixed power for (h) mode near 6.003 GHz at -129 dBm, (i) mode near 6.588 GHz at -122 dBm; metamaterial mode near 6.22 GHz visible as a faint, sharp line near bottom of plots. Figure taken from Ref. [97]. 72

52 Extracted Stark shifts in qubit transtion frequency from Fig. 51(a-f) plotted vs. mean photon number for each of the 6 metamaterial modes, as described in text. Figure taken from Ref. [97]. 74
53 Measured transmission spectrum (black line) for Device B (LHRH hybrid metamaterial with non staggered inductors) compared with spectrum from circuit simulation using AWR (blue dashed line, with -50 dB offset for clarity). Figure adapted from Ref. [97]. 76
54 Sonnet simulations of $S_{21}(f)$ for non-staggered (orange, with -40 dB offset for clarity) and staggered (blue) inductor layouts. Figure taken from Ref. [39]. 77
55 Measurement spectrum of Device C that has all inductors on one side of the capacitors that form the LHTL. 77
56 Sonnet simulations for different grounding configurations for a 42-cell LHTL resonator for (a) resonance frequency vs n, (b) coupling loss $1/Q_c$ vs n. Figure taken from Ref. [39]. 79
57 AWR circuit model of Device B. 81
58 Simulated g_i from AWR/circuit model extended out to higher frequency for a hypothetical qubit with higher upper sweetspot. The slight deviation at 7.5 GHz and 15 GHz is due to the mode frequency approaching fundamental and first harmonic modes of readout resonator. Figure adapted from Ref. [97]. 82
59 Coupling strength of four metamaterial modes to the qubit as function of the position on the RHTL where the qubit is coupled. The total length of RHTL section is 6 mm. The coupling strength reduces to zero at different locations for different modes due to variations in the position where the standing-wave amplitude for the modes corresponds to a node. 85

60 Coupling strength of six metamaterial modes to the qubit as function of the length of the RHTL section. The total length of RHTL section is 1 mm longer than l_a since it also includes the section from the location where the qubit is coupled to the output coupling capacitor C_{cM}^{out}. The maximum of coupling strength occurs at different lengths of RHTL for different modes due to variation of standing-wave amplitude for the modes. 86

61 Numerical solutions for a transmon coupled to four modes with 100 MHz intermode spacing; bare mode frequencies are indicated by horizontal dashed lines. Nearly vertical red dashed line corresponds to bare transmon frequency. Label at the top of each plot indicates the coupling strength $g_i/2\pi$ between each of the four modes and the transmon. Figure adapted from from Ref. [97]. 87

62 Simulation of hypothetical qubit-metamaterial device to achieve superstrong coupling through AWR circuit simulation of device described in text using parameters in Table 4 and numerical solution to Hamiltonian (blue dashed lines) with adjusted coupling strength values to match features in AWR simulation. Black dotted line corresponds to bare qubit transition frequency. The brown horizontal dashed-dotted lines show the bare frequencies for each of the four modes, 7.91 GHz, 8.04 GHz, 8.17 GHz, and 8.31 GHz, with extracted $g_i/2\pi$ values 220 MHz, 193 MHz, 180 MHz, and 178 MHz, respectively. Figure adapted from from Ref. [97]. 88

63 The layout of next-generation qubit-metamaterial device and a few optical images for some of the sections of chip. The zoomed-in image on the right shows the qubit pockets and shunt capacitor pads for the two qubits. The top qubit is more strongly coupled to the metamaterial, while the bottom qubit is weakly coupled to the modes and can be used as a probe. Figure taken from Ref. [112]. 91

64 Vacuum Rabi splittings for metmaterial modes (a) 8.26 GHz, (b) 8.1 GHz, and (c) 7.9 GHz. The black dashed line of each plot correspond to the solutions of the Hamiltonian for one mode coupled to one qubit, as described in Sec.7.2. The extracted coupling strength values for the modes are 74 MHz, 54 MHz and 86 MHz respectively. Figure adapted from Ref. [112] 92

65 (a) Figure shows a layout for 24 cell metamaterial ring resonator. The diameter of the ring is 1.3 mm. Based on Q3D simulations, each cell is made from a series capacitor C_l=200 fF and L_l=0.5 nH (b) A circuit representation of a metamaterial resonator with three qubits coupled around the ring. 94

66 Dispersion relation for a metamterial ring resonator simulated using AWR. Between 8 and 10 GHz, where the band flattens, we can see 5 metamaterial modes. 94

Chapter 1

Introduction

Digital electronic computers have made huge advancements since their early development in 1940s [1] and have transformed modern life. The advances in computational power have enabled dramatic developments in machine learning through the training of deep neural networks [2]. This progress in computing power is a consequence of doubling of transistor count density every two years, which has held true for more than five decades, as described by Moore's Law [3]. The smallest components of the latest computers are now only a few nanometers wide [4, 5] and are hitting the physical limits of fabrication. Undesired quantum effects which start to dominate at these scales also present a challenge to make devices any smaller. However, limitations to increase transistor density is not the only motivation for finding alternative computational approaches. For certain classes of problems, many of them with critical applications, such as hard optimization problems, database searches and modeling of electronic structure of molecules, the algorithms have exponential complexity on classical computers, that is, the resources needed to solve the problems grow exponentially with the number of inputs.

Another approach for solving these complex problems is to make a quantum computer, that harnesses the power of quantum mechanics in computation. The phenomena inherent to quantum systems, such as superposition of states and entanglement of quantum objects, can be exploited to reduce the complexity of of certain computational problems from exponential to polynomial time [6]. Similar to a classical bit, the smallest unit of digital computing, a quantum computer uses a quantum bit, or qubit. A qubit can be physically implemented with various kinds of quantum systems, such as superconducting circuits [7, 8, 9], ion traps [10, 11], photons [12, 13, 14], neutral atoms [15, 16, 17], semiconductors [18, 19] and topological qubits [20, 21]. Each of these implementations has their advantages and disadvantages, and there has been significant progress across the field over the past two decades. As of now, superconducting qubits and trapped ions are clearly the most promising approaches for implementing a scalable quantum computer. Recently, quantum processors made from superconducting circuits [22, 23] consisting of more than 50 qubits have demonstrated quantum supremacy, that is, solving a specific problem orders of magnitude faster than an advanced classical supercomputer. Superconducting qubits are the focus of research in the largest industrial computing labs due to their fast gate times and high gate fidelities, which are approaching the threshold needed for implementing quantum error correction [24]. Such systems require similar fabrication technologies that are used in semiconductor based classical computers computers that have been developed over several decades. As a result, one can envision a scalable superconducting quantum computer. However, understanding and eliminating the decoherence in superconducting qubits still remains the biggest challenge in this system and there is still a long way to go before there are universal fault-tolerant quantum computers. Noisy Intermediate-Scale Quantum (NISQ) [25] computers, which are composed of hundreds of noisy qubits, can still be used in near term to gain quantum advantage for optimization problems [26, 27], simulation of the quantum systems [17] and chemical properties of large molecules [28].

The framework for understanding superconducting quantum technology is provided by circuit quantum electrodynamics (cQED), an analogue of cavity quantum electrodynamics [29]. Cavity quantum electrodynamics is used to describe the dynamics of a coupled atom and photon in an optical cavity. Similarly, superconducting qubits behave as artificial atoms, and the resonant cavities host photonic microwave modes for coupling to the qubits. One of the advantages of cQED over cavity QED is that all the parameters of the system can be designed and incorporated into the device fabrication. This allows for artificial atoms with much larger dipole moments and cavities with reduced mode volume leading to the possibility of much stronger coupling strengths compared to atom-optical systems. This coupling strength can even be increased to the regime of ultra-strong coupling where the coupling strength is comparable to the transition energy scales of the cavity or qubits [30, 31]. In cQED, there is also the possibility of implementing cavities with multiple cavity modes. If these resonances can be made close together, it is possible to reach the superstrong coupling regime, where a single qubit can couple strongly to multiple modes simultaneously [32]. Superstrong coupling can have applications in analog quantum simulations [33, 34], quantum memory [35] and multi-partite entanglement [36].

Metamaterial transmission lines made from lumped circuit elements can be configured to produce left-handed dispersion relations, where the mode frequency is a falling function of wavenumber and low-frequency bandgaps [37, 38]. By forming resonators from such left-handed transmission lines, one can generate a high density of modes and just above an infrared cutoff frequency in the range where superconducting qubits typically operate [33]. This leads to the prospect of reaching the superstrong coupling regime of cQED in a compact physical footprint. Fabricating lumped elements, which make the metamaterial transmission line, using superconductors can thus provide a low-loss system compatible with circuit QED architectures [39].

In this thesis, I present a series of low-temperature measurements of a flux-tunable transmon qubit in the presence of multi-mode spectra generated using superconducting metamaterial resonators. In Chapter 2, I give a brief overview of superconducting qubits and circuit QED. In Chapter 3, I introduce the left-handed metamaterials, left-handed transmission lines and their properties and our scheme to couple the metamaterial resoanor to a qubit. The details of how the coupling scheme was implemented in our devices is explained in Chapter 4. Chapter 5 and Chapter 6 give details of the measurement and analysis. In Chapter 7, I describe details of the simulation tools we used to design our devices and improve the coupling in our future devices. Chapter 8 contains initial measurements of our improved devices.

Chapter 2

Background: Superconducting Qubits and Circuit Quantum Electrodynamics

In this chapter, I give a brief introduction to qubits, their physical implementation using superconducting circuits, circuit QED, and superconducting cavities.

2.1 Qubits

The smallest unit of classical information in a digital computer is a bit that can only be in one of two states – 0 or 1 – at any given instant. The analog of a bit in a quantum computer is called a quantum bit, or qubit. Physically, a qubit can be implemented in many ways, but the state of an ideal qubit can be an arbitrary coherent superposition of the basis states, and can be described mathematically as:

$$|\psi\rangle = \alpha|0\rangle + \beta|1\rangle, \tag{2.1}$$

where $|0\rangle$ and $|1\rangle$ are the eigenstates, and α and β are the complex probability amplitudes that must satisfy the constraint $|\alpha|^2 + |\beta|^2 = 1$. A qubit state can also be represented in terms of a polar angle θ and azimuthal angle ϕ on the Bloch sphere:

$$|\psi\rangle = \cos\frac{\theta}{2}|0\rangle + e^{i\phi}\sin\frac{\theta}{2}|1\rangle. \tag{2.2}$$

2.2 Superconducting qubits

Superconducting materials, when cooled below a critical temperature, T_c can conduct a dc electrical current without any resistance. This happens due to the condensation of pairs of conducting electrons, known as Cooper pairs, into a ground state with macroscopic phase coherence [40]. Therefore, superconducting materials are an obvious choice to make low-loss circuits, such as linear or non oscillators with high quality factors required for quantum architectures.

2.2.1 Josephson junctions

Linear circuit elements, such as inductors and capacitors, can be used to create harmonic oscillators [Fig. 1(a)], which have a quadratic potential energy curve. When quantized, such a harmonic potential results in equally spaced energy levels [Fig. 1(b)]. In order to use an oscillator as a qubit, the transition between two states has be addressed with a unique transition frequency. If the energy levels are equally spaced, when driven at the frequency corrosponding to this energy gap, the system can get excited to higher energy levels. So, it is necessary that the $0-1$ transition frequency is sufficiently different than from the $1-2$ transition frequency and other transitions. In order to form a nonlinear oscillator with unequal level spacings, one can use a Josephson junction as a nonlinear inductor [Fig. 1(c)]. For such a circuit, the transition between the ground energy level and first excited state can be uniquely addressed and thus can be used as the two states for a qubit [Fig. 1(d)]. A Josephson tunnel junction is formed from two superconducting layers separated by a thin insulating layer that is a few nm thick. The dynamics of a Josephson junction depend on two relations [41]:

$$V(t) = \frac{\Phi_0}{2\pi}\frac{\partial\phi(t)}{\partial t}, \tag{2.3}$$

$$I(t) = I_0 \sin\phi(t). \tag{2.4}$$

Here, $\Phi_0 \equiv h/2e$ is the magnetic flux quantum, V is the voltage across the junction, I is the current through the junction, I_0 is the critical current of the junction above which the junction becomes resistive, and ϕ is the phase difference of the superconducting wave function across the junction. We can use these two equations to calculate the inductance for a Josephson junction

$$L_J = \frac{V(t)}{\frac{dI(t)}{dt}} = \frac{\Phi_0}{2\pi I_0 \cos\phi(t)}, \tag{2.5}$$

and the Josephson energy

$$E_J = \frac{\Phi_0 I_0}{2\pi}. \tag{2.6}$$

The Josephson energy for a junction depends on the superconducting materials and tunnel barrier thickness and can be determined using Ambegaokar-Baratoff relation [42] :

$$E_J = \frac{\Phi_0 I_0}{2\pi} = \frac{\Phi_0 \Delta}{4eR}. \tag{2.7}$$

Here, Δ refers to the gap energy of the superconductor, and R is the normal-state junction resistance.

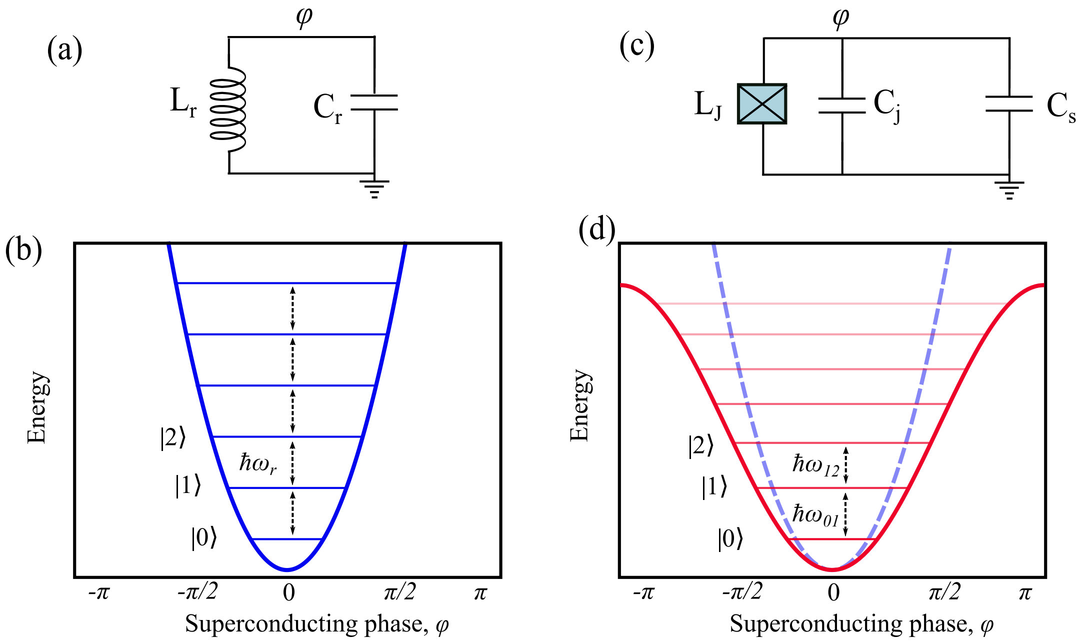
(a)
φ
L_r
C_r
(c)
φ
L_J
C_j
C_s
(b)
Energy
|2⟩
|1⟩
|0⟩
ħω_r
-π
-π/2
0
π/2
π
Superconducting phase, φ
(d)
Energy
|2⟩
|1⟩
|0⟩
ħω_12
ħω_01
-π
-π/2
0
π/2
π
Superconducting phase, φ

Figure 1: (a) Circuit diagram of a quantum harmonic oscillator represented as a parallel LC oscillator; (b) Energy potential and energy levels for a quantum harmonic oscillator; (c) circuit representation of a transmon qubit. (d) The Josephson inductance reshapes the quadratic energy potential (dashed blue) into cosine (solid red), resulting in nonequidistant energy levels. Figure concept adapted from Ref. [43].

2.2.2 Transmons

The nonlinear oscillator formed by a superconducting island connected to ground by a Josephson junction and a large shunt capacitance can be described by the following Hamiltonian [44]:

$$\hat{H} = 4E_C(\hat{n} - n_g)^2 - E_J \cos\hat{\phi}. \tag{2.8}$$

Here, $E_C = e^2/2C_\Sigma$ is the charging energy of the superconducting island, where C_Σ is the total capacitance of the island, $\hat{n}$ is the charge operator, $\hat{\phi}$ is the phase operator related by $[\hat{\phi}, \hat{n}] = i$, $n_g = Q_r/2e + C_g V_g/2e$ is the effective offset charge of the device, which depend on environment induced offset charge Q_r, the gate voltage V_g, and the gate capacitance C_g of a gate electrode. Such a circuit in the limit $E_J >> E_C$ is known as a transmon [44] qubit and qubit, and has a vanishingly small sensitivity to charge noise. The transmon design has been adopted by many labs throughout the community [45, 46, 47]. Two important quantities for any qubit are the qubit transition energy from the ground to first excited state ($\hbar\omega_{01}$) and the anharmoncity, which is the difference between the 0-1 and 1-2 transition energies. For a transmon qubit, the 0-1 transition frequency is given by [44]

$$\omega_Q/2\pi \equiv \omega_{01}/2\pi \sim (\sqrt{8E_J E_C} - E_C)/h, \tag{2.9}$$

and the anharmonicity $\alpha \simeq -E_C$. For a typical transmon, typical parameters are $\omega_Q/2\pi \sim 5$ GHz, $I_0 \sim 30$ nA, $C_\Sigma \sim 65$ fF and $E_J/E_C \sim 40$. It is also advantageous to have the capability to tune the qubit frequency. This can be done by splitting the junction into two smaller junctions connected in parallel forming a SQUID loop. This changes the Josephson part of the Hamiltonian to [44]:

$$\hat{E_J} = -E_{J\Sigma} \cos\left(\frac{\pi\Phi}{\Phi_0}\right) \sqrt{1 + d^2 \tan^2\left(\frac{\pi\Phi}{\Phi_0}\right)} \cos(\hat{\phi} - \phi_0), \tag{2.10}$$

where Φ is the flux applied through the SQUID loop, $\phi = (\phi_1 + \phi_2)/2$ with ϕ_1 and ϕ_2 the phase differences across each junction, $E_{J\Sigma} = E_{J1} + E_{J2}$, where E_{J1} and E_{J2} are the Josephpson energy for two junctions, the phase ϕ_0 can be found using $\tan\phi_0 = d\tan(\pi\Phi/\Phi_0)$, where d is the junction asymmetry $d \equiv \frac{E_{J2} - E_{J1}}{E_{J2} + E_{J1}}$. For junctions with equal Josephson energy ($d = 0$), the Josephson energy tunes to zero at odd half-integer multiples of Φ_0, leading to a maximum possible tuning range for ω_{01}. However, this can lead to excessive dephasing due to flux noise because of the large slope of the qubit transition energy with respect to flux. A balance between the tunabilty of the qubit frequency and flux noise insensitivity can be achieved through a careful choice of the asymmetry parameter d [48].

2.3 Circuit Quantum Electrodynamics

One of the most fundamental interactions that occurs in nature, namely that between light and matter, can be explained using cavity quantum electrodynamics. Practically, due to the small size of an atom, the interaction strength between an atom and a photon is rather weak and difficult to measure. By trapping the atom and photon in a cavity, the strength of this interaction can be increased.

2.3.1 Jaynes-Cummings Hamiltonian

In order to study the dynamics of a cavity and qubit, we will initially simplify the system by treating the qubit as an ideal two-level system and the cavity as a quantum harmonic oscillator. We will revisit the treatment where we include the higher energy levels of a superconducting qubit and a cavity later in Sec. 7.2. This simplified system can still provide a good physical intuition for the interaction between a qubit and cavity, and can be described by the Jaynes-Cummings Hamiltonian [49, 50]:

$$\hat{H} = \hbar\omega_c\hat{a}^\dagger\hat{a} + \frac{\hbar}{2}\omega_q\hat{\sigma}_z + \hbar g(\hat{a}\hat{\sigma}_+ + \hat{a}^\dagger\hat{\sigma}_-), \tag{2.11}$$

where ω_c and ω_q are cavity and qubit frequencies respectively, g is the coupling strength between the qubit and cavity, $\hat{\sigma_z}$ is the Pauli pseudospin z operator, $\hat{a}^\dagger$ and $\hat{a}$ are the raising and lowering operators for photon number in the cavity mode and $\hat{\sigma}_+$ and $\hat{\sigma}_-$ are the raising and lowering operators for the qubit. The Hilbert space for this Hamiltonian is spanned by states of the form:

$$|\psi\rangle = \sum_{n=0}^{\infty}\sum_{i\in\{g,e\}}\alpha_{n,i}|n,i\rangle, \tag{2.12}$$

where $|n\rangle$ is the Fock state of the cavity with n photons, and $|g\rangle$ and $|e\rangle$ are the ground and excited levels of the qubit, respectively.

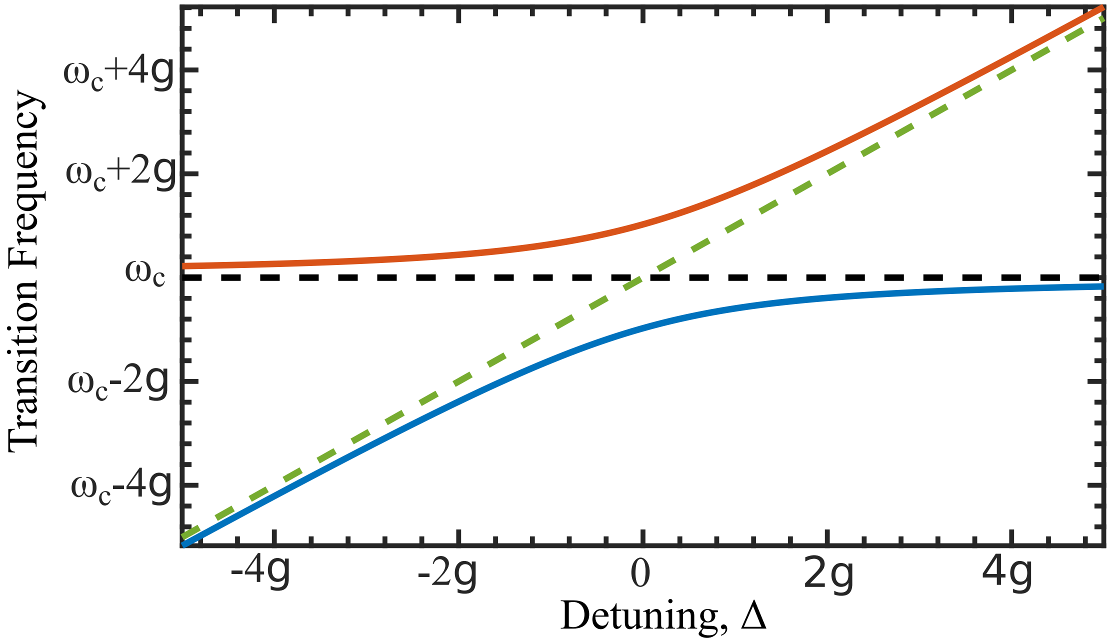

Figure 2: A plot of the avoided crossing in the transition frequency from the ground state in the one-excitation manifold. The dashed lines show the uncoupled resonator frequency, ω_c (black dashed line) and qubit frequency, ω_q (green dashed line). Qubit-cavity hybridized levels shown in red and blue.

It is useful to study the dynamics of this system in two different parameter regimes to understand the experiments described later in this thesis: the resonant regime, when $\omega_c \approx \omega_q$, and the dispersive regime, for which the detuning $\Delta \equiv \omega_q - \omega_c \gg g$. On resonance, when $\omega = \omega_c = \omega_q$, the qubit and cavity become hybridized, and the eigenmodes of the Hamiltonian are $|\psi_\pm\rangle = \frac{1}{\sqrt{2}}(|n{+}1, g\rangle \pm |n, e\rangle)$, with eigenfrequencies $\omega_\pm = \omega \pm g$ [50]. If the system has one excitation, for example, with 1 photon in the cavity, the system undergoes oscillations where the excitation is coherently swapped back and forth between the qubit and cavity at frequency g (Fig. 2).

For the dispersive regime, the Hamiltonian can be approximated to:

$$\hat{H} = \hbar\omega_c \hat{a}^\dagger \hat{a} + \frac{\hbar}{2}\omega_q \hat{\sigma}_z + \hbar\chi \hat{a}^\dagger \hat{a} \hat{\sigma}_z, \tag{2.13}$$

where $\chi = g^2/\Delta$ [50]. The above expression can be written in two useful forms:

$$\hat{H} = \hbar(\omega_c + \chi\hat{\sigma}_z)\hat{a}^\dagger \hat{a} + \frac{\hbar}{2}\omega_q \hat{\sigma}_z, \tag{2.14}$$

which exhibits a qubit-state dependent shift of the cavity frequency, which can be used for a measurement of the qubit state. Alternatively, by grouping the χ-shift term with the qubit portion:

$$\hat{H} = \hbar\omega_c \hat{a}^\dagger \hat{a} + \hbar \left(\frac{\omega_q}{2} + \chi \hat{a}^\dagger \hat{a} \right) \sigma_z, \tag{2.15}$$

where one can see a number-state dependent ac Stark shift of the qubit frequency, which can be used to probe the photon number in the cavity [51, 52].

The above Hamiltonian expressions correspond to unitary evolution of the system, However, the system is inescapably always coupled to the environment. This leads to two kind of incoherent processes: the decay of excitations from the qubit or cavity to the environment, and dephasing, where the phase of the superposition state is scrambled.

2.4 Superconducting cavities

The second part of a circuit QED system is the cavity, which is a linear harmonic oscillator that is often implemented with thin-film coplanar waveguide (CPW) resonators [53], or sometimes 3D waveguide cavities [54] or lumped-element LC oscillators. Superconducting 3D waveguide cavities are capable of reaching somewhat higher internal quality factors compared to CPW resonators [55]. However, the large physical size for the 3D cavities makes them incompatible with large qubit arrays. Figure 3 shows the geometry of a CPW transmission line, where the center conductor and ground plane are made from a superconducting thin film on a low-loss dielectric substrate, typically high resistivity Si or sapphire. A resonator is formed by choosing a length of a CPW transmission line and putting either small coupling capacitors to external circuitry or a short circuit at either end. Depending on the boundary conditions, the fundamental resonance is either a half wavelength or a quarter wavelength. For the remainder of this chapter, we focus on half-wave CPW resonators, but the expressions for quarter-wave resonators are similar.

2.4.1 Transmission line half-wave resonator

A half-wave resonator is made by terminating a CPW transmission line (TL) with small capacitors on both ends, resulting in open-circuit boundary conditions. The

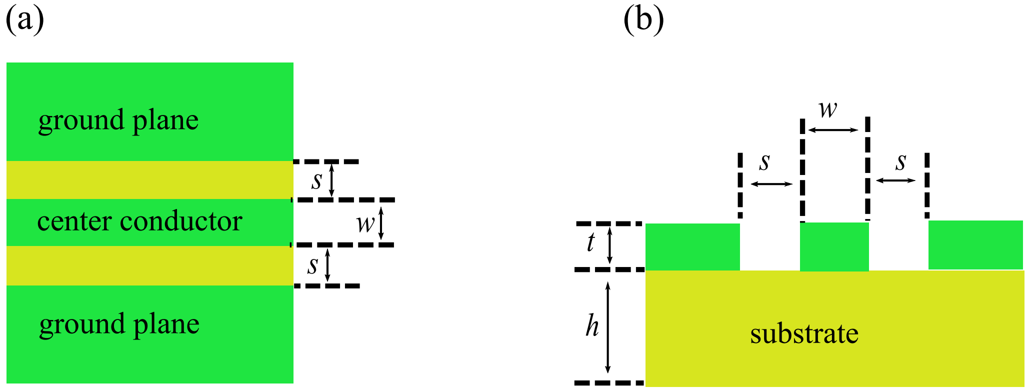

Figure 3: CPW geometry: (a) Top view of a CPW with center conductor width w and slot width s; (b) side view of a CPW with film thickness of t on top of a substrate with thickness of h.

quantities that are important for coupling a resonator to a qubit are the resonant frequency, quality factor, and impedance. The following derivation follows the highlights from Ref. [56]. The resonator's fundamental frequency is given by [56]

$$f_R = \omega_R/2\pi = \frac{c}{\sqrt{\epsilon_{eff}}}\frac{1}{2l}. \tag{2.16}$$

Here, l is the length of the resonator, $c/\sqrt{\epsilon_{eff}} = v_{ph}$ is the phase velocity, and ϵ_{eff} is a function of both the CPW geometry and materials properties. The phase velocity $v_{ph} = 1/\sqrt{L_R C_R}$ of the EM wave propagating along the TL depends on the capacitance C_R and inductance L_R per unit length, which are given by [56]:

$$L_R = \frac{\mu_0}{4}\frac{K(k_0^{'})}{k_0}, \tag{2.17}$$

$$C_R = 4\epsilon_0\epsilon_{eff}\frac{k_0}{K(k_0^{'})}. \tag{2.18}$$

Here, K denotes the complete elliptic integral of the first kind with the arguments

$$k_0 = \frac{w}{w+2s}, \tag{2.19}$$

$$k_0^{'} = \sqrt{1-k_0^2}. \tag{2.20}$$

The characteristic impedance of a CPW is then given by $Z_0 \approx \sqrt{L_R/C_R}$.

The total quality factor Q_{tot} can be broken into two contributions: an internal quality factor Q_i and an external coupling quality factor Q_c, with the following relation:

$$\frac{1}{Q_{tot}} = \frac{1}{Q_i} + \frac{1}{Q_C}. \tag{2.21}$$

When Q_c is large compared to Q_i, the resonator is undercoupled, in the opposite regime, it is overcoupled. The choice of coupling strength depends on the particular application [57].

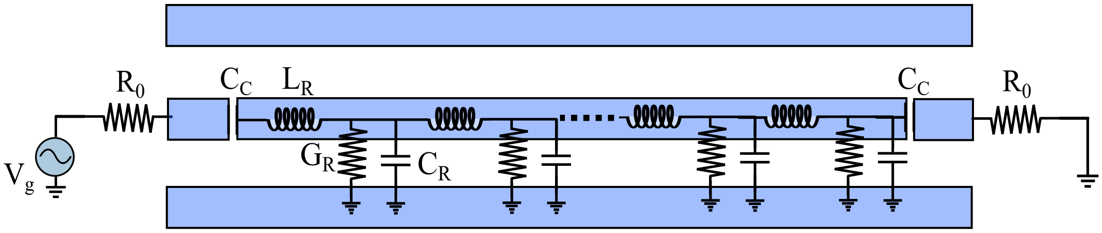

Figure 4: Circuit schematic of a TL half-wave resonator with external power source and load. C_c is the input/output coupling capacitance, and R_0 is the source/load resistance of the external circuitry.

To calculate Q_i and Q_C, a transmission line can be treated as a discrete line formed from lumped circuit elements (Fig. 4), where G_R, L_R and C_R denote the shunt conductance, inductance, and capacitance per unit length, respectively. At position x and time t, the voltage $V(x,t)$ and current $I(x,t)$ can be related in the following way [57]:

$$\frac{\partial}{\partial x}V(x,t) = -L_R\frac{\partial}{\partial t}I(x,t), \tag{2.22}$$

$$\frac{\partial}{\partial x}I(x,t) = -C_R\frac{\partial}{\partial t}V(x,t) - G_R V(x,t). \tag{2.23}$$

The impedance of a TL resonator of length l can be found as [56]:

$$Z_{TL} = Z_0\frac{1 + i\tan kl \tanh \alpha l}{\tanh \alpha l + i\tan kl} \approx \frac{Z_0}{\alpha l + i\frac{\pi}{\omega_0}(\omega - \omega_n)}, \tag{2.24}$$

where α is the attenuation constant, and $k = \omega_n/v_{ph}$ is the phase constant.

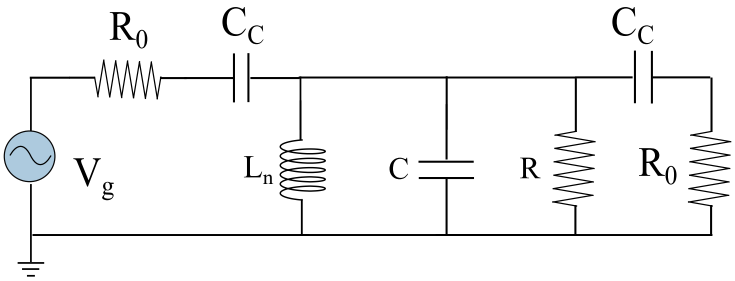

Figure 5: Diagram of a loaded parallel LCR resonator circuit.

Near the nth resonance mode, a TL resonator can be modeled as a parallel circuit made from a single lumped-element inductor L_n, capacitor C and resistor R (Fig. 5). For a simple parallel LCR circuit, the impedance of the circuit is given by:

$$Z_{LCR} = \left(\frac{1}{i\omega L_n} + i\omega C + \frac{1}{R}\right)^{-1}. \tag{2.25}$$

From this it is easy to derive (Ref. [57]) the resonance frequency $\omega_n = 1/\sqrt{L_n C}$ and the internal quality factor Q, which is defined as the ratio of energy stored in the LCR circuit to the energy dissipated by the resistor R per cycle:

$$Q = \frac{E_{stored}}{E_{loss}} = \omega_0 RC = \frac{R}{Z_0}. \tag{2.26}$$

Near resonance, $\omega = \omega_0 + \Delta\omega$, we can rewrite the impedance in Eq. 2.25 as [56]:

$$Z_{LCR} \approx \frac{R}{1 + 2i\Delta\omega RC} = \frac{R}{1 + 2iQ\Delta\omega/\omega_0}. \tag{2.27}$$

Now substituing values for the nth mode of a CPW resonator to the resonance of a parallel LCR circuit leads to [56]:

$$L_n = \frac{2L_R l}{n^2\pi^2}, \tag{2.28}$$

$$C = \frac{C_R l}{2}, \tag{2.29}$$

$$R = \frac{Z_0}{\alpha l}. \tag{2.30}$$

Then, Q_i and Q_c can be expressed in terms of the transmission-line parameters as [56]:

$$Q_i = \omega_n RC = \frac{n\pi}{2\alpha l}, \tag{2.31}$$

and

$$Q_C = \frac{n\pi}{4} \frac{1}{\omega_n^2 R_0 Z_0 C_C^2}. \tag{2.32}$$

2.5 Qubit decoherence

The above Hamiltonian expressions discussed in Sec. 2.3.1 correspond to unitary evolution of the system. That is, if we know the starting state of the qubit and its Hamiltonian, then we can predict the state of the qubit at any time in the future. When a qubit is prepared in superpostion state $\psi(0) = \alpha|0\rangle + \beta|1\rangle$, the qubit state evolves with time as:

$$\psi(t) = \alpha|0\rangle + \beta e^{i\omega_q t}|1\rangle. \tag{2.33}$$

However, in practice, the system is inescapably always coupled to the environment. This leads to two kinds of incoherent processes: relaxation and dephasing. A qubit in its excited state can decay by emitting energy into the environment and relaxing to the ground state $|0\rangle$ with rate Γ_1^r. Similarly, a qubit in state $|0\rangle$ can absorb energy from the environment and excite to the state $|1\rangle$ with rate Γ_1^e. The overall decay rate is given by $\Gamma_1 \equiv 1/T_1 = \Gamma_1^r + \Gamma_1^e$, where T_1 is the $1/e$ decay time. In the typical operating regime $k_B T \ll \hbar\omega_q$, Γ_1^e is much less than Γ_1^r, resulting in the rate $\Gamma_1 \equiv 1/T_1 \simeq \Gamma_1^r$ [43].

The second incoherent process is dephasing, where the phase of the superposition state is scrambled. From Eq. 2.33, it can be inferred that any noise process that can change the qubit frequency can also change the phase of the superposition state [58]. This decoherence of the qubit state is quantitatively described by the rate Γ_ϕ which is the pure dephasing rate. The total dephasing rate Γ_2 also includes a contribution from the energy relaxation of the excited-state component of the superposition state at a rate Γ_1, therefore [43]:

$$\Gamma_2 \equiv \frac{1}{T_2} = \frac{\Gamma_1}{2} + \Gamma_\phi. \tag{2.34}$$

The measurement process of finding T_1 and T_2 experimentally is explained in Chapter 6.

Chapter 3

Metamaterial transmission lines

In this chapter, I give a brief introduction to metamaterials, then describe important characteristics of metamaterial transmission lines and metamaterial resonators. The detailed derivations are based on earlier publications from our group and can be found in Refs. [59, 39].

3.1 Metamaterials

It is possible to engineer material systems that have properties that are not exhibited by any naturally occurring materials [60, 61] . This can be achieved by arranging the elements in repeating patterns on a length scales shorter than the wavelengths of the phenomena of interest. The unique properties of such a metamaterial do not come so much from material properties, but rather from the shape, size, geometry, or orientation of the elements. This can include materials with novel optical [62], mechanical [63], or acoustic properties[64, 65]. In electromagnetism, applications of metamaterials include systems that exhibit a negative index of refraction [61], extreme optical anisotropy [66], and engineered optical bandgaps [67].

Here, as an example, we study negative refractive index. For an isotropic linear materials, electromagentic (EM) waves the electric field $\vec{E}$, magnetic, $\vec{B}$ obeys a right hand rule with both the wave vector $\vec{k}$ and the Poynting vector $\vec{S}$ (directional energy flux), that is,

$$\vec{k} = \vec{E} \times \vec{B}, \tag{3.1}$$

and

$$\vec{S} = \vec{E} \times \vec{H}, \tag{3.2}$$

where $\vec{B} = \mu \vec{H}$ for the permeablity of the material μ [68]. This material is considered right handed. The refractive index for the material n which is defined as the ratio of of the speed of light in vacuum c to the phase velocity v, i.e., $n = c/v$. As shown in Fig. 6(a), for two right handed materials, when the light travels from one medium (medium 1) to another (medium 2 shown in orange) with different indices of refraction, part of the the light wave is reflected back with the angle (θ_1) equal to the angle of the incident wave with respect to the normal to the surface θ_0. Part of the wave is transmitted to media 2 with a different angle θ_2. The relationship between the angles of the incident and refracted wave , their velocities, thus refraction of indices are given using Snell's law[68]:

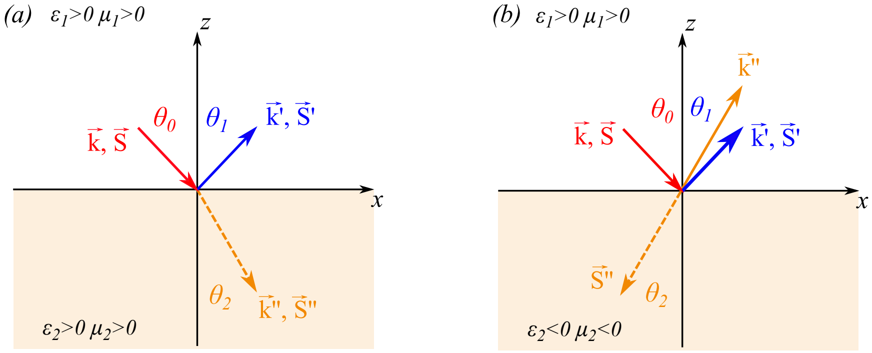
(a) $\varepsilon_1>0$ $\mu_1>0$
z
θ_0
θ_1
$\vec{k}$, $\vec{S}$
$\vec{k}'$, $\vec{S}'$
x
θ_2
$\vec{k}''$, $\vec{S}''$
$\varepsilon_2>0$ $\mu_2>0$
(b) $\varepsilon_1>0$ $\mu_1>0$
z
$\vec{k}''$
θ_0
θ_1
$\vec{k}$, $\vec{S}$
$\vec{k}'$, $\vec{S}'$
x
$\vec{S}''$
θ_2
$\varepsilon_2<0$ $\mu_2<0$

Figure 6: A diagram of of how EM waves refracts between two media with the incident wave (red $\vec{k}$ and $\vec{S}$), the reflected wave (blue $\vec{k}'$ and $\vec{S}'$) and the refracted wave (orange $\vec{k}''$ and $\vec{S}''$). (a) permittivity ϵ_2 and permeability μ_2 for medium 2 are both positive. (b) permittivity ϵ_2 and permeability μ_2 for medium 2 are both negative. Figure adapted from Ref. [59].

$$\frac{\sin\theta_1}{\sin\theta_2} = \frac{v_1}{v_2} = \frac{n_2}{n_1}. \tag{3.3}$$

If medium 2 has permittivity ϵ_2 and permeability μ_2 that are both negative, as first shown in Ref. [60], $\vec{k}$, $\vec{E}$, and $\vec{B}$ form a left-handed set and the material is described as being left-handed. However, even in this case, $\vec{S}$, $\vec{E}$, and $\vec{B}$ still form a right-handed set. This implies that the phase velocity $v_p = \omega/k$, which will point in the same direction as $\vec{k}$, will be opposite to the direction of the group velocity, $v_g = \partial\omega/\partial k$, which will point in the same direction as $\vec{S}$. The angle of refraction thus becomes negative and can be computed using the left-handed version of Snell's Law:

$$\frac{\sin\theta_1}{\sin\theta_2} = -\frac{n_2}{n_1}. \tag{3.4}$$

There are no naturally occurring materials that exhibit a negative index of refraction, but it is possible to achieve this, for certain wavelenghts, with metamaterials. Similar manipulation of the properties of light when physically realized can have wide varieties of application such as metalenses [69] that can achieve achromatic focusing of the primary colors by dispersion engineering [70].

3.2 Left handed transmission lines (LHTL)

In addition to optical systems with a negative index of refraction, it has been shown that microwave transmission lines can be engineered to have left-handed dispersion relations, resulting in opposite directions for the phase and group velocities. Such systems, fabricated from conventional metallic circuit elements, have been shown to have numerous applications, including zero-wavelength antennas [71] and broadband directional couplers [72]. In order to study left-handed metamaterials in the quantum regime, the elements must be fabricated from superconducting traces and designed in a configuration that is compatible with cQED architectures.

3.2.1 LHTL: circuit model

As discussed in Sec. 2.4.1, a transmission line with right handed dispersion (RHTL) can be modeled as an infinte chain of distributed LC network, where in each cell, an inductor is connected in series and capacitor connected in parallel to the ground. If a transmission line is created in which the position of inductors and capacitors is swapped, the transmission line exhibits left handed dispersion relation (LHTL) where mode frequency is a falling function of the mode number [73]. It is important to note that the discrete RHTL can be turned into a continuous RHTL by taking the unit cell size to zero but this does not work for LHTLs, so these can only be made with lumped elements.

To obtain expression for the dispersion relation and the infrared cutoff frequency, when Kirchhoff's Law is applied to the ciruit at a particular cell m [Fig. 7(b)], as derived in Ref. [39] we get:

$$v_m - v_{m+1} = i_m \left(\frac{1}{i\omega C_l}\right), \tag{3.5}$$

$$i_{m-1} - i_m = v_m \left(\frac{1}{i\omega L_l}\right), \tag{3.6}$$

$$v_{m-1} - v_m = i_{m-1} \left(\frac{1}{i\omega C_l}\right), \tag{3.7}$$

$$i_m - i_{m+1} = v_{m+1} \left(\frac{1}{i\omega L_l}\right). \tag{3.8}$$

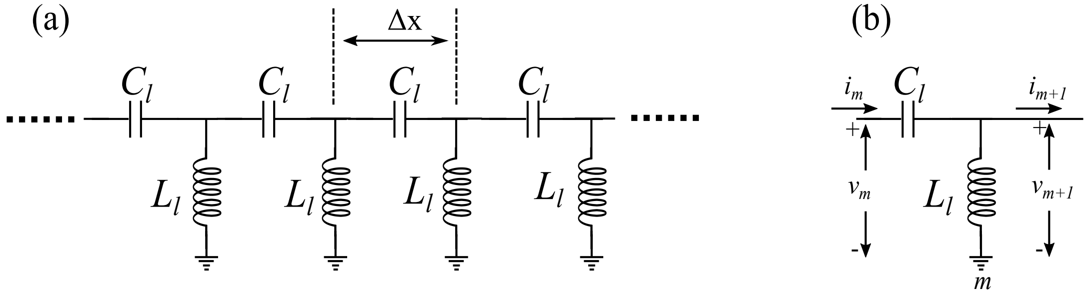

Figure 7: LHTL circuit model: (a) array of series capacitors C_l with shunt inductors L_l to ground; (b) definition of current and voltage in the LHTL at cell m.

By defining the admittance of the inductor $Y = 1/i\omega L_l$ and impedance of the capacitor $Z = 1/i\omega C_l$, we can reduce these to two expressions

$$v_m(2 + ZY) = v_{m-1} + v_{m+1}, \tag{3.9}$$

$$i_m(2 + ZY) = i_{m-1} + i_{m+1}. \tag{3.10}$$

Assuming a plane wave solution for propagation through the transmission line, the voltage and current for cell m can be written as:

$$v_m = V_0^+ e^{-ikm\Delta x} + V_0^- e^{ikm\Delta x}, \tag{3.11}$$

$$i_m = I_0^+ e^{-ikm\Delta x} + I_0^- e^{ikm\Delta x}, \tag{3.12}$$

where Δx is the unit cell length, $k = 2\pi/\lambda$ is the magnitude of the wavenumber and $V_0^+(V_0^-)$ and $I_0^+(I_0^-)$ are the amplitudes of the forward (reverse) propagating voltage and current, respectively. Combining Eqs. (3.11)-(3.12) with Eqs. (3.9)-(3.10), we obtain

$$[V_0^+ e^{-ikm\Delta x} + V_0^- e^{ikm\Delta x}][2\cos(k\Delta x) - (2 + ZY)] = 0. \tag{3.13}$$

This expression must be satisfied for all values of $km\Delta x$, therefore

$$2\cos(k\Delta x) = (2 + ZY). \tag{3.14}$$

This relationship between $k\Delta x$ and ZY leads to the dispersion relation for the transmission line

$$\omega_{LHTL}(k) = \frac{1}{2\sqrt{L_l C_l}} \frac{1}{\sin\left(\frac{k\Delta x}{2}\right)}. \tag{3.15}$$

We see that ω_L is a decreasing function of k. At $k = 0$, the sine function will be equal to zero thus the dispersion is divergent. The sine function will equal unity when its argument is $\pi/2$, corresponding to $k\Delta x = \pi$, when the wavelength is two unit cells. This shortest wavelength for propagating waves corresponds to the lowest frequency, ω_{IR}, which is the infrared cutoff frequency:

$$\omega_{IR} = \frac{1}{2\sqrt{L_l C_l}}. \tag{3.16}$$

By substituting Eq. (3.11) into Eq. (3.5) and solving for i_m, we can compare the results with Eq. (3.12) to obtain the following expressions:

$$I_0^+ = 2ie^{-ik\Delta x/2} \sin\left(\frac{k\Delta x}{2}\right) \frac{V_0^+}{Z}, \tag{3.17}$$

$$I_0^- = -2ie^{ik\Delta x/2} \sin\left(\frac{k\Delta x}{2}\right) \frac{V_0^-}{Z}. \tag{3.18}$$

Eq. (3.14) can be rewritten as

$$2i\sin\left(\frac{k\Delta x}{2}\right) = \sqrt{ZY}, \tag{3.19}$$

which can then be substituted into Eqs. (3.17)- (3.18) to yield:

$$I_0^+ = e^{-ik\Delta x/2}\frac{V_0^+}{Z_0}, \tag{3.20}$$

$$I_0^- = -\, e^{ik\Delta x/2}\frac{V_0^-}{Z_0}. \tag{3.21}$$

with

$$Z_0 = \sqrt{\frac{L_l}{C_l}}, \tag{3.22}$$

which can be defined as the characterstic impedance of the LHTL.

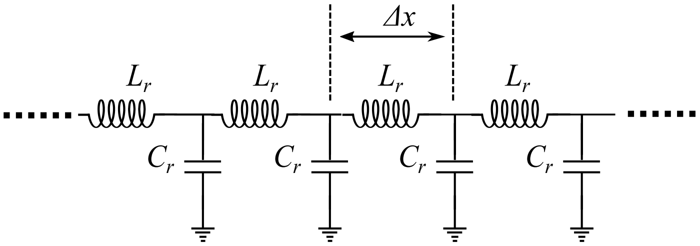

Figure 8: Circuit diagram of discrete right-handed transmission line.

Although the treatment in Eqs. (3.5)- (3.14) was described in terms of a LHTL, this can be easily extended to treat a discrete right-handed transmission line RHTL as well. For example, a RHTL in Fig. 8 with $Z = i\omega L + r$ and $Y = i\omega C_r$ has the dispersion of:

$$\omega_{RHTL} = \frac{2}{\sqrt{L_r C_r}} \sin\left(\frac{k\Delta x}{2}\right). \tag{3.23}$$

The limit of small $k\Delta x$ could correspond either to long wavelengths, or to the continuum limit when $\Delta x \to 0$. Similar to the case for LHTL, there is now a maximum allowed frequency when $k\Delta x$ is π, which corresponds again to the shortest wavelength for propagating waves of $2\Delta x$, that now occurs at the highest frequency of the transmission line, thus setting an ultraviolet cutoff:

$$\omega_{UV} = \frac{2}{\sqrt{L_r C_r}}. \tag{3.24}$$

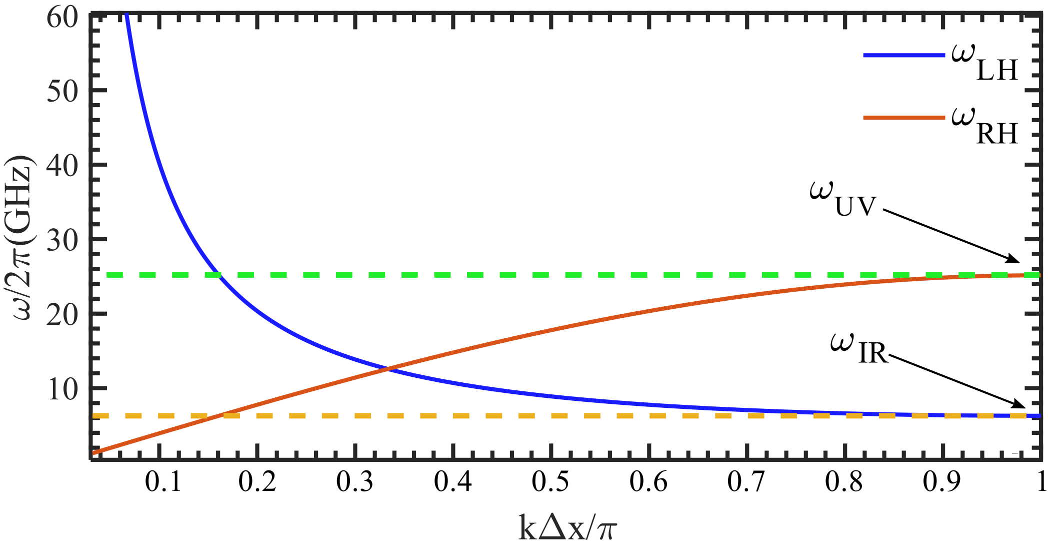

Figure 9: Dispersion relation of ideal LHTL (blue solid line) with $\omega_{IR}/2\pi = 6$ GHz. Due to its left-handed nature, k is negative, but here we plot the absolute value of k. Dispersion relation of a discrete RHTL (red solid line).

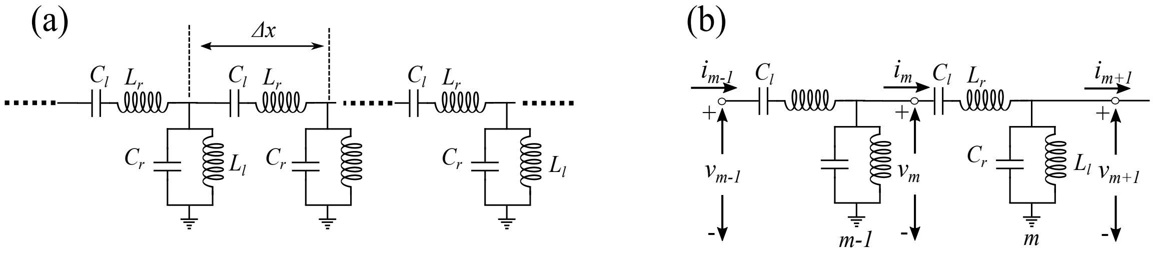

Figure 10: (a) The circuit diagram of a LHRH transmission line, which is the LHTL with stray reactances included. (b) Voltage and current in a unit cell.

3.2.2 Stray reactances in LHTL

Parasitic stray reactances alter the properties of the LHTL circuit. This can be modeled as a parasitic shunt capacitance C_r in parallel with L_l and a parasitic inductance L_r in series with C_l, as shown in Fig. 10 [71]. Thus, each inductor of the LHTL will have a self-resonance frequency $\omega_L = 1/\sqrt{L_l C_r}$. Similarly, each capacitor will have a self-resonance frequency $\omega_C = 1/\sqrt{L_r C_l}$. We will refer to such a structure as Left-Handed Right-handed (LHRH) transmission line. Following a similar treatment

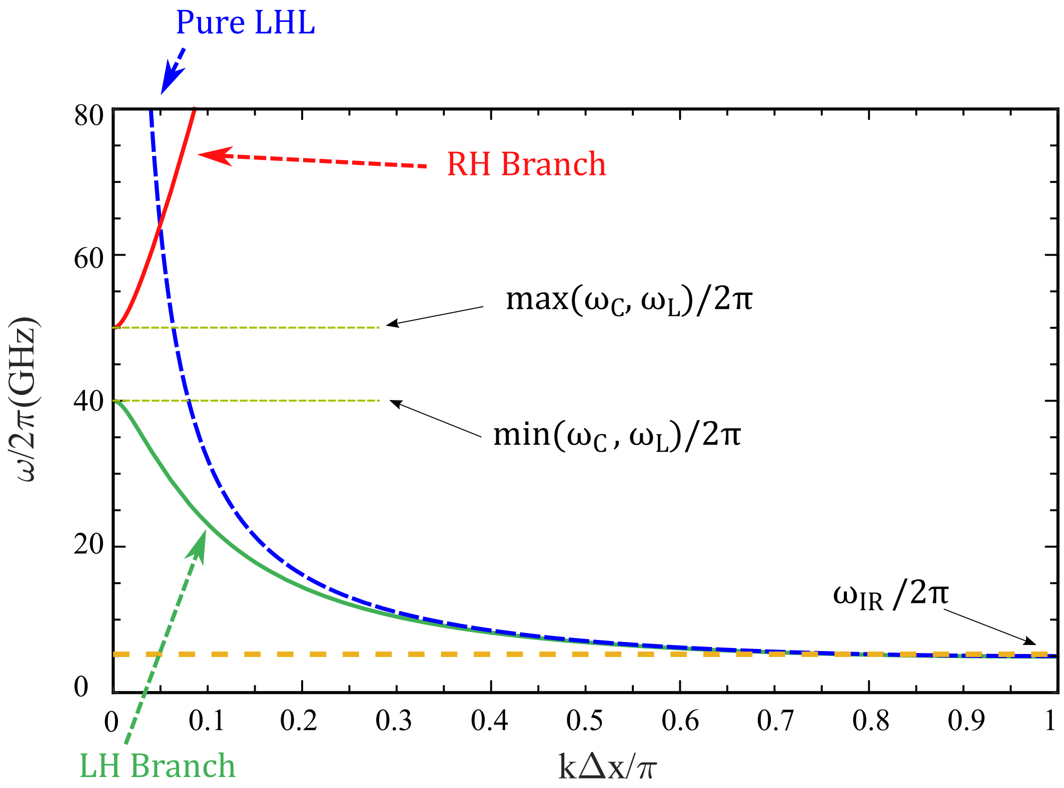

Figure 11: Calculated dispersion relations for ideal LHTL (dashed blue line) [Eq. 3.15] and composite LHTL (solid black line) [Eq. 3.29] using circuit parameters described in text. Figure adapted from Ref. [39].

to the previous section for the voltage and current in a unit cell, but now with L_r and C_r included [Fig. 10(b)] we obtain [71]:

$$v_m - v_{m+1} = i_m \left(i\omega L_r + \frac{1}{i\omega C_l} \right), \tag{3.25}$$

$$i_{m-1} - i_m = v_m \left(i\omega C_r + \frac{1}{i\omega L_l} \right), \tag{3.26}$$

$$v_{m-1} - v_m = i_{m-1} \left(i\omega L_r + \frac{1}{i\omega C_l} \right), \tag{3.27}$$

$$i_m - i_{m+1} = v_{m+1} \left(i\omega C_r + \frac{1}{i\omega L_l} \right). \tag{3.28}$$

We can then define the unit-cell series impedance $Z = i\omega L_r + 1/i\omega C_l$ and the unit-cell shunt admittance $Y = i\omega C_r + 1/i\omega L_l$. If we follow the steps similar to in previous section, we can derive the dispersion relation for the LHRH transmission line, which is given by:

$$k(\omega) = \frac{1}{\Delta x}\cos^{-1}\left[1 - \frac{1}{2}\left(\omega L_r - \frac{1}{\omega C_l}\right)\left(\omega C_r - \frac{1}{\omega L_l}\right)\right]. \tag{3.29}$$

When inverted, this has two solutions for $\omega(k)$, which are plotted in Fig. 11. We see there is a left-handed branch at low frequency, which approaches the dispersion for an ideal LHTL near ω_{IR}. When the magnitude of k is small, rather than diverging unphysically, the LHRH dispersion intercepts the $k = 0$ axis at the lower of the two self-resonance frequencies: $\min(\omega_L, \omega_C)$. Between the two self resonance frequencies, there is a gap with no propagating solutions, then a branch with right-handed dispersion begins at the larger of the two self-resonance frequencies, $\max(\omega_L, \omega_C)$. The characteristic impedance still given by $\sqrt{Z/Y}$ modifies to [71]:

$$Z_0 = \sqrt{\frac{L_l}{C_l}}\sqrt{\frac{1-\omega^2 L_r C_l}{1-\omega^2 C_r L_l}} = \sqrt{\frac{L_l}{C_l}}\sqrt{\frac{1-\omega^2/\omega_L^2}{1-\omega^2/\omega_C^2}}. \tag{3.30}$$

Despite this frequency dependence of Z_0 for an LHRH line, this does not deviate by more than 1% relative to $\sqrt{L_l/C_l}$ over the frequency range of our measurements for our typical devices parameters.

3.3 Left-handed transmission line resonator

By imposing boundary conditions and defining a length, metamaterial transmission-line resonators can be formed in the same way as continuous CPW resonators. Here we focus on configurations with coupling capacitors to external circuitry at both ends of the line [Fig. 12(a)], where the fundamental resonance corresponds to half of a wavelength along the resonator. Here, we summarize the characteristics such as dispersion relation, transmission S_{21} factor, impedance, and coupling losses of a LHTL resonator. The effect of stray reactances on these characteristics is also discussed. The original detailed derivations that are presented in part here can be found in Refs. [59] and [39].

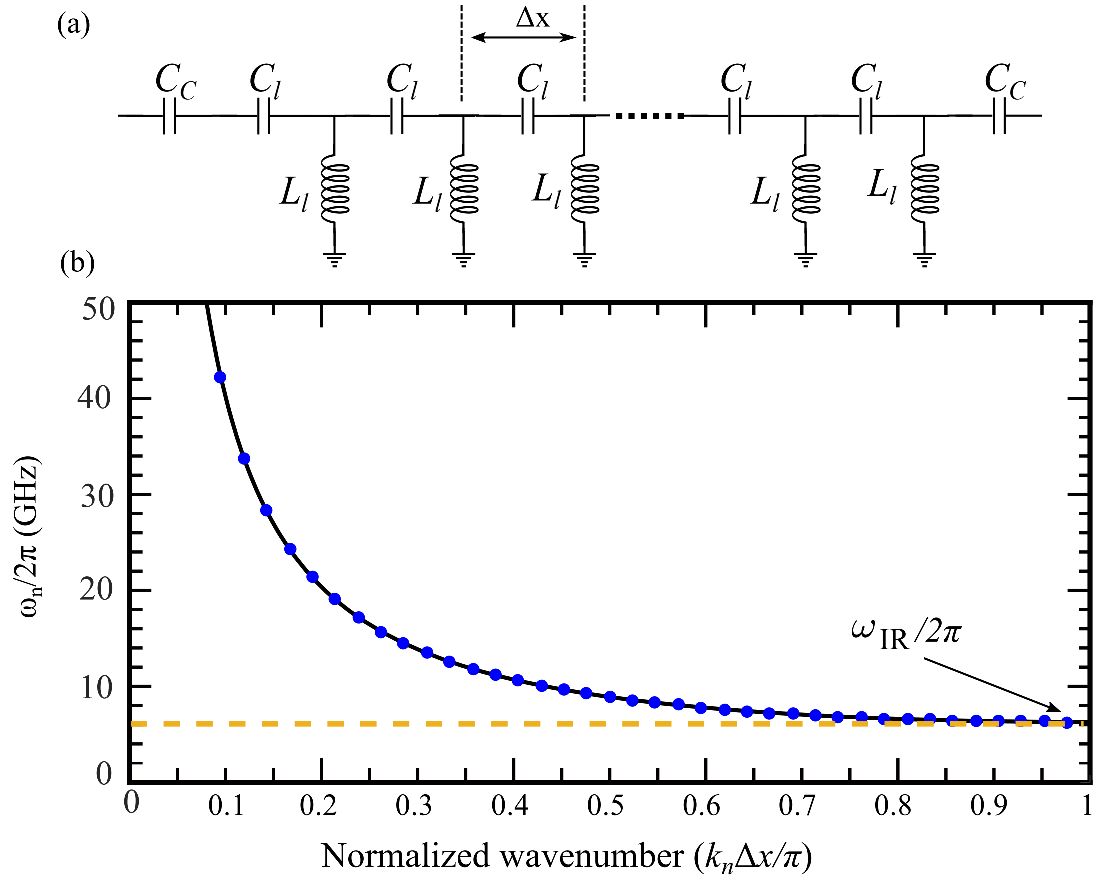

Figure 12: (a) Schematic of an ideal LHTL terminated by coupling capacitors C_C. (b) Dispersion relation of a LHTL resonator with normalized wavenumber. The blue points here correspond to the resonant modes where $k\Delta x = n\pi/N$, while the solid black line is the dispersion relation calculated using (Eq. 3.15) for the parameters N =42, C_l =250 fF and L_l=0.625 nH. Figure adapted from Ref. [59].

3.3.1 Ideal LHTL resonator

For an an ideal LHTL, which does not have any stray reactances, the dispersion relation is given by Eq. 3.15. When the number of unit cells N is finite, the open boundary conditions lead to resonances whenever $kl = n\pi$, where $n \in \{0, N\}$. Since the total length $l = N\Delta x$, we obtain:

$$k\Delta x = \frac{n\pi}{N}. \tag{3.31}$$

From Fig. 12(b), we see that the mode frequency diverges as $k \to 0$, thus there is no mode for $n = 0$. Also, as we will see later in this chapter, the coupling factor is infinite for mode $n = N$, so the resonance there cannot be measured. Thus, for an LHTL resonator made from N cells, we can see at most $N - 1$ modes. Due to the left-handed nature of the dispersion, the small-n mode, which correspond to long wavelengths, are at high frequency. At the same time, the high-n modes with short wavelengths correspond to the lowest frequencies. Near the infrared cutoff, the mode spacing is very small due to the flatness of the band.

3.3.2 Effects of stray reactance: LHRH resonator

As described in Sec. 3.2.2, an LHTL cavity built from physical circuit elements will always have parasitic reactances. We see the effect of this in the changes of the dispersion relation. Due to the self-resonance frequencies of the capacitors and(or) inductors, the dispersion dispersion $\omega(k)$ no longer diverges as $k \to 0$. This also reduces the mode spacing between all the modes since the same $N - 1$ number of modes will now be compressed into a smaller frequency span, although this effect is maximum for higher frequency modes and we only see a small decrease in the mode spacing at lower frequency modes. The structure can now also support an $n = 0$ mode [71]. At this mode, the resonance will have infinite wavelength while non-zero frequency. Voltage in all units cells oscillate up and down in phase so there are no nodes or antinodes. Because the stray capacitance C_r and inductances L_r are typically small, this novel $n = 0$ mode typically lies out of the measurement range for our typical LHTL resonators. However, in future devices, it might be possible to reduce the frequency of this mode by intentionally adding a series inductor to the C_l or a shunt capacitor in parallel to L_l. Figure 13(b) shows the modes and dispersion relation for the LH branch of an LHRH resonator for the same parameters as in the dispersion plot from Fig. 11.

3.3.3 LHRH impedance and transmission $S_{21}(\omega)$

As derived in Refs. [59] and [39], the impedance of a general discrete transmission line with N cell is:

$$Z_{-N} = Z_0 \frac{e^{ikN\Delta x} + \Gamma e^{-ikN\Delta x}}{e^{-ik(-N+\frac{1}{2})\Delta x} - \Gamma e^{ik(-N+\frac{1}{2})\Delta x}}, \tag{3.32}$$

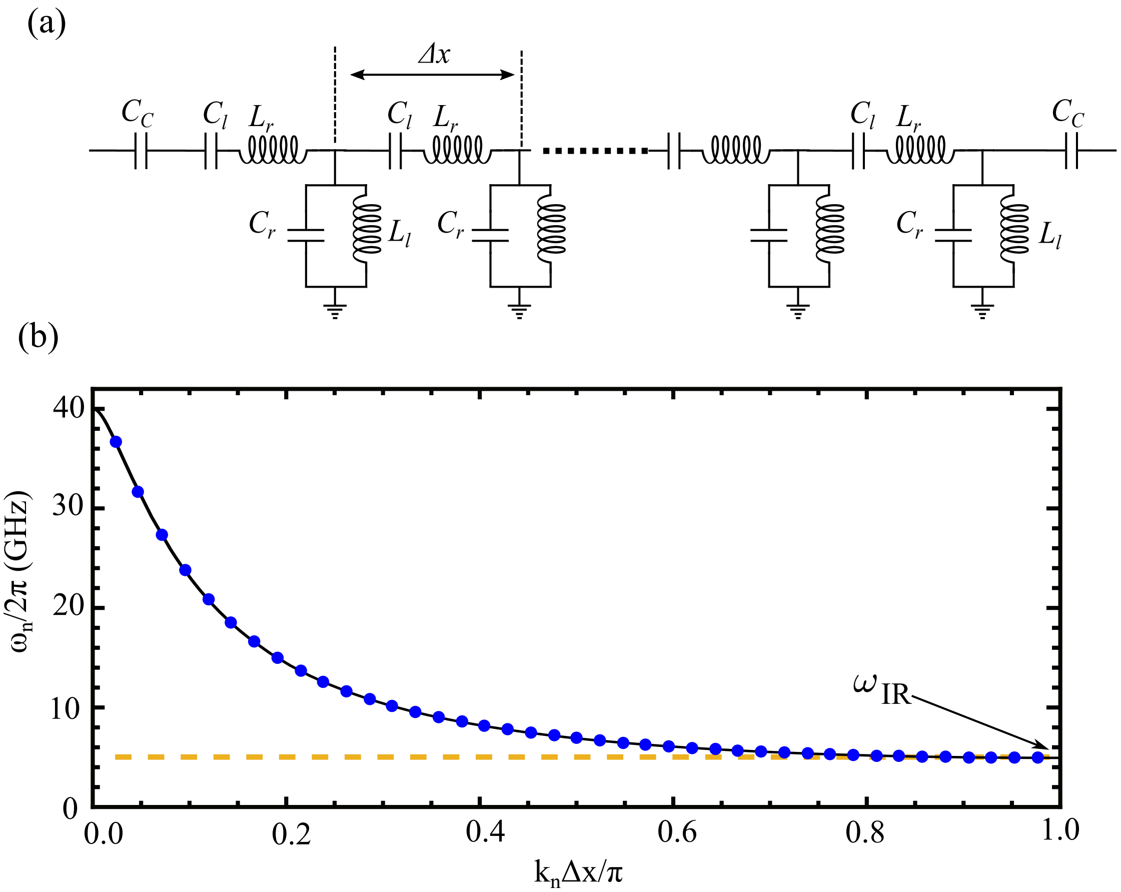

Figure 13: (a) Schematic of a composite LHRH resonator with stray reactances including coupling capacitances C_c at each end. (b) Plot of mode frequencies vs. wave number computed for for a composite LHRH resonaotr with 42 cells . The solid line is the dispersion relation obtained from [Eq. (3.29)] using circuit parameters described in text. Figure adapted from Ref. [39].

Where

$$\Gamma = \frac{Z_l e^{\frac{-ik\Delta x}{2}} - Z_0}{Z_l e^{\frac{ik\Delta x}{2}} + Z_0}, \tag{3.33}$$

can be found by requiring that, at cell $m = 0$, impedance $Z_m = Z_l$, where Z_l is the load resistance [Fig. 14] and Z_0 is the characteristic impedance of the line defined as $Z_0 = Z/2i\sin(k\Delta x/2)$. Equation 3.32 provides impedance of a general result for a lossless discrete transmission line. The details of a particular transmission line with a particular $\omega(k)$ would be encoded in the k values in this expression to determine

$Z_{-N}(\omega)$.

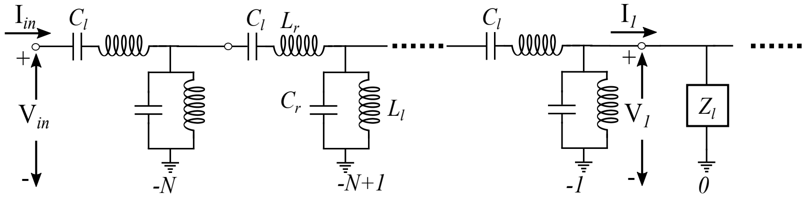

Figure 14: The circuit diagram of a lossless LHRH transmission line with load impedance Z_l on the right end. Figure adapted from Ref. [39].

In order to derive a general expression for $S_{21}(\omega)$ through a discrete transmission line resonator, we take the terminating load to be determined by the output coupling capacitor C_c and a resistive load R_0 such that the impedance of the terminating cell at $m = 0$ is $Z_l = R_0 + 1/i\omega C_c$. We then add an input drive with source resistor R_0 and input coupling capacitance C_c , such that source impedance, $Z_s = Z_l$. For simplicity, we assume symmetric coupling. However, the analysis could easily be extended to the case of asymmetric coupling. $S_{21}(\omega)$ as derived in Refs. [59] and [39] is given by:

$$S_{21} = \frac{2Z_{-N}}{Z_s + Z_{-N}} \frac{R_0}{Z_l} \frac{1 + \Gamma}{e^{ikN\Delta x} + \Gamma e^{-ikN\Delta x}}. \tag{3.34}$$

S_{21} for a particular transmission line can then be computed from Eq. (3.34) by substituting Eq. (3.32) for Z_{-N} and Eq. (3.33) for Γ. Note that the frequency dependence of S_{21} is determined by the dispersion relation $k(\omega)$ that one chooses. In Fig. 15, we plot $S_{21}(\omega)$ computed from Eq. (3.34) for the $n = 23$ mode of a LHRH resonator with the parameters given in the caption. A numerical simulation of a circuit with these same parameters in AWR Microwave Office yields quite good agreement.

3.3.4 Coupling quality factor for discrete transmission line resonators

We can use the expressions derived in the previous sections to investigate the coupling loss for a discrete transmission line resonator. One approach to extract Q_c for each mode of a discrete transmission line resonator is to use Eq. (3.34) for $S_{21}(\omega)$ and fit Lorentzians to each resonance peak to determine the linewidth. Alternatively, it would be useful to derive a closed-form expression for Q_c for more efficient evaluation

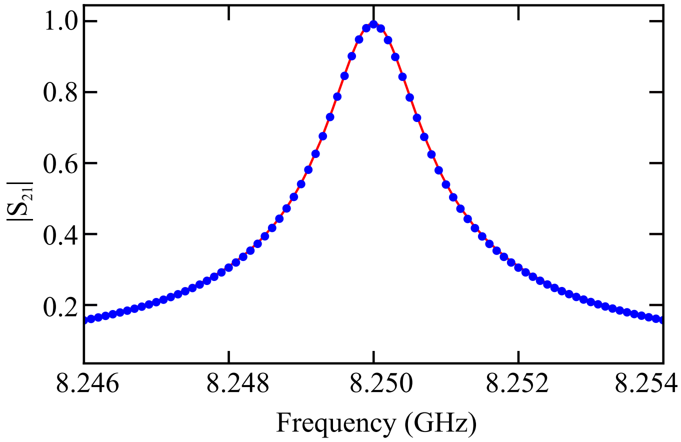

Figure 15: $S_{21}(f)$ calculated for the $n = 23$ mode of a 42-cell LHRH metamaterial resonator using Eq. (3.34) (solid red line) and simulated using AWR Microwave Office (blue points). Unit cell parameters are: $C_l = 266$ fF, $L_L = 0.6$ nH, $C_r = 21.806$ fF and $L_r = 0.595$ nH, chosen based on the discussion in Chapter 4. Figure taken from Ref. [39].

of circuits. This can be done by considering the equivalent LC resonant circuit for each mode of a discrete transmission line resonator then mapping this onto the expression for Q_c for the simple LC circuit. We apply this approach to compute the coupling loss for an LHTL resonator, resulting in [39]:

$$Q_c^{LHTL}(n) = \frac{2NZ_0C_l^2 \sin^3\left(\frac{n\pi}{2N}\right)}{R_0C_c^2\cos^2\left(\frac{n\pi}{2N}\right)}, \tag{3.35}$$

where, the inductance of the equivalent LC oscillator for mode n of an LHTL resonator can be found to be

$$\tilde{L}_{LHTL} = \frac{2L_l\cos^2\left(\frac{n\pi}{2N}\right)}{N}. \tag{3.36}$$

We compare the coupling loss for an LHTL resonator computed with this analytic expression with that obtained from an AWR Microwave Office circuit simulation and linewidth fits extracted from the full expression for $S_{21}(\omega)$ from Eq. (3.34). Again, the agreement between the three approaches is quite good. It is important to note the difference of the dependence of Q_c^{LHTL} on mode number n, compared to Q_c^{RHTL} for continuous and discrete cases where $Q_c^{RHTL} \propto n$ and $Q_c^{RHTL} \propto 1/(\sin\left(\frac{n\pi}{2N}\right)\cos^2\left(\frac{n\pi}{2N}\right)$, respectively [39].

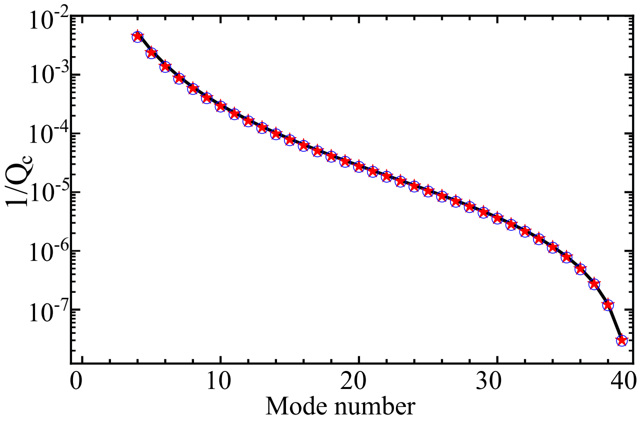

Figure 16: Coupling loss comparison for an LHTL resonator for analytic expression from Eq. (3.35)(Solid black line), AWR Microwave Office circuit simulation (Red stars), and linewidth extraction for $S_{21}(\omega)$ expression from Eq. (3.34) (blue circles). The parameters for the LHTL are: $C = 250$ fF, $L = 0.625$ nH, $C_c = 10$ fF, $N = 40$. Figure taken from Ref. [39].

Results given by Eq. 3.35 for $Q_c^{LHTL}(n)$ did not include any stray reactance in calculation. For a realistic circuit that does include such parasitic effects, these stray reactances can indeed be accounted for, but the expressions become rather unwieldy. To test the effects of neglecting the stray reactances in this analysis, in Fig. 17, we compare the coupling loss vs. n for an ideal LHTL resonator computed from Eq. (3.35) with coupling loss values obtained from the complete $S_{21}(\omega)$ expression from Eq. (3.34) using realistic values of stray reactance L_r and C_r included. As the comparison shows, the analytic expression from Eq. (3.35) for an ideal circuit agrees reasonably well with the realistic LHRH resonator for mode numbers beyond ~ 10. Only the lowest n (highest frequency) modes have any significant deviation. Thus, the simple analytic expression from Eq. (3.35) can be used for estimating coupling losses for LHTL resonators for all but the highest frequency modes, where a numerical extraction of linewidths using Eq. (3.34) should be used instead.

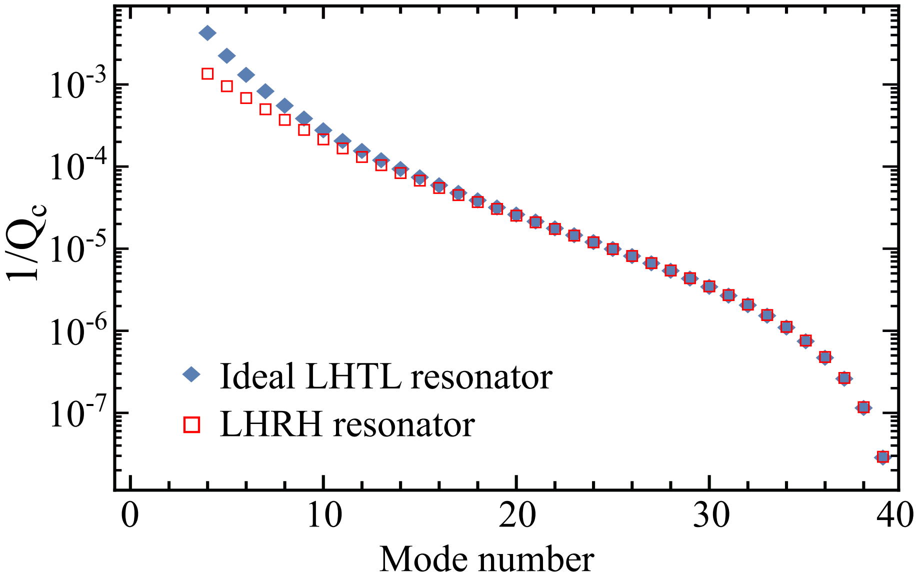

Figure 17: Coupling loss comparison between calculation for an ideal LHTL resonator using Eq. (3.35) with an LHRH resonator with non-zero stray reactances from linewidth extractions using Eq. (3.34). The parameters for the LHTL are: $C = 250$ fF, $L = 0.625$ nH, $C_c = 10$ fF, $N = 40$ $C_r = 16.211389$ fF, $L_r = 0.0334947$ nH, corresponding to self resonance frequencies of 50 GHz and 55 GHz. Figure taken from Ref. [39].

3.4 Coupling a transmon qubit to a metamaterial resonator

A variety of routes for achieving multi-mode cQED have been explored by other research groups, including long continuous transmission-line resonators [74] and metamaterials made from lumped circuit elements [75] and Josephson junctions [32, 76, 77]. For these systems, either the cavities are physically big, thus difficult to scale, or the cavities have resonance modes in the entire qubit frequency range so the qubit will always be coupled to at least some of the modes.

The metamaterial resonator provides us a possible way of engineering a high-density spectrum in the GHz frequency range, compatible with superconducting qubits, and with a relatively compact physical footprint. It also has an IR-cutoff, so the flux-tunable transmon qubit can be biased below the metamaterial modes, where coherence is long, thus allowing for high-fidelity preparation of initial qubit states. For these reasons, the metamaterial the metamaterial resonator is a promising cavity candidate for multi-mode cQED coupling to a qubit.

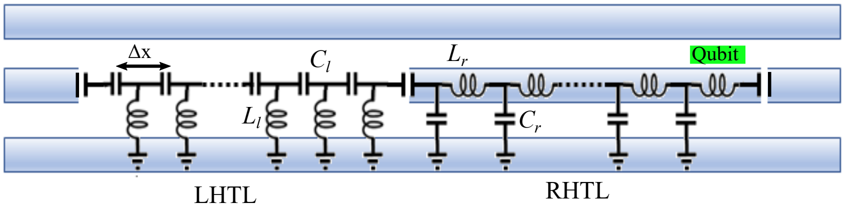

Figure 18: LHTL coupled to a continous RHL. Qubit can be coupled near the end of RHTL. Figure adapted from Ref. [33].

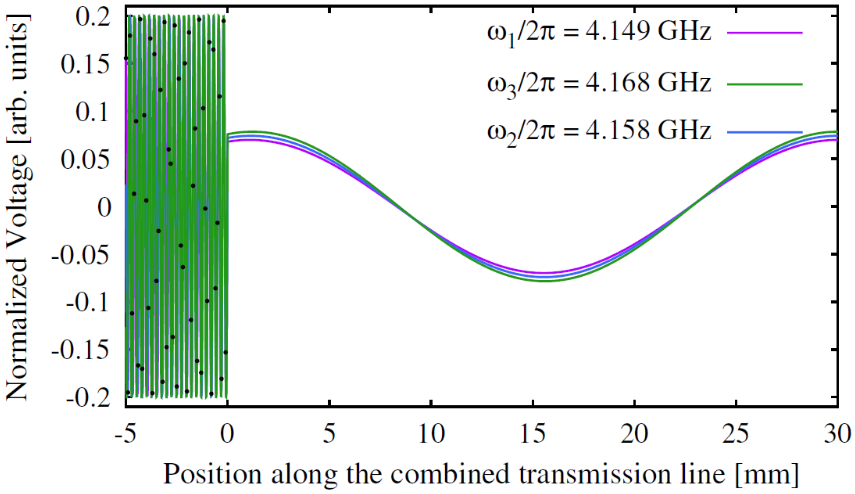

Figure 19: The standing wave patterns of the first three modes of a hybrid transmission line cavity counting from low frequency end. Figure taken from Ref. [33].

In cQED architectures, transmon qubits are coupled to resonant circuits, such as CPW resonators or 3D cavities, for various purposes, including dispersive readout [50], qubit-qubit coupling [78], and quantum memories [55, 79]. This coupling is commonly achieved through a weak capacitance to a portion of the resonator near a voltage antinode of a particular mode. The fundamental mode frequency for these resonators are typically in the GHz range. Because the mode frequency increases linearly with wavenumber, higher modes are spaced by multiples of the fundamental resonance frequency. Thus, modes are spaced by a few GHz. The coupling strength between a cavity mode and a qubit is typically in the range of 50-100 MHz. Thus, since the typical spacing between modes is significantly larger than the coupling strengths between the qubit and each mode, the qubit can only couple strongly to one mode at a time.

To develop a system with the possibility of simultaneous strong coupling between a qubit and multiple modes, Daniel Egger and Frank Wilhelm [33] proposed a novel approach: instead of using only a LHTL resonator, one can couple a continuous RHTL like a CPW to one end of the LHTL to form a hybrid transmission line and apply open-circuit boundary condition to this TL to form a hybrid cavity. The two directly coupled transmission lines should have the same impedance to avoid impedance mismatch. Shown in Fig. 19, the hybrid cavity would still have a high density of peaks and IR-cutoff at the low-frequency band edge, behaving similarly to a LHTL, while the voltage spatial distribution of the RH part would remain almost the same for the modes that are close in frequency. Thus, coupling a qubit to the end of the RH part would ensure the qubit being coupled to the voltage anti-nodes of the entire hybrid cavity.

The modes in the frequency range accessible by a typical transmon will have a short wavelength in the LH section with a much longer wavelength in the RH portion. The mode spectrum for such a hybrid LHTL-RHTL resonator still exhibits peaks near the LHTL resonances, with a slow modulation from the standing wave in the RH portion. Thus, by placing the qubit near the end of the RHTL, close to the antinodes of the low-frequency modes, the qubit can couple to all of the modes in its frequency range. The standing-wave pattern will, in general, be different for each mode. Thus, for a given qubit placement, strong coupling is only possible to the modes with large amplitudes near the qubit. In the LHTL, low frequencies correspond to short wavelengths due to the falling dispersion relation. Thus, by only a small change in frequency, a new orthogonal mode can be found that is different by one node in the left-handed component. But because of the hybrid nature of this new hybrid TL, the closely spaced frequencies at this lower band edge have nearly identical spatial structures in the RHTL. The specific details of how it was implemented in our devices are provided in Sec. 4.4.

Chapter 4

Device Design

In this chapter, I discuss the design considerations for implementing an LHTL coupled to a qubit. The chapter is divided into sections based on the different circuit elements of the device. One of the most important circuit element for our device, a LHTL resonator was designed, fabricated and characterized in detail as a standalone chip, referred to Device A in the rest of the thesis. In a subsequent design, the LHTL resonator was combined with a RHTL made from a CPW to create a hybrid LHTL-RHTL metamaterial resonator. Furthermore, the hybrid metamaterial was coupled to a transmon qubit. A separate CPW resonator was included in the design to probe and manipulate the transmon. This design will be referred to Device B in the rest of thesis and most of the discussion will be focused on this device. A similar design to Device B, with the exception of a slight difference in the layout of the inductors for LHTL was also designed. Our research group is currently pursuing new metamaterial device designs and preliminary measurements will be presented in Chapter 8.

4.1 LHTL Design

As described in Chapter 3, a metamaterial transmission line can be implemented with a 1D chain of lumped circuit elements with series capacitors and inductors to ground [37]. The number of modes in the spectrum with left-handed dispersion for a LHTL resonator with open boundary conditions at both ends is equal to the number of unit cells, where each unit cell consists of a series capacitor with an inductor connecting one side of the capacitor to ground.

To design a LHTL resonator that exhibits the desired characteristics and dispersion relation, the target values of the capacitors and inductors have several fundamental and practical constraints. Two important fundamental quantities for LHTL resonator, which are determined by the values of the unit-cell capacitor C_l and inductor L_l, are the infrared cutoff, which is the frequency of the first LHTL mode, $\omega_{IR} = 1/2\sqrt{L_l C_l}$ and the characteristic impedance of the LHTL, Z_l, given approximately by $\sqrt{L_l/C_l}$. The characteristic impedance of the LHTL resonator for most of the devices studied during the work was designed to be 50 Ohms to minimize the reflection and losses to the external measurement circuity.

Table 1: Metamaterial parameters determined by finite element simulations of circuit layout.

Label	Description	Value
L_l	Unit cell inductance	0.7 nH
C_l	Unit cell capacitance	250 fF
L_r	Unit cell stray inductance	0.03 nH
C_r	Unit cell stray capacitance	25 fF

For a LHTL resonator with a fixed characteristic impedance, theoretically any infrared cutoff frequency can be achieved by adjusting the C_l and L_l values. However, in practice these parameter values will be limited by the physical extent of the circuit elements and their self-resonance frequencies ($\omega_C = 1/\sqrt{L_r C_l}$ and $\omega_L = 1/\sqrt{L_l C_r}$). Also, as a practical consideration, we must ensure that ω_{IR} and at least several modes fall in the region where they can be measured in the lab with our standard microwave electronics hardware (~2-12 GHz). In addition, since we want to couple several modes from the densest portion of the LHTL spectrum to a superconducting qubit, the range for $\omega_{IR}/2\pi$ narrows down to ~4-9 GHz, where superconducting qubits are typically operated. Furthermore, we would like $\omega_{IR}/2\pi$ to be around 5 GHz so that the qubit frequency can be tuned to be below ω_{IR} for longer qubit lifetimes, as will be discussed later. As described in the previous chapter, the presence of stray reactances for the inductors and capacitances impacts the dispersion relation for a LHTL resonator. However, this change is primarily at the high-frequency end of the spectrum, which is typically outside of our measurement range with the parameters of our designed

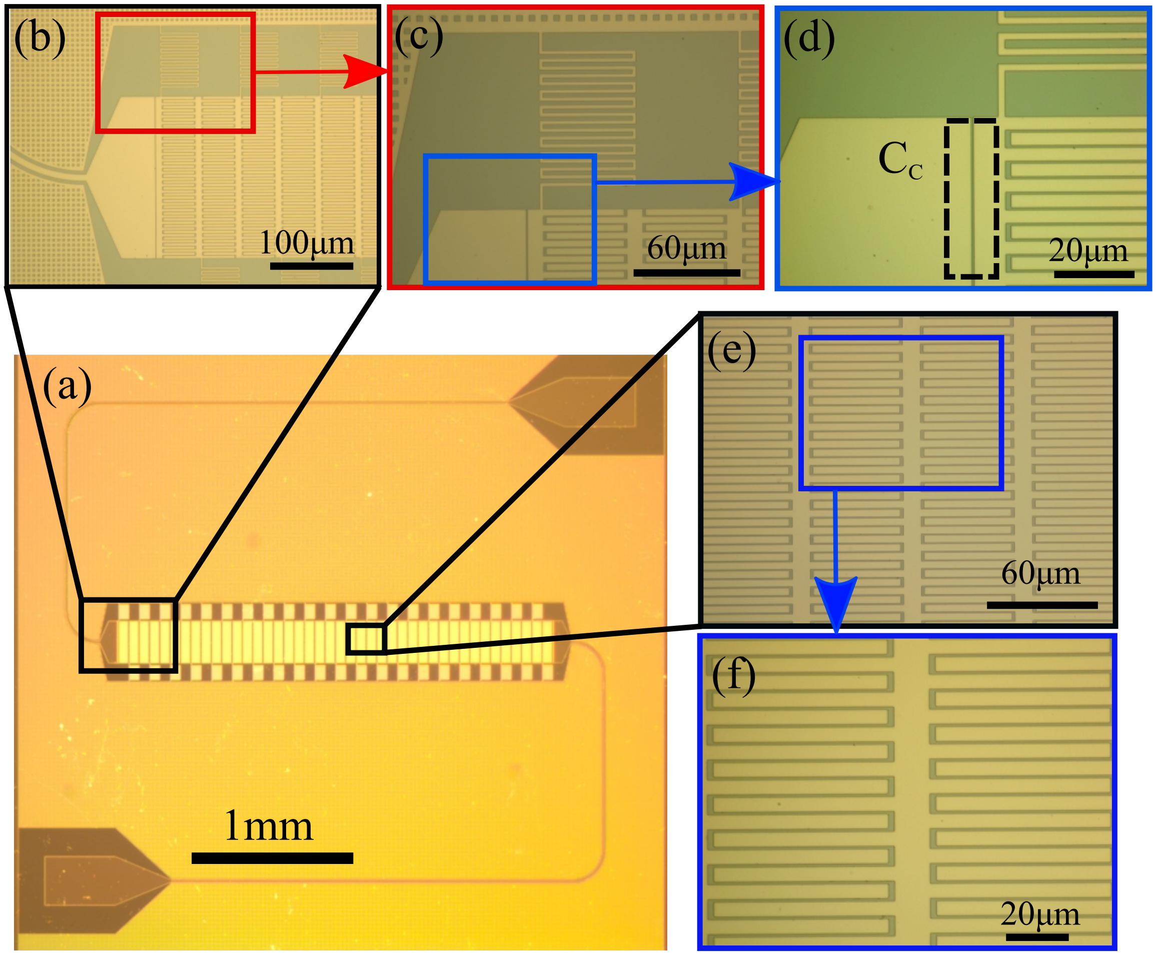

Figure 20: Optical micrographs of LHTL resonator device (Device A): (a) zoomed-out image of entire chip, (b) input coupling capacitor Cc and first few unit cells, (c) meanderline inductor of first unit cell, (d) detail of input coupling capacitor and connection between inductor and capacitor of first unit cell, (e) interdigitated capacitors in several unit cells, (f) detail of interdigitated capacitor.

LHTL resonator.

In order to implement the LHTL resonator with high-Q modes that is compatible with coupling to superconducting qubits, we fabricate the inductors and capacitors from thin-film superconducting Nb thin films. For the capacitors, we use an interdigitated design with 29 pairs of 4-μm wide/52-μm long fingers for each capacitor. For the inductors, we use a meander-line design with 9 turns of 2-μm wide traces. The dimensions of these elements are based on the simulations and experiments in our earlier LHTL work, described in Ref. [80]. The design values for the parameters are given in Table 1. The inductors are arranged in a staggered pattern with alternating inductors connected to the ground plane on either side of the LHTL, as in Ref. [39], to maximize the number of cells that can be physically implemented on a Si chip in the 4-mm window of our standard sample holder. This leads to a total of 42 unit cells for our 3.5-mm long LHTL resonator. The ends of the metamaterial resonator are defined with coupling capacitor gaps at the first and last cells to conventional coplanar waveguide (CPW) traces carrying the output/input signals to/from launcher pads at the opposite corners of the chip. We estimate the C_c values for these structures to be 30 fF based on HFSS Q3D simulations. Figure 20 shows the optical image of such a LHTL resonator.

4.2 Qubit design

We follow the design of transmon qubit widely used in the superconducting quantum computing commmunity, More specifically, we adapt the floating-transmon design from earlier work done by IBM [45, 46, 47]. Two important quantities for designing a transmon are qubit frequency and anharmonicity, which depend on E_J and E_C. E_J is determined by the junction thickness and junction area. E_C is determined by the total qubit capacitance $C_\Sigma = C_Q + 2C_J + C_{QR} + C_{QM}$. C_Σ for a transmon is typically dominated by shunt capacitance C_Q. We calculate the values of the different capacitance components (Table 3) by doing a full network analysis, similar to the treatment in Appendix A of Ref. [44], for the capacitance matrix obtained from Q3D simulation of the qubit layout as shown in Fig. 21. The transmon used in the device contains a split junction geometry allowing for the qubit transition frequency to be tuned with an external magnetic flux, which is provided by a wire- wound coil above the chip .The capacitance contributed from each junction C_J is $\sim$2.5 fF. While the split junction design allows for flexibility in the tunability of the qubit transition, it also leads to enhanced qubit dephasing due to magnetic flux noise. For future devices, asymmetric transmons[44] made from junctions with different areas can be used to balance the tunabilty of qubit frequency and qubit dephasing [48].

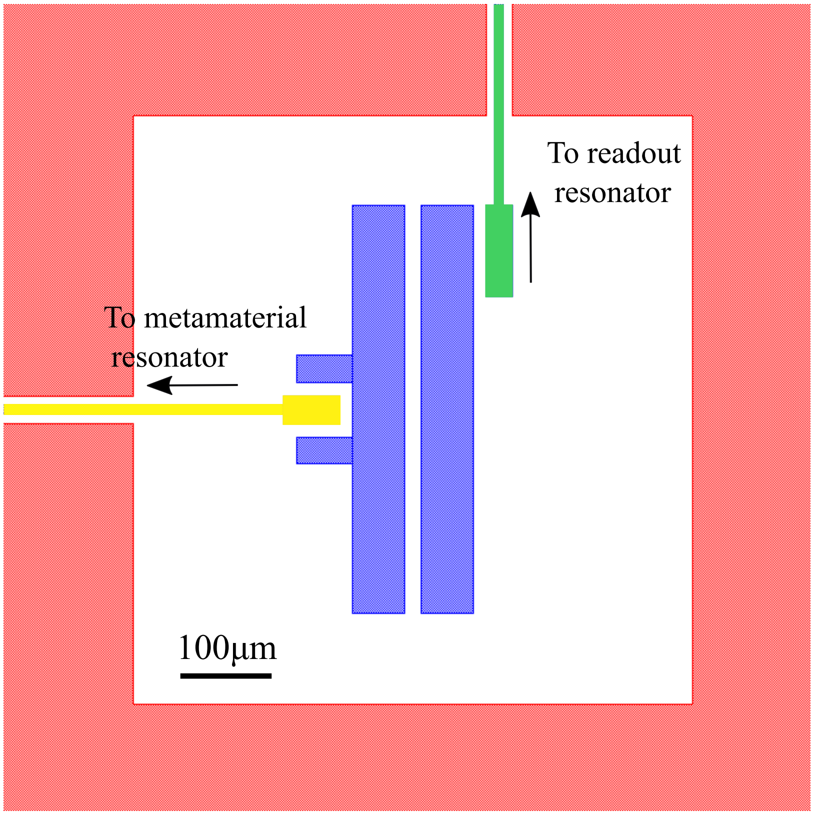

Figure 21: Layout of the transmon used in the device showing the shunt capacitor pads (blue) and coupler to the metamaterial(yellow) and the coupler to readout resonator (green) and ground plane(red)

4.3 Readout resonator

A separate half-wave CPW resonator is coupled to the qubit by the capacitor, $C_{QR} = 4.8$ fF, for conventional dispersive readout of the qubit state [50]. A 10-μm wide center conductor and a 6-μm wide gap to the ground plane allow 50 ohms charcaterstic impedance for the CPW resonator. The parameters of the CPW and length of readout resonator(7.7-mm), which are defined by input capacitor C_{cR}^{in} and output capacitor C_{cR}^{out} capacitors, determines the fundamental mode frequency ($f_R = \omega_R/2\pi$) of the readout resonator. The C_{cR}^{in} and C_{cR}^{out} also determines the coupling loss($1/Q_c$) of readout resonator to the measurement circuitry and its transmission peak level. Q_c and internal quality factor (Q_i) contributes to the total quality factor of the resonator ($Q_{tot}^{-1} = Q_c^{-1} + Q_i^{-1}$). We design the resonator to be in the overcoupled regime ($Q_c >> Q_i$) where $Q_c^{-1} = Q_{in}^{-1} + Q_{out}^{-1}$ and the total quality factor of ∼15k. The linewidth of the resonator $\kappa/2\pi = f_R/Q_{tot}$ should be several times of the dispersive shift readout reasonator frequency due to the qubit to resolve the the different qubit excitation levels [81]. Further details of parameters is provided in Table 2.

Table 2: Qubit and readout resonator design parameters.

Label	Description	Value	Method of Determination
C_Q	Qubit shunt capacitance	48 fF	Finite element simulations
C_{QR}	Qubit-readout resonator coupling capacitor	4.8 fF	Finite element simulations
C_{QM}	Qubit-metametarial coupling capacitor	4.3 fF	Finite element simulations
C_J	Junction capacitance	2.5 fF	Junction area from SEM image
C_{cR}^{in}	Readout resonator input coupling capacitor	1 fF	Finite element simulations
C_{cR}^{out}	Readout resonator output coupling capacitor	2 fF	Finite element simulations
l_R	Readout resonator length	7.7 mm	

4.4 Metamaterial coupled to a transmon

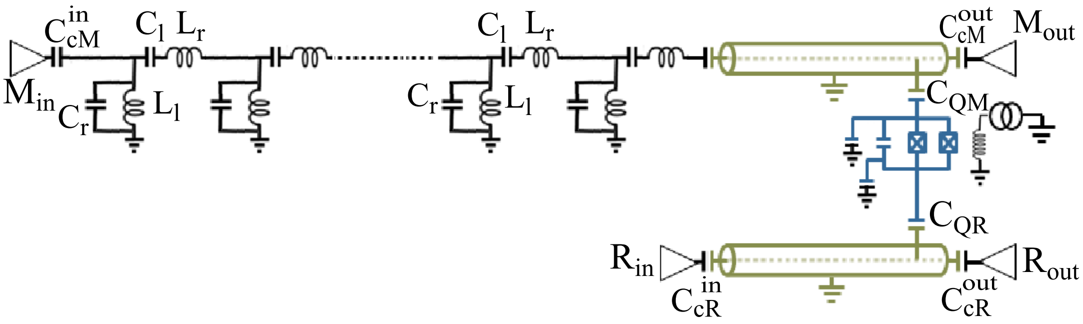

Figure 22: Circuit schematic of the device.

As described in Sec 3.4, to couple our LHTL resonator to a qubit we follow the approach given in Ref. [33]. We build a hybrid system with one end of the LHTL

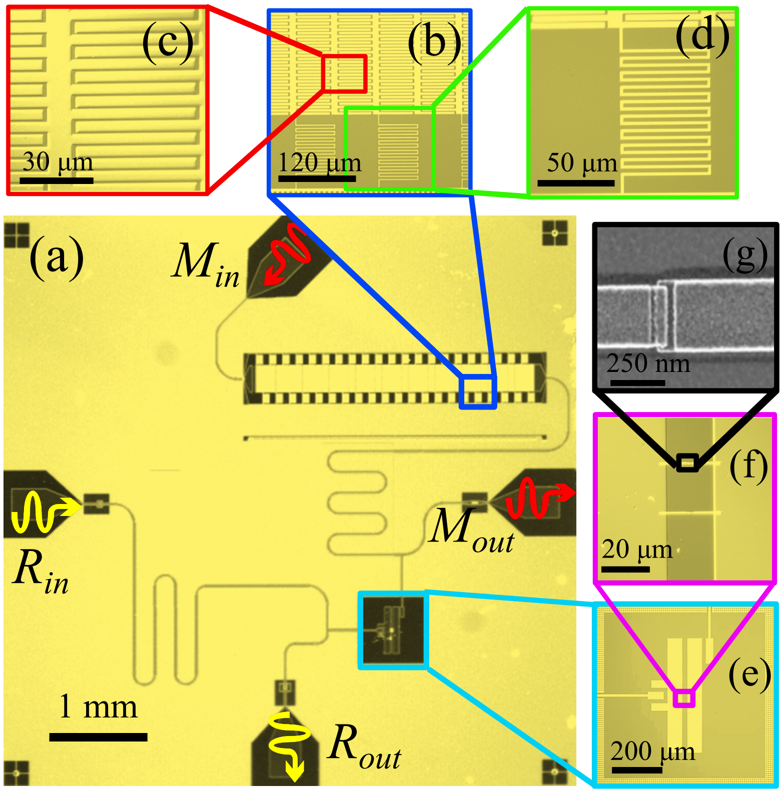

Figure 23: (a-g) Optical micrographs of metamaterial resonator device B: (a) zoomed-out image of entire chip, (b) section of metamaterial resonator containing several unit cells of inductors and capacitors, (c) detail of interdigitated capacitor, (d) detail of meander-line inductor, (e) transmon qubit with coupling capacitors to metamaterial resonator and readout resonator,(f) SQUID loop of the transmon, (g) Scanning electron microscope (SEM) image of one of the transmon junctions.

connected to a right-handed transmission line (RHTL). The transmon qubit is placed near the other end of the RHTL. Figure 22 show the schematic for our device where the LHTL resonator is integrated to couple it to a qubit (Device B). Figure 23 show the optical micrograph for our device (Device B). Table 1 lists the LHTL resonator parameters, for our integrated chip, which are determined by finite-element simulations.

The input coupling capacitor C_{cM}^{in} ($\sim$ 30 fF) near the end of the LHTL portion and the output coupling capacitor C_{cM}^{out} ($\sim$ 25 fF) near the end of the RHTL portion define the resonant modes of the hybrid metamaterial resonator. The input coupling

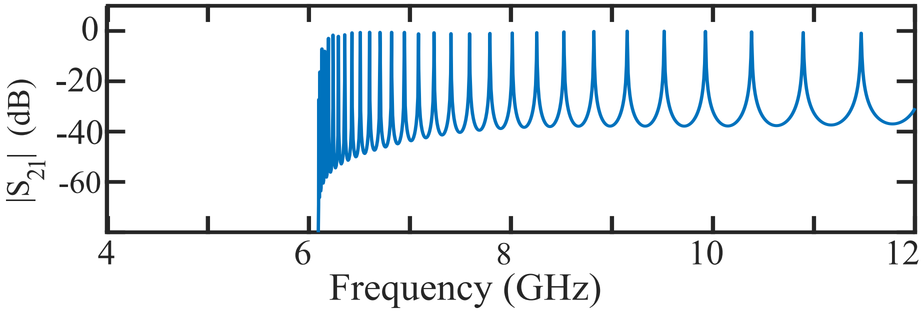

Figure 24: Transmission spectrum calculated from circuit simulation using AWR for a hybrid LHTL-RHTL resonator with parameters of the designed device B.

capacitor to the LHTL portion C_{cM}^{in} is formed with a 4.9-μm wide gap to the input feedline. The output end of the RHTL consists of an interdigitated capacitor C_{cM}^{out} for coupling to the output feedline. Near the output portion of the RHTL, the capacitor C_{QM} couples the transmon to the hybrid metamaterial.

The RHTL portion of the hybrid metamaterial resonator is formed from a 5-mm long CPW which is based on AWR simulations to maximize the coupling bewteen the qubit and modes in the 6-8 GHz region. Figure 24 shows the tranmission spectra of a hybrid LHTL-RHTL resonator calculated using AWR. Even with the presence of an RHTL component the spectra looks very similar when compared with the spectra of a pure LHTL resonator. More details of AWR simulations are provided in Section 7.4. A 10-μm wide center conductor and a 6-μm wide gap to the ground plane on either side of the CPW designed allow us to match the impedance (about 50 Ohms) between the LHTL and RHTL segments.

As described in the section 7.4, by making changes to the current design it should be possible to reach the regime where the coupling strength between the qubit and individual modes of the metamaterial resonator is larger than the mode spacing.

The metamaterial resonators with inductors on the one side of the LHTL were also designed (Device C). For the same 3.5-mm length, the maximum number of cells that could be physically implemented is 38 to allow enough spacing between adjacent meanderline inductors. Figure 25 shows the optical image of the LHTL resonator.

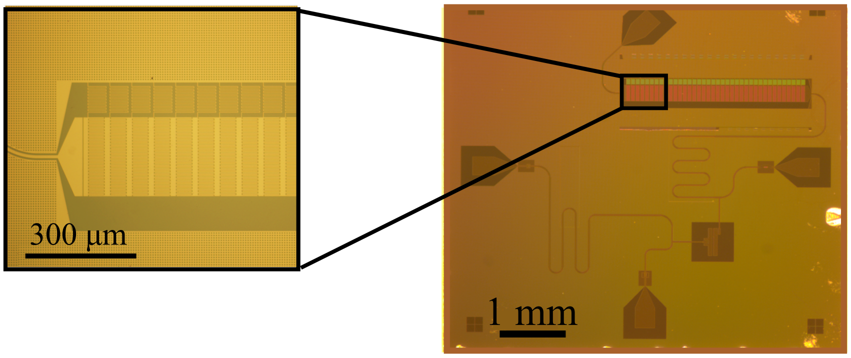

Figure 25: Optical micrographs of metamaterial resonator device with inductors on one side of the LHTL (Device C).

4.5 Fabrication Details

The devices were fabricated with two lithographic steps: photolithography and electron beam lithography. Photolithography was used to pattern most of the circuit elements of our device except the qubit junctions, which were patterned using e-beam lithography. The device which contained just the LHTL resonator (Device A) went only through the photolithography step.

Initially an 80-nm thick Nb film was sputter deposited onto a high-resistivity Si wafer. All of the circuit elements besides the qubit junctions were then patterned in a single photolithography step with UVN2300 deep-UV negative resist. After development, the pattern was etched using an inductively coupled plasma etcher with BCl_3, Cl_2, and Ar. For the devices where the metamaterial resonator was coupled to the transmon qubit, the junctions were defined with an electron-beam lithography step with a bilayer of MMA and PMMA to form the junction electrodes and airbridge for shadow evaporation. Following development in methyl isobutyl ketone and surface oxide removal using 13 sec Argon ion mill, the junctions were formed by double-angle depostion of Al thin films with 35 nm for the first layer and 65 nm for the second layer. The tunnel barriers were formed by an in situ oxidation step in between the two film depositions; the unwanted Al was lifted off using dichloromethane following the vacuum step. More detailed fabrication recipe is given in Appendix A.

Chapter 5

LHTL resonator measurements

In this chapter I summarize the measurements and main results for Device A, which is a 42-cell LHTL resonator. More details about the measurements and analysis can be found in Ref. [39] and Ref. [59]. In this work, the dense mode spectrum of the LHTL resonator is characterized extensively by both microwave transmission measurements and laser scanning microscopy (LSM). In particular, the measurements of mode frequencies, spatial profiles of current and charge densities, and damping due to external loading confirms that we can implement a LHTL resonator with tailored characteristics predicted by analytical (Chapter 3) and numerical modeling (Sec. 7.1).

5.1 Measurement setup

After we fabricate our devices on a high resistivity Si wafer following the steps mentioned in Appendix A.1, they are diced into a $4.25 \times 4.25\,\mathrm{mm}^2$ chips. A single chip is loaded into a printed circuit board (PCB) sample holder. [Fig. 27 (b)]. The launching pads on the chip are connected to the center traces of the board using aluminum wirebonds. To ensure a low-impedance connection at microwave frequencies between the device ground plane and the ground of the sample holder, we use numerous wirebonds that connect from the PCB ground plane to the perimeter of the chip and across different discontinuous sections of the ground plane of the chip. SMA connectors are used to connect the center traces to RF cables to the cabling on the cryostat. An aluminum lid is used to protect the chip from stray magnetic fields and black body radiation. The sample box is mounted on a cold finger made from OFHC copper on an Adiabatic Demagnetization Refrigerator (ADR) with a base temperature of around 50 mK. The sample box and the cold finger are shielded by a single-layer cryogenic μ-metal magnetic shield. The input line to the LHTL resonator is connected to the top of the ADR thorough semi-rigid cables with 39 dB of cold attenuation for thermalization. The output from the LHTL is amplified by 32 dB with a HEMT (CITCRYO01-12A, Bandwidth: 1-12 GHz) mounted on the 3 K plate of the ADR and again with a room-temperature amplifier (NARDA West) with 35 dB gain.

Transmission measurements across the LHTL resonators are performed using a vector network analyzer (VNA) (as shown in Fig. 28). We measure transmission using scattering paramater or S parameters, matrix. For a two port device, the S parameters are defined in terms of incident a_1, a_2 and reflected b_1, b_2 voltage waves [57]:

$$\begin{bmatrix} b_1 \\ b_2 \end{bmatrix} = \begin{bmatrix} S_{11} & S_{12} \\ S_{21} & S_{22} \end{bmatrix} \begin{bmatrix} a_1 \\ a_2 \end{bmatrix}. \tag{5.1}$$

In the measurement setup that we use, S_{21} characterizes the transmission through the resonator. When the load impedance is matched to the source impedance at the input end, S_{21} is reduced to [57]:

$$S_{21} = \frac{b_2}{a_1} = \frac{2V_2}{V_g}, \tag{5.2}$$

where V_g is the source voltage at port 1 and V_2 is the voltage measured at port 2. A detailed derivation for S_{21} for a LHTL resonator is provided in Ref. [39].

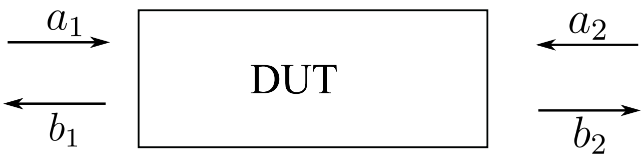

Figure 26: Schematic of a two port device under test (DUT).

Python scripts are used for programming the VNA to automate the measurements. A separate transmission measurement of a CPW feedline with the identical setup is performed to get a transmission baseline. However, small variations in baseline measurement can be expected due to slight chip-to-chip variations. Because a single Narda amplifier does not have enough bandwidth to cover the complete range of our measurements, we used two Narda amplifier with bandwidths 2-8 GHZ and 6-18 GHz and divided the transmission measurements from 2-8 GHz and 8-16 GHz where the appropriate Narda was used. Similarly, we divided the measurements for baseline transmission.

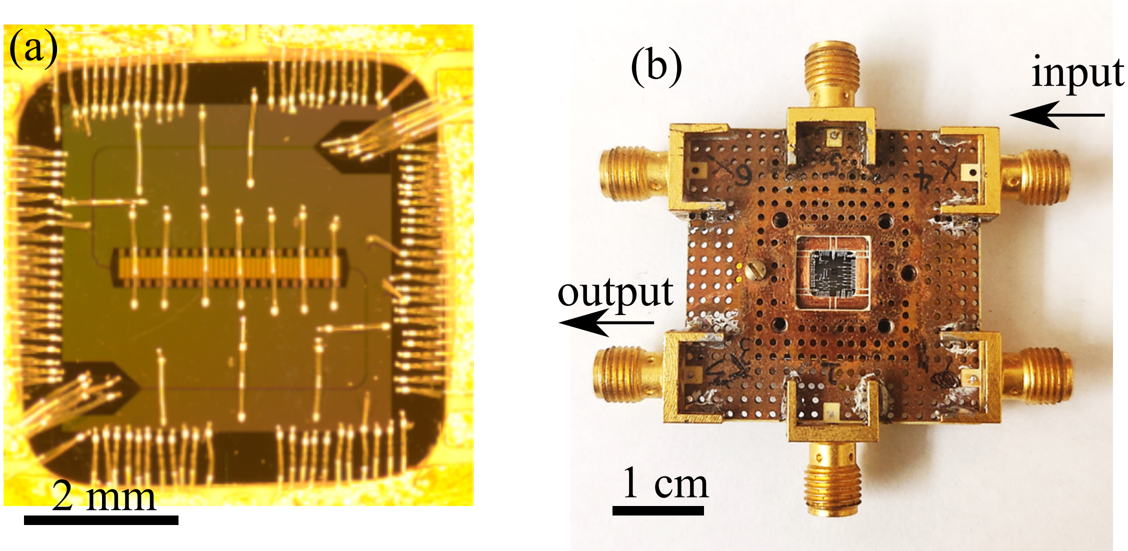

Figure 27: (a) Zoomed-out image of the chip fitting in the sample holder and the wirebonds; (b) the entire sample holder with chip bonded in place and input/output connections marked.

5.2 Mode structure of a LHTL resonator

In this section, we present measurements for one of our LHTL resonators at two different temperatures: 65 mK and 3 K with input power of ∼ -90 dBm applied on the input end of the sample.

Figure 29 is the calibrated measurement results: black solid line is the base temperature, while the blue dashed line is the high temperature result. At both 65 mK and 3 K, the spectrum shows a large number of peaks. The transmission below the first peak at 4.245 GHz is quite low. We see that peaks are very closely spaced in the region between 5-8 GHz. The measured smallest mode spacing is 147 MHz between

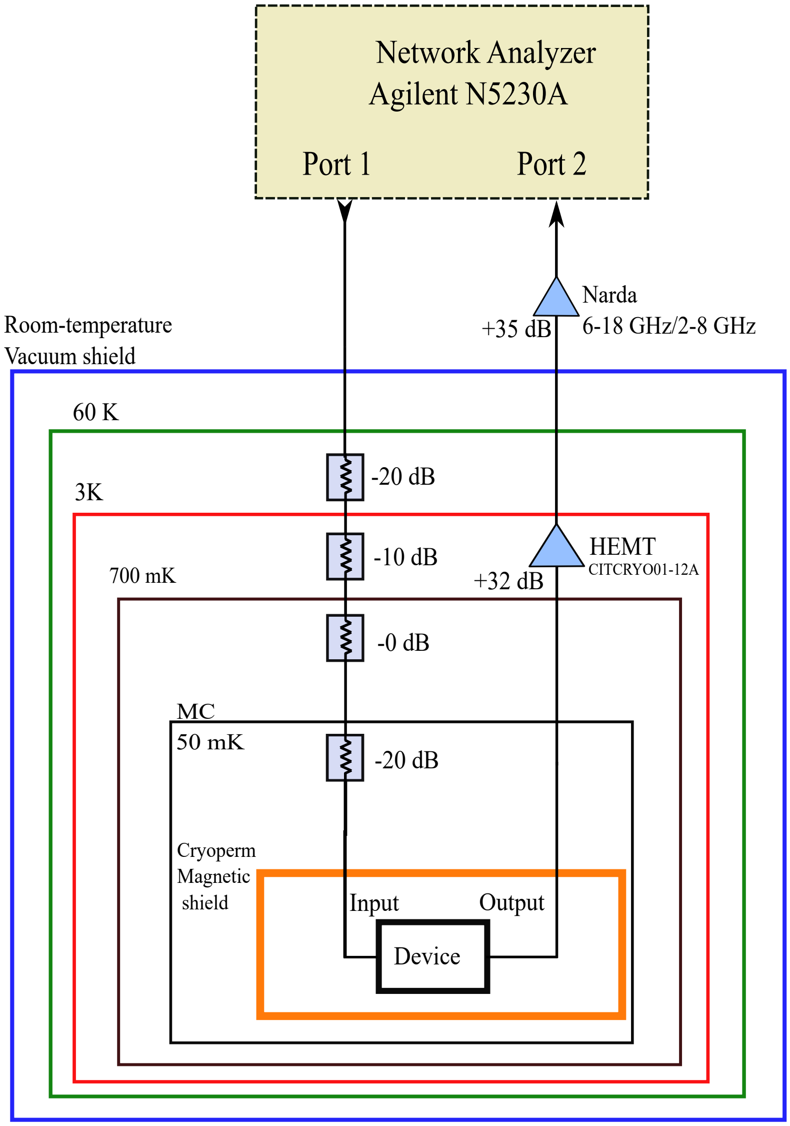
Network Analyzer
Agilent N5230A
Port 1
Port 2
Narda
6-18 GHz/2-8 GHz
+35 dB
Room-temperature
Vacuum shield
60 K
-20 dB
3K
-10 dB
HEMT
CITCRYO01-12A
700 mK
+32 dB
-0 dB
MC
50 mK
-20 dB
Cryoperm
Magnetic
shield
Input
Output
Device

Figure 28: Transmission measurement setup including the wiring inside the ADR.

mode 39 and 38. With the exception of the first few modes, we see that the spacing between the modes increases with frequency, as predicted by theory 13. The highest Q we measure at base temperature is around 26,000 for mode 40. The bandwidth of our HEMT, which is roughly 2-16 GHz, limits the highest frequency mode that we can measure, which is around 15 GHz. Figure 29(b) shows the transmission measurement for mode 39, and a negative shift in the resonance frequency can be seen at

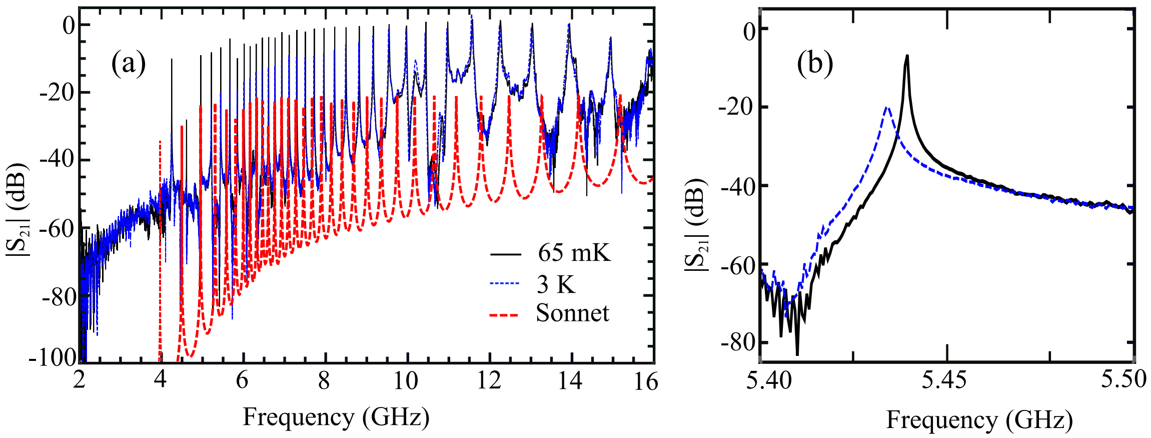

Figure 29: (a) Measurements of the magnitude of the microwave transmission $|S_{21}(f)|$ on the ADR at two different temperatures: 65 mK (solid black line); 3 K (blue dashed line); Sonnet simulation (red dashed line) offset by 20 dB; (b) an enlarged plot in the vicinity of $n = 38$ mode near 5.41 GHz. Figure taken from Ref [39].

higher temperature due to the increase in kinetic inductance [82], which is a consequence of temperature dependence of the number density of cooper pairs relative to the number density of unpaired conducting electrons [83]. Q for the modes remains high at low temperatures that are substantially far away from the T_c of Nb around 9 K [84]. A decrease in Q at high temperature is also seen due to an increased population of thermal quasiparticles. The chip is characterized at 3 K to help interpreting the results from LSM images presented in Sec. 5.4. Figure 30(a) shows the plot for mode frequencies vs normalized wavenumber measured at 65 mK in the ADR. The plot shows good agreement between the mode frequency found with the ADR and LSM measurements and the mode frequencies obtained from Eq. (3.29), numerical circuit simulations using AWR (Sec. 7.1), and finite-element device simulations using Sonnet (Sec. 7.1) except at the lowest frequency modes [Fig. 10(b)], where there are more significant deviations.

5.3 Coupling and Internal Losses

Since we want to couple LHTL resonators to other devices such as a superconducting qubits, it is crucial to understand how the internal and coupling Q depends on mode frequency. In this section I discuss how the internal and coupling Q were extracted

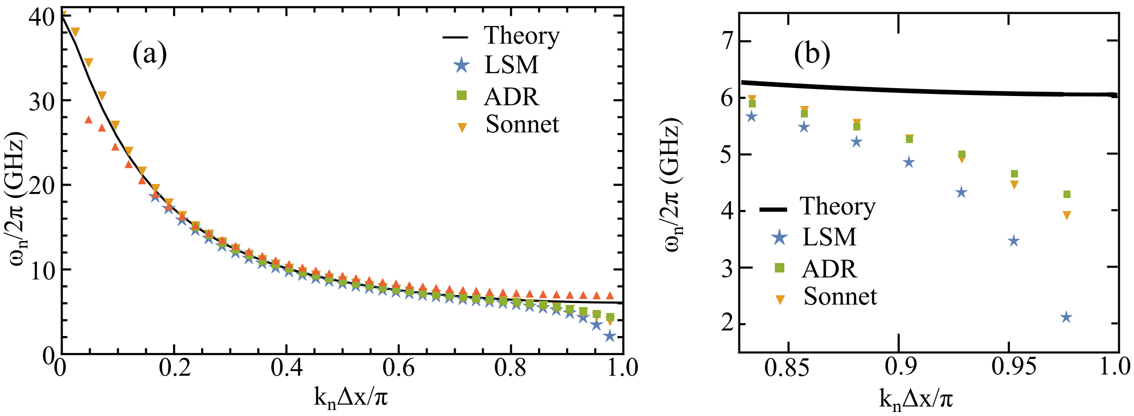

Figure 30: (a) Plot of mode frequency vs. normalized wavenumber for ADR measurements, LSM images, Sonnet simulations; the solid black curve corresponds to dispersion relation of Eq. (3.29). (b) Closeup of behavior near $\omega_{IR}/2\pi$. Figure taken from Ref [39].

from the measured data and how they compare with the theory and simulations.

After measuring $S_{21}(f)$ for a particular mode, to extract Q_i and Q_C simultaneously, $S_{21}(f)$ can be fitted in the complex plane to a standard function, as described in literature [85, 86, 87]:

$$S_{21} = \frac{Q}{Q_C}\frac{e^{i\phi}}{1+2iQ(f-f_0)/f_0}, \tag{5.3}$$

where Q, Q_C, f_0 and ϕ are the total quality factor, the coupling quality factor, the mode frequency and the rotation angle of the resonance circle on the complex plane, respectively. The Internal quality factor can then be calculated as $Q_i^{-1} = Q^{-1} - Q_C^{-1}$.

This method works well for the absorption type resonance for which the transmission away from the dip is unity, and thus yields a self calibrated baseline [88].

However, for peak-style transmission resonances, also applicable for our LHTL resonator measurements, a separate baseline calibration is required in order to separate the values of Q_i and Q_c from the fit. The accuracy of the fit depends on the baseline measurements, which inevitably introduce some variation since they must be performed on a separate cooldown with a different device that may have slight differences in the bonding and packaging.

The modes of our LHTL resonator in overcoupled regime, where $Q_C \ll Q_i$, thus it is difficult to extract Q_i as a small change in baseline will result in big change of

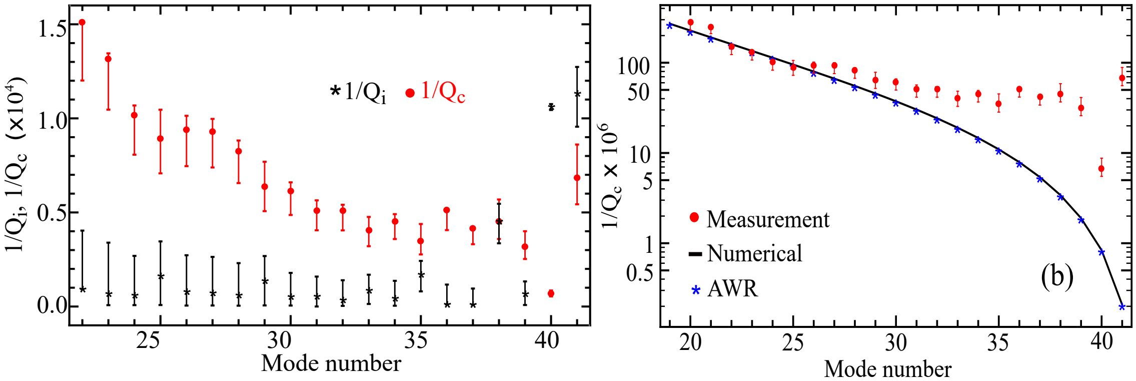

Figure 31: (a) Comparison of internal loss and coupling loss extracted from measured $S_{21}(f)$; (b) The external loss plot on a log scale for the measurement at 65 mK compared with AWR simulation, Sonnet simulations of both staggered and non-staggered inductor configuration, and theoretical dependence calculated from Eq. (5.4) Figure taken from Ref [39].

the Q_i. We estimate an uncertainty in the baseline level of $\pm 2\ dB$ and use this to compute uncertainties in the Q_i values extracted from the fits. For the cases, where a resonance peak goes higher than 0 dB which is physcally immpossible for passive a device, we adjust baseline to 0 dB. Figure 31(a) shows the extracted values of Q_i^{-1} and Q_C^{-1} for LHTL resonator. For most of the modes of the LHTL, Q_i^{-1} values are around 10^{-5}, which is typical for the devices where dielectric loss at the substrate surface and interfaces dominates [89, 90], as in our devices where the interdigitated capacitors make up a significant portion of the LHTL resonator. The Q_c^{-1} values generally decrease for larger n modes, which is quite different from the trend for a conventional right-handed transmission-line resonator, where the $Q_c^{-1} \propto n$ [56]. In Appendix D of Ref. [39], we derive expressions for Q_c for resonators formed from discrete lumped-element transmission lines, with both right-handed and left-handed dispersion relations. For the simplest case of an ideal LHTL resonator, we obtain

$$Q_c^{LHTL}(n)^{-1} = \frac{C_c^2 \cos^2\left(\frac{n\pi}{2N}\right)}{2NC_l^2 \sin^3\left(\frac{n\pi}{2N}\right)}, \tag{5.4}$$

where n is the mode number, N is the total number of cells, C_c is the coupling capacitor, and C_l is the capacitance of a unit cell.

In Fig. 31(b), we plot $Q_c^{-1}(n)$ from Eq. (5.4), along with values from a numerical simulation of an ideal lumped-element LHTL resonator using AWR Microwave Office showing nearly perfect agreement. The Q_c^{-1} values extracted from our measured resonances agree reasonably well with Eq. (5.4) for lower values of n, but begin to deviate significantly for higher n modes starting around $n \sim 30$. Q_c^{-1} extracted from finite element simulations using Sonnet with two configurations are also studied. Q_c^{-1} extracted for the staggered inductor configuration using Sonnet shows a similar deviation of Q_c at large n compared to our measured values. Q_c^{-1} extracted for the non-staggered inductor configuration matches closely with AWR simulations and Eq. (5.4). This effect is likely a consequence of the short wavelengths for these high-n modes, which are strongly influenced by the layout of the inductors,the kinetic inductance of the capacitors, as well as the integrity of the ground plane across the chip [39].

5.4 LSM imaging of mode structure

In this section, I describe low-temperature laser-scanning microscope (LSM) images of our LHTL resonators performed by our collaborators Alexander Zhuravel and Alexey Ustinov at the Karlsruhe Institute of Technology. LSM imaging provides a direct measurement of the spatial distribution of microwave fields in a superconducting circuits. This technique is quite useful for studying the mode structure of the various resonances in our LHTL resonators.

LSM has been used previously to image a wide variety of superconducting structures under rf excitation [91, 92]. The various modes of LSM operation have been described in detail in Refs. [93] and [94]. The LSM microsopy is based on the fact that we can observe a change in a global property, like S_{21} of a superconducting circuit, by a local perturbation caused by the local deposition of laser energy over a small area of a superconducting device. The change in the global response depends on the local microwave field distribution in the focused area where the energy is deposited. An image of the photoresponse $\mathscr{R}(x, y, f)$ can be produced by raster scanning the laser probe over the surface of the sample while modulating the beam intensity. The modulated signal is measured using a lock-in technique by correlating the output signal as a function of the location of the laser spot.

The jumper wirebonds are removed across the chip so they do not block the laser

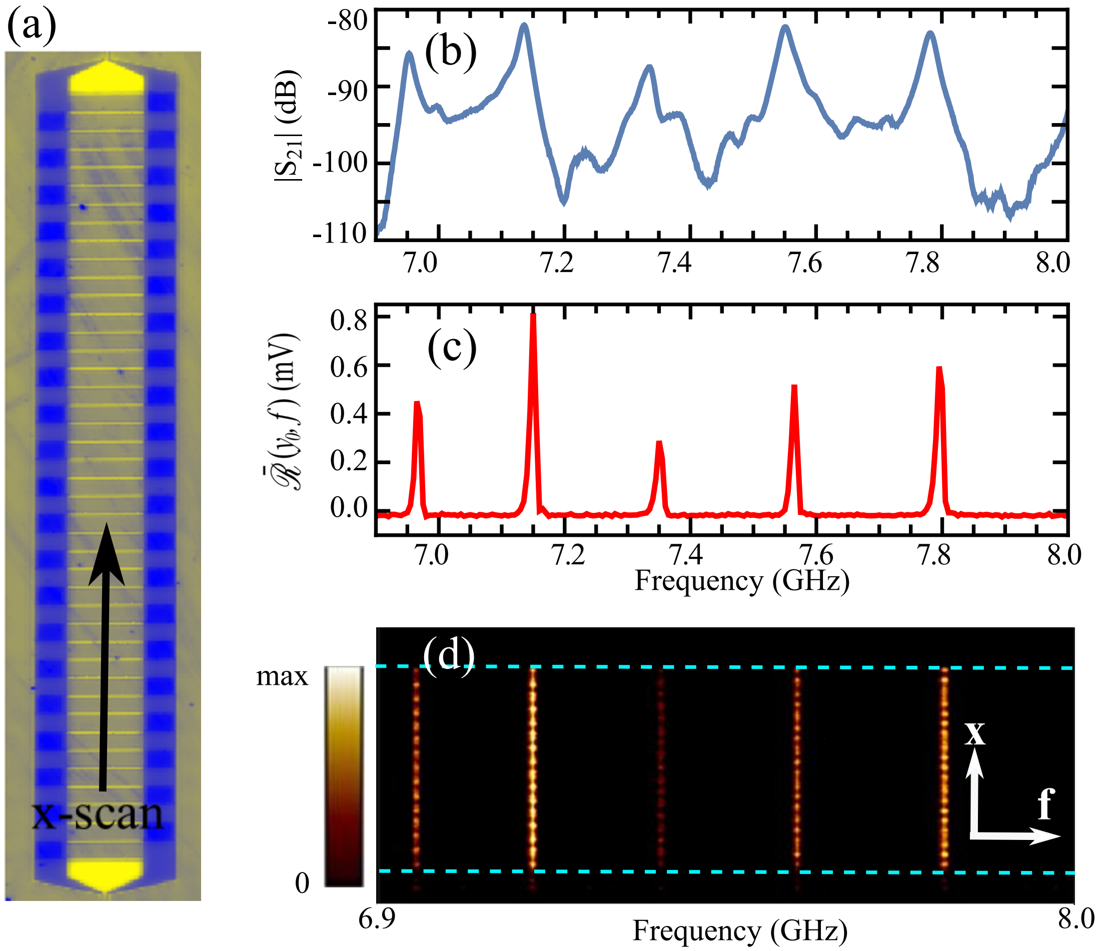

Figure 32: LSM reflectivity image with the arrow indicating the direction of 1D line scans. (b) Microwave transmission (not normalized) $|S_{21}(f)|$ measured on LSM. (c) Average LSM photoresponse $\overline{\mathscr{R}}(y_0, f)$ along 1D line scans. (d) 1D line scans $\mathscr{R}(x, y_0, f)$ vs. frequency; dashed horizontal lines indicate location of input and output coupling capacitors. Figure taken from Ref [39].

beam from reaching the surface of the chip. The chip along with the sample holder is mounted inside a vacuum chamber of a cryostat with optical access. The temperature of the cryostat was kept about 5 K, which is well below the T_C of Nb. The focused beam is produced by a diode laser with wavelength 640 nm. The beam is focused to a spot of about 12-μm diameter on the surface of the chip, which results in a power deposition of approximately 10 μW and an increase of the local temperature.

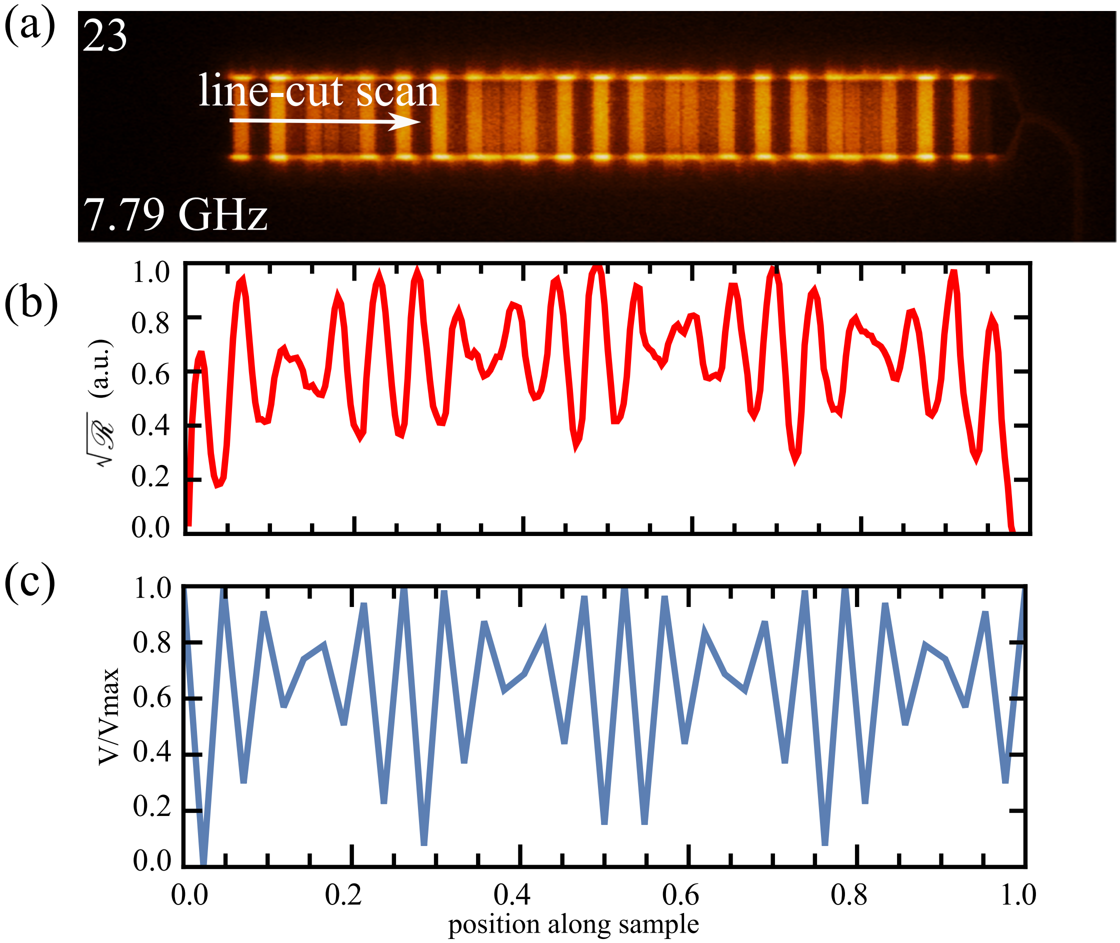

Figure 33: (a) LSM photoresponse for mode 23 with the arrow indicating the location of subsequent line cut. Bright (dark) regions correspond to large (small) PR signal. (b) Plot of the square root of LSM photoresponse signal along line cut. (c) Standing-wave pattern of voltage across capacitors computed with Eq. (E3) in Ref. [39] for mode 23 of a 42-cell LHTL resonator. Figure taken from Ref [39].

The intensity of the laser is modulated at 100 kHz while the change in microwave transmission $|\Delta S_{21}(f)|$ is measured. The output signal from the sample is carried out using semi-rigid coaxial cables to an amplifer(60 dB), a crystal diode rectifier and the lock-in amplifier. The Photoresponse signal is produced by lock-in detection at the modulation frequency.

Figure 32(a) contains a reflectivity image of the metamaterial in the LSM, with an arrow indicating the orientation and location of 1D scans along the x axis of the photoresponse that are measured in the LSM. The photoresponse signal averaged over the length of the resonator $\overline{\mathscr{R}}(y_0, f)$ [Fig. 32(c)] and microwave transmission $|S_{21}|$(Fig. 32(b)) are measured simultaneously as a function of frequency.

The peaks in $\mathscr{R}(x, y_0, f)$ in Fig. 32(c) coincide with the mode resonances in the $S_{21}(f)$ measurements from Fig. 32(b), thus indicating that $\mathscr{R}(x, y_0, f)$ can be used to investigate the metamaterial resonances and the corresponding standing-wave patterns.

We then perform 2D scans of $\mathscr{R}(x, y, f)$ while exciting one of the metamaterial modes at a time. [Fig. 33(a)]. We see the large photoresponse where we expect large microwave currents particularly in the inductors near the current antinodes in the standing wave pattern. We also see a large phtoresponse in the regions where we expect large microwave voltages around the capacitors near the standing-wave antinodes for charge density. A linecut along the length of the LHTL resonator can be used to generate a 1D plot of $\sqrt{\mathscr{R}}(x, y_0, f)$ as function of position along the resonator [Fig. 33(c)]. We see that this curve is in good agreement with the theoretical curve 33(c)] generated by the voltage vs. position relation derived in Appendix E of Ref. [39]

The LSM imaging is repeated for all of the modes in our LHTL below 20 GHz and Fig. 34 contains an array of LSM images for many of these modes. We observe that for mode $n \leq$21 the number of nodes decreases with an increase in frequency i.e., the wavenumber is a falling function of frequency. However, we also see an increase in the number of antinodes from $n =$41 to 21, which is what one would expect for a transmission-line resonator with right-handed dispersion. As described in Section V of Ref. [39], this can be understood as an undersampling effect due to the discrete lumped-element nature of our metamaterial transmission line and the fact that the LSM image is only sensitive to intensity and not phase.

In conclusion, we have shown that we can fabricate and characterize LHTL resonators with tailored dispersion relations whose properties can be well understood analytically and through numerical simulations.

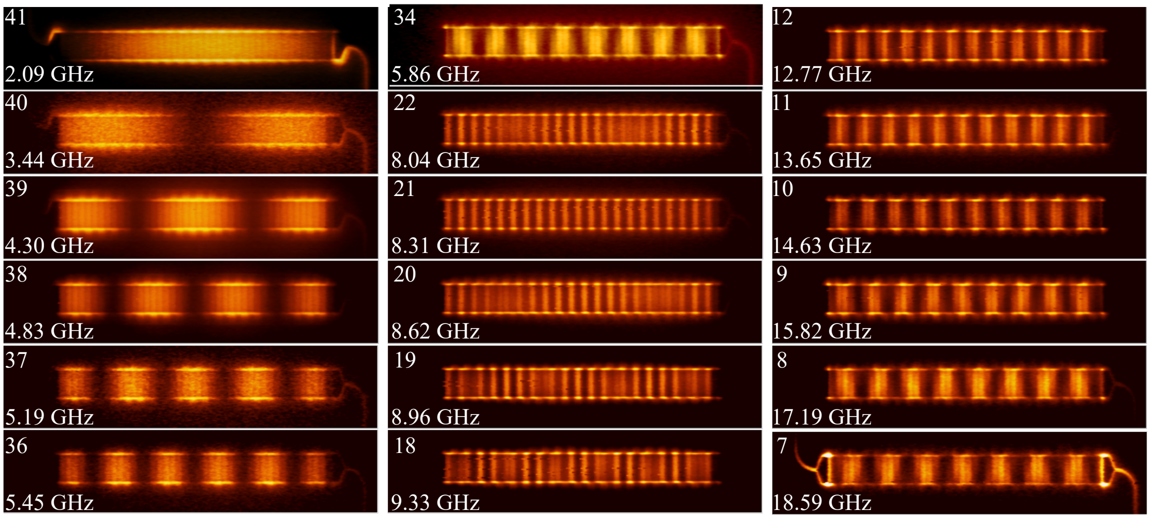
41
2.09 GHz
40
3.44 GHz
39
4.30 GHz
38
4.83 GHz
37
5.19 GHz
36
5.45 GHz
34
5.86 GHz
22
8.04 GHz
21
8.31 GHz
20
8.62 GHz
19
8.96 GHz
18
9.33 GHz
12
12.77 GHz
11
13.65 GHz
10
14.63 GHz
9
15.82 GHz
8
17.19 GHz
7
18.59 GHz

Figure 34: Array of LSM images of metamaterial for different modes, labeled by mode number and frequency. Bright (dark) regions correspond to large (small) PR signal. Amplitudes of photoresponse signal are normalized for best contrast. Figure taken from Ref [39].

Chapter 6

Measurements of a qubit coupled to a metamaterial resonator

In this chapter, I discuss in detail about the various measurements for Device B that has a transmon is coupled to a metamaterial resonator. The interaction between the transmon and metamaterial is measured by both the transmission response of the metamaterial resonator and direct qubit characterization with a separate readout resonator.

6.1 Measurement setup

The device is diced into a $6.25 \times 6.25\,\mathrm{mm}^2$ chip. Using a small amount of GE varnish, the chip is glued into a square pocket of a machined aluminum sample box. GE vanish assists with the thermalization of the chip at low temperature and prevents the chip from moving inside the pocket. The on-chip launching pads are connected to the PCB traces by aluminium wirebonds. A large number of wirebonds are connected between the perimeter of the chip and the ledge of the pocket in the aluminum box to ensure good grounding of the chip. The length of wirebonds is kept short (<1 mm) to minimize their inductance. The sample box is covered by an aluminum lid with an integrated superconducting wirewound coil (Fig. 35). The sample box is mounted on the cold finger of a dilution refrigerator. A single-layer cryogenic magnetic shield is used to shield the device from external magnetic flux noise. The output from the network analyzer (Fig. 37) is connected to the SMA port on the top of DR.

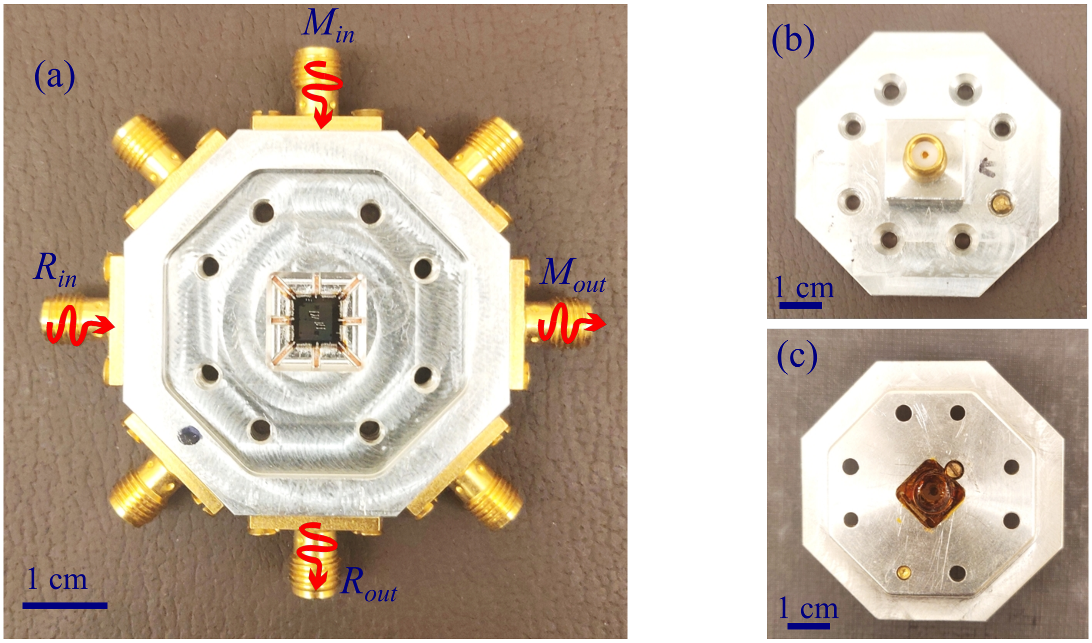

Figure 35: (a) Aluminum sample box with the device wirebonded in the center. (b) Top view of the lid of the sample box; SMA port is used to connect the DC bias of the superconducting coil. (c) Bottom view of the lid. In the center superconducting coil can be seen which is made from 150 turns of NbTi wire.

Figure 36 shows the wiring inside the dilution refrigerator. Inside the fridge signal is carried to M_{in} port [Fig. 35(a)] with semi rigid cables and 50 dB of cold attenuation and low pass filter. The output from port M_{out} passed through filters and isolator and amplifed by HEMT (Model: CITCRYO01-12A, Gain: +32dB, Bandwidth: 1-12 GHz) and room temperaure amplifier (Model: NARDA West, Gain +35 dB, , Bandwidth: 2-8 GHz/6-18 GHz) by about 65 dB (As shown in Figs. 36 and 37). A dilution refrigerator (DR) can maintain base temperature continuously for several weeks to several months. Modern dilution refrigerators are cryogen-free, that is, they do not require liquid nitrogen and liquid helium to cool from room temperature to 4 K. However, this chip was measured on an conventional wet dilution refrigerator. DR runs on a conventional ^{3}He/^{4}He process to reach of base temperature of about 25 mK [95].

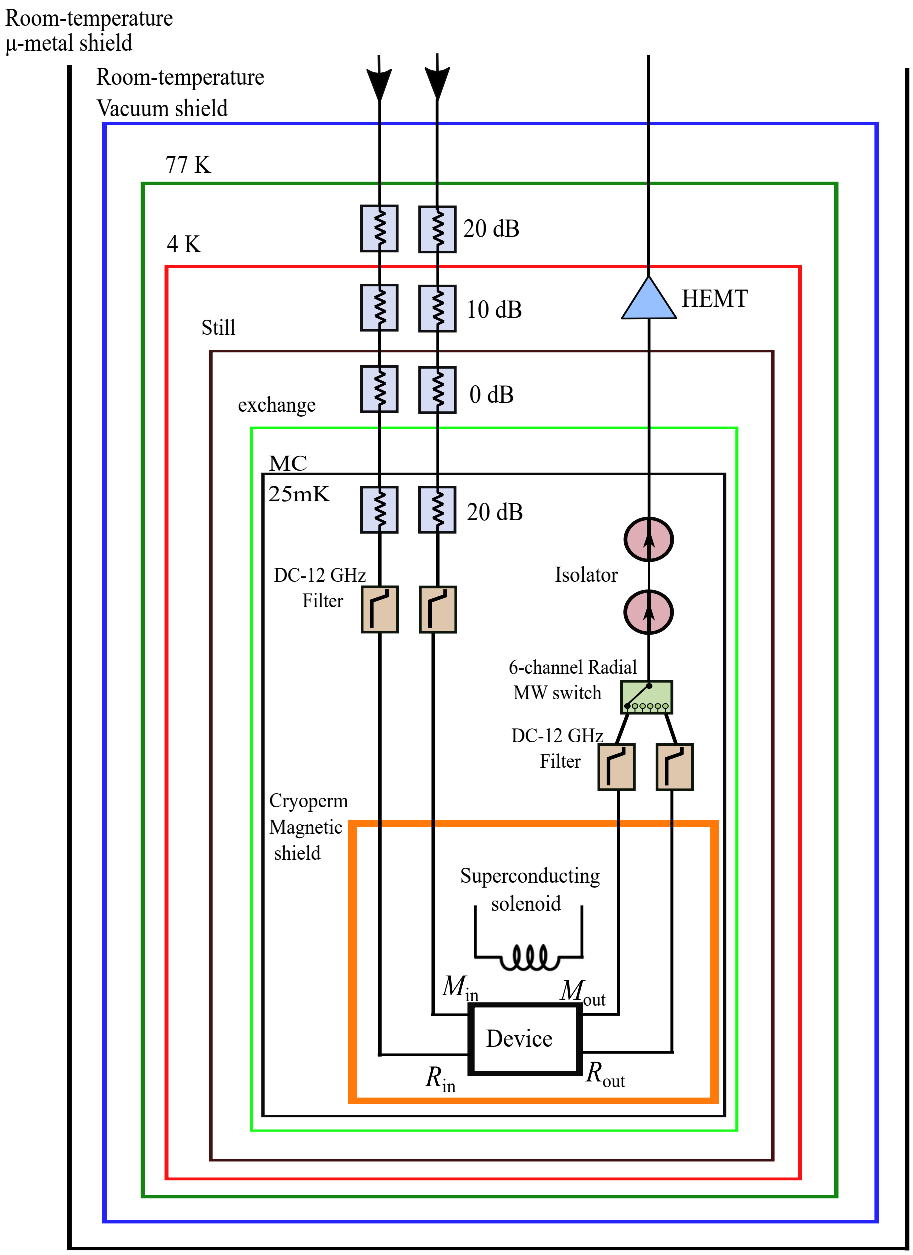
Room-temperature
µ-metal shield
Room-temperature
Vacuum shield
77 K
4 K
Still
exchange
MC
25mK
20 dB
10 dB
0 dB
20 dB
HEMT
DC-12 GHz
Filter
Isolator
6-channel Radial
MW switch
DC-12 GHz
Filter
Cryoperm
Magnetic
shield
Superconducting
solenoid
M_{in}
M_{out}
Device
R_{in}
R_{out}

Figure 36: Wiring inside the dilution refrigerator. The input for metamaterial resonator and input resonator, each go thorough 50 dB of attenuation and a low pass filter. The output signal from the device go through a low pass filter, a microwave switch, isolators and a HEMT amplifier mounted at 4 K stage.

Figure 38 shows the schematic for the hardware setup used for measurements involving qubit characterization and qubit interaction with the metamaterial resonator.

A separate transmission measurement of a CPW feedline with an identical setup is performed to get a transmission baseline. Qlab software that was developed by BBN is used for measurement and instrument control. This software uses a combination of Matlab and Python scripts for the parameter configuration interface and instrument control. The Quantum Gate Language (QGL) module, a part of QLab package, is used for pulse sequence generation [96] for different qubit characterization experiments (Fig. 45).

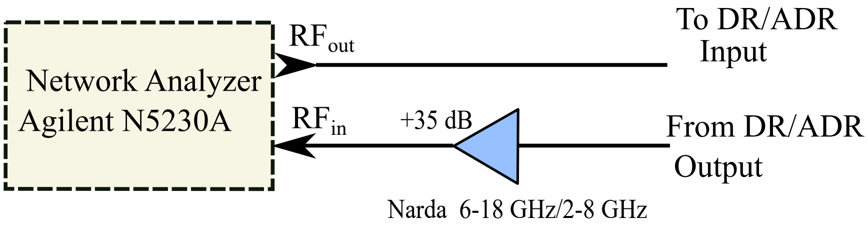

Figure 37: Transmission measurement for initial characterization of device spectra setup using a network analyzer.

6.2 Mode structure of hybrid LHTL-RHTL metamaterial resonators

For the initial characterization of the device spectrum, we measure the microwave transmission $S_{21}(f)$ with a vector network analyzer. Figure 39 shows the measured and simulated transmission spectrum for Device B. Even with the presence of a RHTL segment in the metmaterial resonator, the transmission spectra look similar when compared with measured and simulated spectra of a pure LHTL resonator (Fig. 30). For both configurations we see transmission is quite low at low frequencies, and there is a dense region of peaks between $\sim 6-8$ GHz. The infrared cutoff $\omega_{IR}/2\pi$ is around 5 GHz. The spacing between the modes increases with frequency except for the first few modes due to the staggered configuration of inductors as discussed in previous chapter. From this $S_{21}(f)$ measurement we extract the mode frequencies and plot them as a function of normalized wave number in Fig. 40. We also plot the dispersion relation calculated from circuit simulation using AWR with same device parameters.

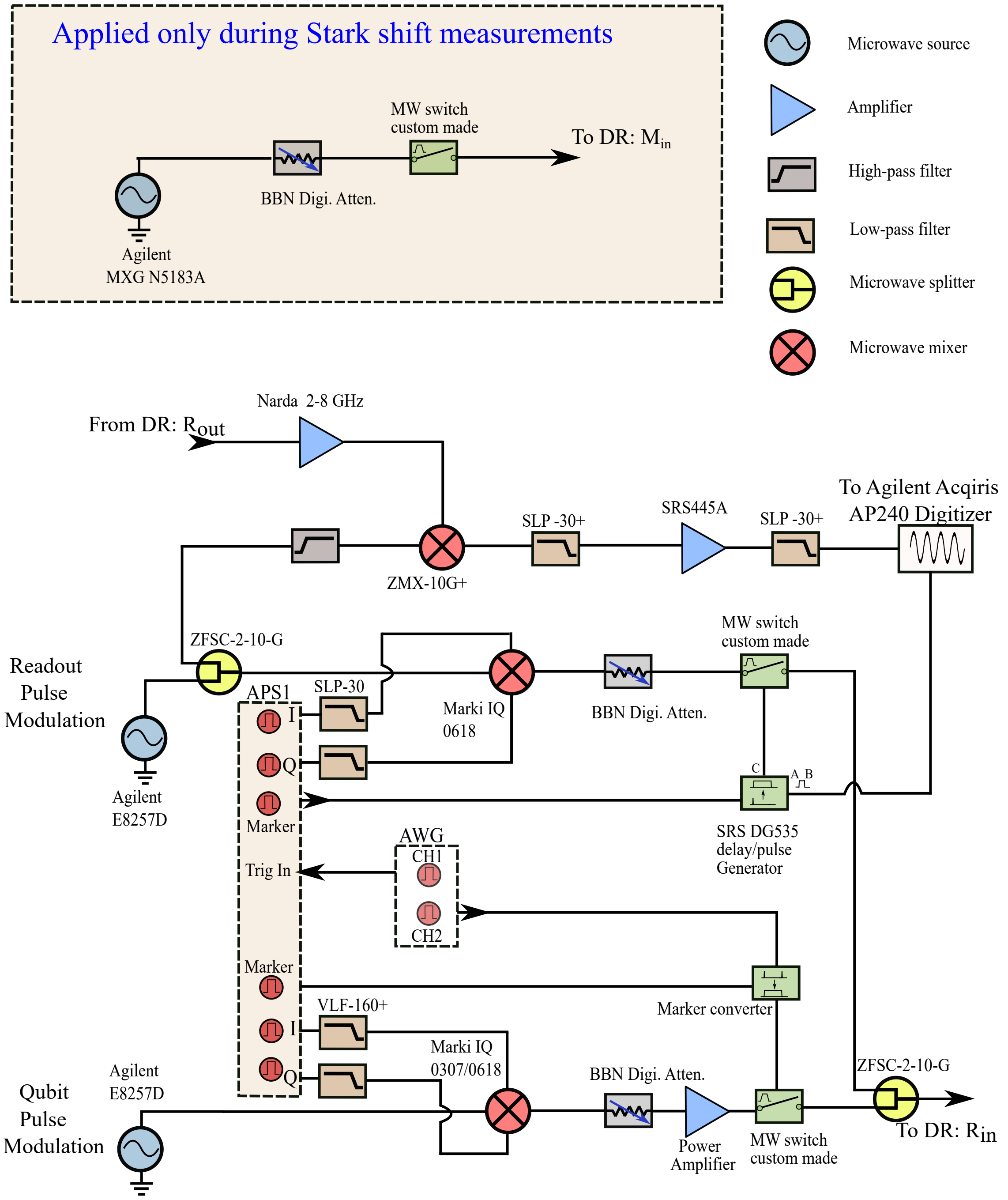
Applied only during Stark shift measurements
MW switch custom made
To DR: M_{in}
BBN Digi. Atten.
Agilent MXG N5183A
Microwave source
Amplifier
High-pass filter
Low-pass filter
Microwave splitter
Microwave mixer
Narda 2-8 GHz
From DR: R_{out}
To Agilent Acqiris AP240 Digitizer
SLP -30+
SRS445A
SLP -30+
ZMX-10G+
ZFSC-2-10-G
MW switch custom made
Readout Pulse Modulation
APS1
SLP-30
I
Q
Marki IQ 0618
BBN Digi. Atten.
C
A B
Agilent E8257D
Marker
SRS DG535 delay/pulse Generator
AWG
CH1
Trig In
CH2
Marker
Marker converter
VLF-160+
I
Q
Marki IQ 0307/0618
Agilent E8257D
BBN Digi. Atten.
ZFSC-2-10-G
Qubit Pulse Modulation
Power Amplifier
MW switch custom made
To DR: R_{in}

Figure 38: Measurement setup for qubit spectroscopy and characterization.

Since the metamaterial resonator is coupled to outside circuitry with relatively large input C_{cM}^{in} and output C_{cM}^{out} capacitors, the modes are in the overcoupled regime

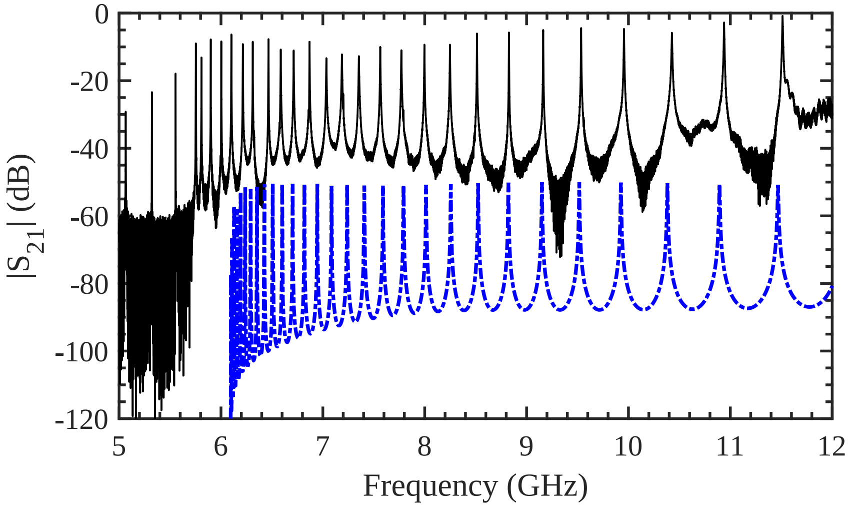

Figure 39: Measured transmission spectrum (black line) for Device B compared with spectrum from circuit simulation using AWR (blue dashed line, with -50 dB for clarity). Figure adapted from Ref. [97].

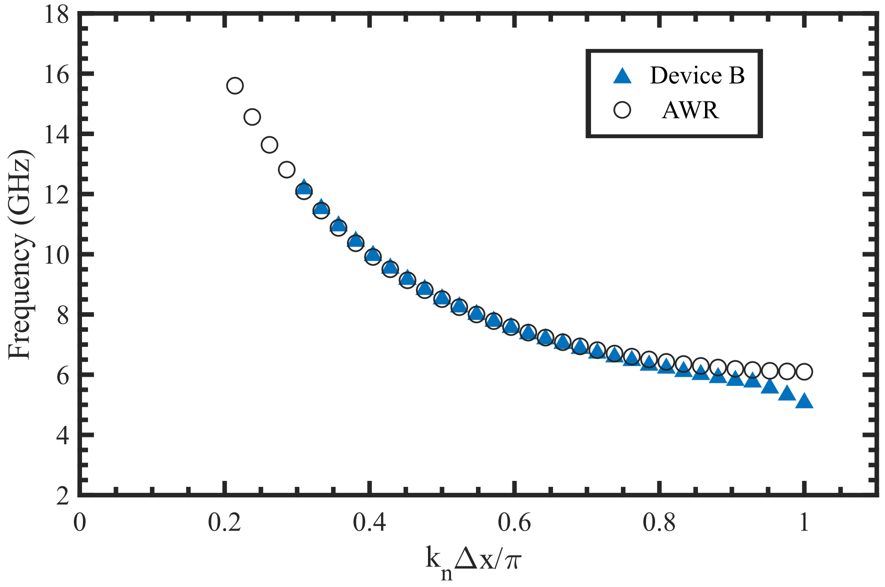

Figure 40: Dispersion relation obtained from S_{21} measurement of Device B compared with dispersion obtained from AWR simualtion with same parameters.

($Q_i \gg Qc$) and the total quality factor (Q) of the modes is dominated by the coupling quality factor ($Q_{total} \approx Q_c$). We extract the total quality factor of the modes by four

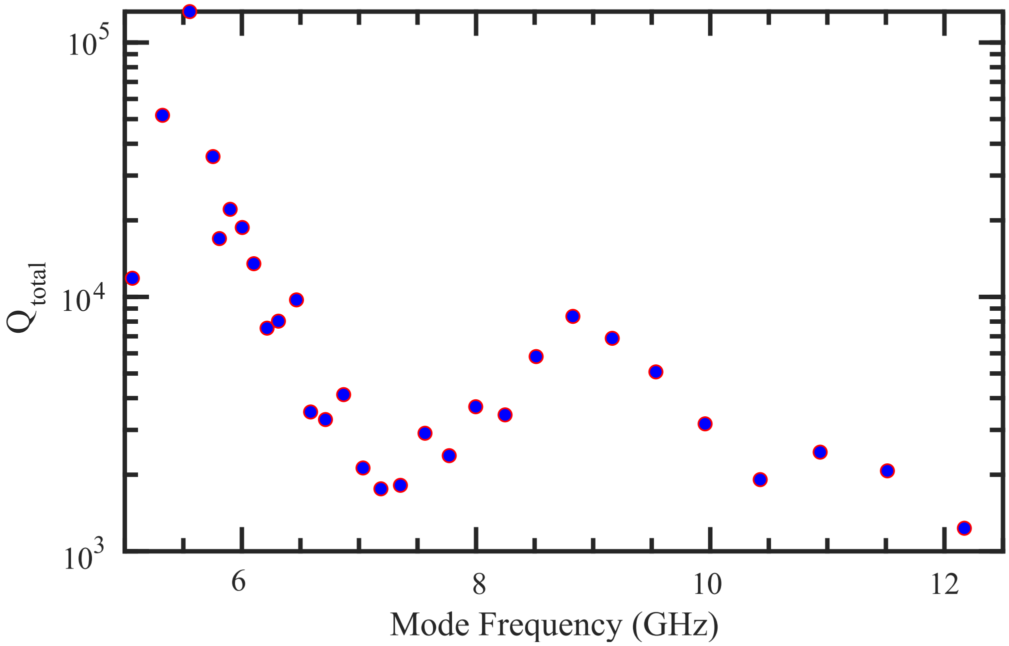

Figure 41: Measured total quality factor of metamaterial modes as function of frequency. The presence of the RHTL segment that is used to couple the metamaterial to the qubit results in the non-monotonic behavior of the mode quality factor vs. frequency through the variation in the standing-wave pattern in the RHTL portion with frequency; by contrast, a simple LHTL resonator exhibits a monotonic decrease in quality factor for increasing frequency (Fig. 31). Figure taken from Ref. [97].

parameter fit of transmission magnitude $|S_{21}(f)|$ to a simple Lorentzian

$$|S_{21}(f)| = \frac{A}{1+\left(\frac{f-f_0}{\kappa}\right)^2} + C, \tag{6.1}$$

where f_0 is the resonance frequency, A is the amplitude of the peak and C is the baseline offset. From the fit, we extract total quality factor $Q_{total} = f_0/2\kappa$ and 2κ is full width at half maximum (FWHM) or the 3 dB width (when $|S_{21}|$ is plotted on a log scale) of the resonance peak.

When compared to an ideal LHTL, where Q_{total} generally decreases as the mode frequency increases, we see additonal structure in Q_{total} as a function of mode frequency for our hybrid LHTL-RHTL metamaterial resonator. Q_{total} first decreases, then from 7 to 8.5 GHz, Q_{total} increases by almost an order of magnitude, before going down again for the modes higher than 8.5 GHz. This additonal structure is caused by standing-wave structure in the RHTL section and the location of local maxima in $Q_{total}(f)$ is determined by the resonant mode frequency of the RHTL section, which is determined by its length and wave speed [56].

6.3 Probing metamaterial modes coupled to a qubit

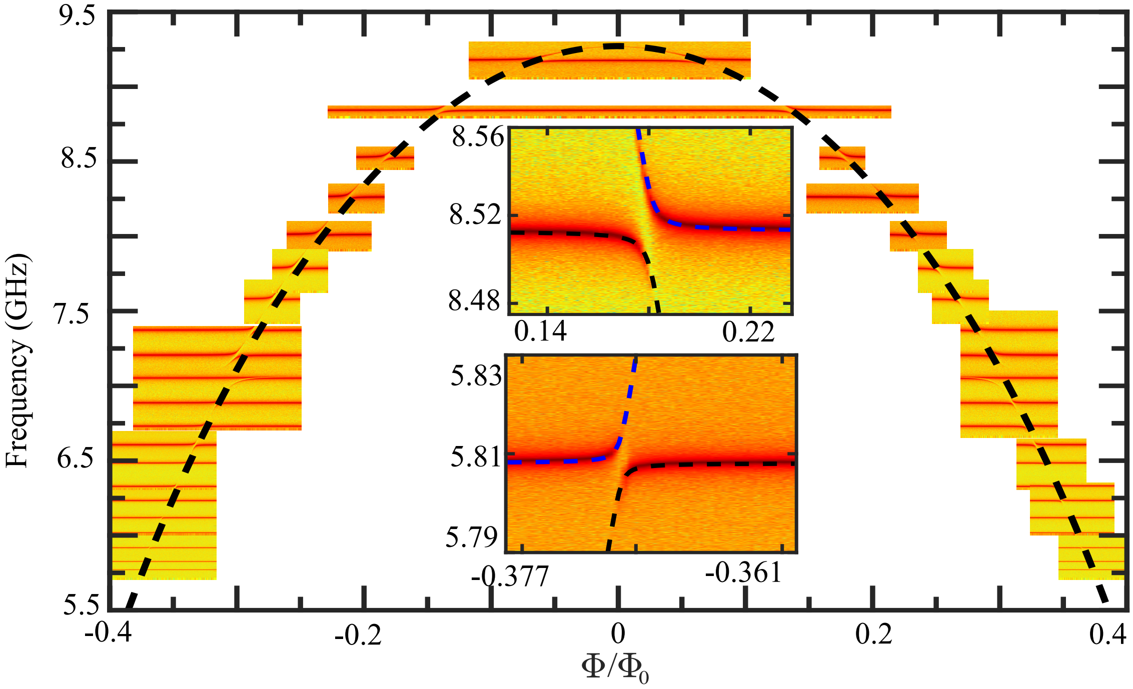

Figure 42: Density plot of magnitude of transmission through metamaterial resonator vs. qubit flux bias, showing vacuum Rabi splittngs for all of the modes that the qubit tunes through. Dashed line indicates flux tuning of bare transmon energy band from fits to splitting location. (Insets) closeup of splittings and fits for 5.81 GHz and 8.52 GHz modes. Figure taken from Ref. [97].

In this section, we see how the presence of a transmon qubit can affect the modes of the metamaterial resonator. Initially we probe the qubit indirectly through transmission measurements of the metamaterial, rather than using the separate readout resonator. Near one of the modes, we measure transmission $S_{21}(f)$ at low input power (around -100 dBm at the chip). By varying the flux bias to tune the qubit transition frequency, we are able to observe the influence of the qubit on each mode through

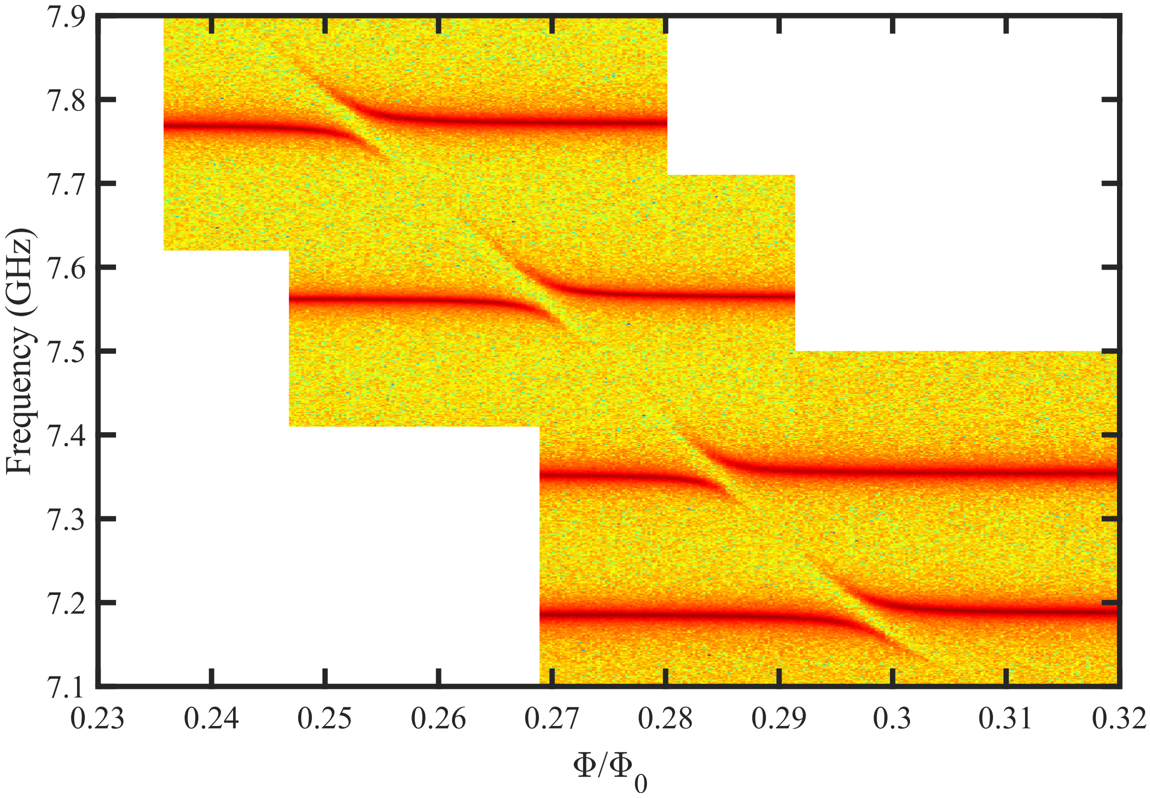

Figure 43: Detail of splittings for four adjacent modes between 7.1 and 7.9 GHz. Figure taken from Ref. [97].

which it passes. Next we tune the qubit frequency by changing the flux bias of the superconducting coil (Fig. 36). When the bare qubit frequency approaches each resonance peak, we observe a vacuum Rabi splitting [98] in the microwave transmission, where the qubit hybridizes with the photonic state of the metamaterial resonant mode [Insets of Fig. 42 and Fig. 43].

As we tune the qubit frequency, it crosses 21 modes up to the mode at 9.16 GHz, suggesting that the maximum qubit frequency is between 9.16 GHz and 9.56 GHz (frequency of next mode, which does not have any splitting) at an integer flux quantum ($\Phi_0 \equiv h/2e$, where h is Planck's constant and e is the electron charge). Through direct qubit spectrosopy spectroscopy with the use of the readout resonator, which will be discussed later in Sec. 6.4, we confirm that the maximum qubit frequency is 9.25 GHz (Fig. 47). We combine the plots of all the splitings on a single plot as shown

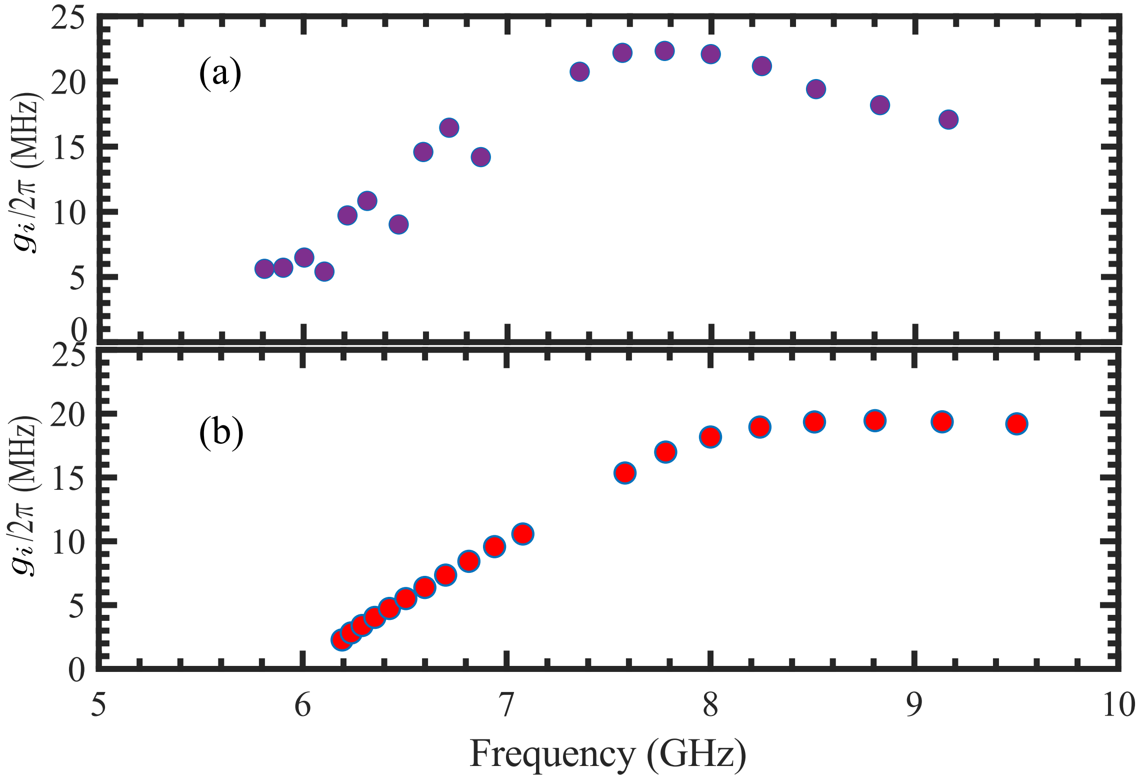

Figure 44: (a) Extracted coupling strength between qubit and each metamaterial mode vs. frequency. (b) Simulated coupling strengths vs. frequency using AWR Microwave Office and circuit model approach described in text. Figure taken from Ref. [97].

in Fig. 42. We can fit the positions of these various splittings to the conventional transmon flux-modulation dependence [Eq. (2.10)] while varying the maximum Josephson energy E_{J0} to obtain the black dashed curve drawn on Fig. 42. The extracted value for E_{J0} is consistent with the fabricated junction parameters.

For each of the modes that the qubit crosses, we can easily see that the splitting is larger than the linewidth of the particular mode, which corresponds to the strong coupling regime of cQED [99]. Since the splittings are smaller than the intermode spacings over the range of our measurements, we can make an approximation and treat each mode individually for extracting the coupling strength g_i for the qubit to each of the metamaterial modes. We first extract the peak frequency as a function of flux for both branches of the splitting. We then fit the solutions of the Hamiltonian for one cavity mode coupled to a transmon with g_i as a free parameter. The bare cavity frequency is fixed to the peak frequency of the mode when measured at high power. For the transmon, first we set E_C based on Q3D simulations. Then, we set the maximum E_{J0} so that the calculated maximum frequency of the transmon matches with the measured frequency (9.25 GHz). In this way, we fit each vacuum Rabi splitting to the Hamiltonian for one resonator mode coupled to a transmon, and thus extract g_i for each mode.

Further details on this fitting, including a discussion of the validity of treating each mode separately, are included in Section 7.2. Fig. 44(a) shows a plot of the extracted g_i values to each mode. Initially $g_i/2\pi$ increases with frequency above ω_{IR} up to a maximum of 22 MHz for the mode near 7.8 GHz; this is followed by a gradual decrease in g_i up to the maximum qubit transition frequency. This non-monotonic variation of g_i with frequency is due to the standing-wave structure in the RHTL portion of our hybrid metamaterial resonator. This is also similar to the variation of Q_{total} with frequency, suggesting corelation between Q_{total} and g_i. We study this non-monotonic behaviour of g_i with frequency in more detail for various lengths of the RHTL section in Section 7.1. In the region around 7.5 GHz, where the modes are relatively close together and the g_i values are near the maximum, the upper branch of the splitting for one mode comes close to touching the lower branch of the splitting for the next higher mode (Fig. 43). Nonetheless, even the maximum g_i remains smaller than the minimum mode spacing, thus, the system is not quite in the multimode strong coupling regime, where the qubit would be able to couple strongly to multiple modes simultaneously.

For modeling g_i and comparing with the measurements, we use AWR Microwave Office [100]. We can simulate the splittings in the spectrum semi-classically by approximating the qubit as a tunable LC oscillator coupled to a hybrid metamaterial resonator with the parameters of our device. Details are discussed in Appendix 7.3. The simulated g_i frequency dependence plotted in Fig. 44(b) is in reasonable agreement with our measured coupling strengths, although the decrease in g_i for the highest qubit frequencies is not quite as strong in the simulations.

Table 3: Qubit and readout resonator parameters.

Label	Description	Value	Method of Determination
f_{01}^{max}	Maximum qubit frequency	9.25 GHz	Qubit spectroscopy of the f_{01} transition at the flux-insensitive sweetspot
η	Qubit anharmonicity	340 MHz	Qubit spectrosopy of f_{01} and $f_{02}/2$
$g_R/2\pi$	Qubit-readout resonator coupling strength	65 MHz	Measurement of resonator transmission S_{21} vs. flux
$\omega_R/2\pi$	Fundamental frequency of readout resonator	7.07 GHz	Measurement of resonator transmission S_{21}
Q	Total quality factor of readout resonator	15,463	Measurement of resonator transmission S_{21}

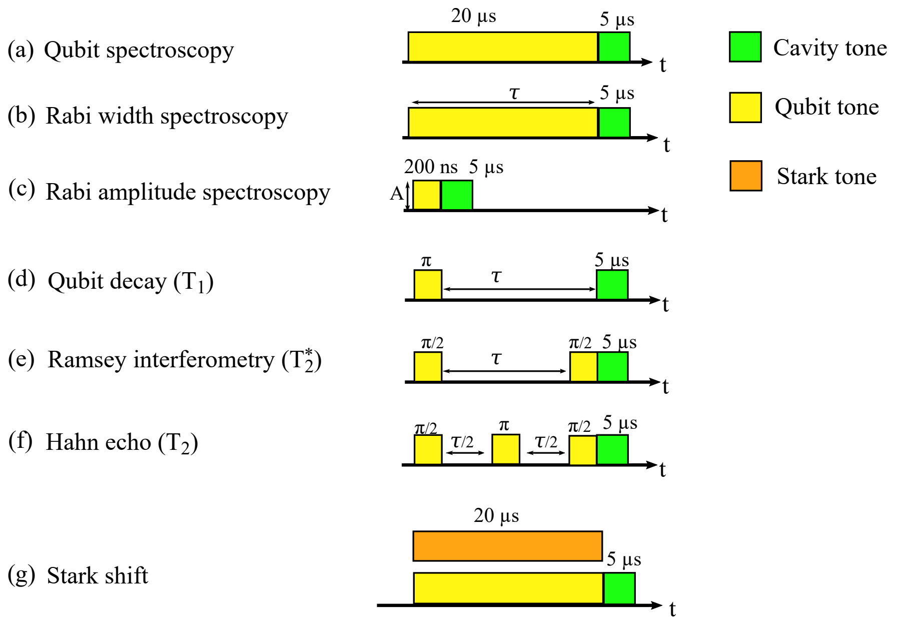
(a) Qubit spectroscopy
20 μs
5 μs
t
(b) Rabi width spectroscopy
τ
5 μs
t
(c) Rabi amplitude spectroscopy
200 ns
5 μs
A
t
(d) Qubit decay (T$_1$)
π
τ
5 μs
t
(e) Ramsey interferometry (T$_2^*$)
π/2
τ
π/2
5 μs
t
(f) Hahn echo (T$_2$)
π/2
τ/2
π
τ/2
π/2
5 μs
t
(g) Stark shift
20 μs
5 μs
t
Cavity tone
Qubit tone
Stark tone

Figure 45: Pulse sequences used for different qubit characterization experiments.

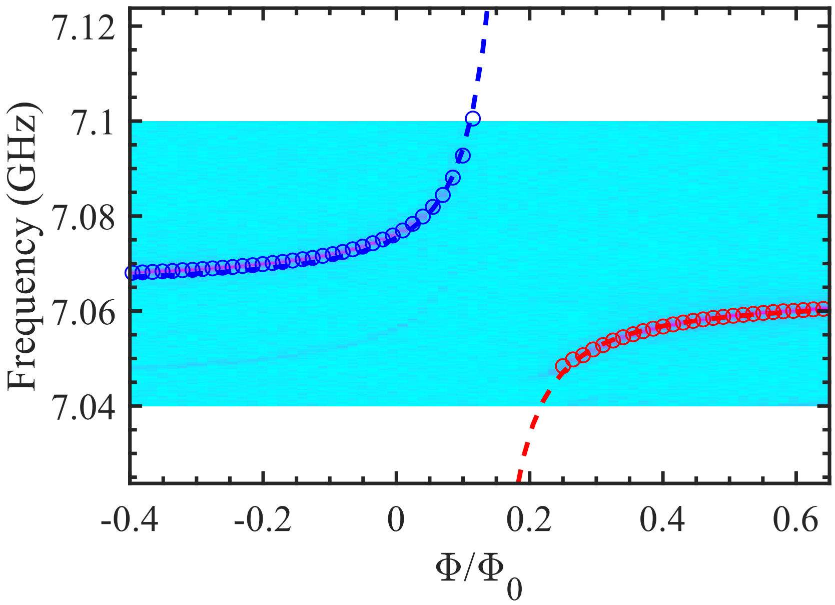

Figure 46: Density plot of magnitude of transmission through readout resonator vs. qubit flux bias. Red (blue) circle are the extracted resonance frequencies extracted from Lorentzian fit of 1D vertical slices of the density plot. Red and blue dashed lines are the eigensolutions of the Hamiltonian of a qubit coupled to one mode of a resonator. The faint blue feature shows up due to the leakage of lower sideband from the mixer used for heterodyne detection.

6.4 Dispersive readout of the qubit

In addition to probing the interactions of the qubit and metamaterial modes through direct measurements of the metamaterial resonator, we are also able to read out the qubit with the separate readout resonator. First, by monitoring the transmission between ports R_{in} and R_{out} and changing the qubit flux bias, we see a vacuum rabi splittng (Fig. 46). As explained in the previous section, by fitting the eigensolutions of the Hamiltonian of a qubit coupled to one mode of a resonator to the peak frequencies from the measurement, we extract the coupling strength between the qubit and the readout resonator. Table 3 lists the extracted coupling strength and other important parameters for the qubit and readout resonator. We perform conventional dispersive measurement of the qubit state, as described in Chapter 2, by measuring the change in transmission of the readout resonator peak while applying a second

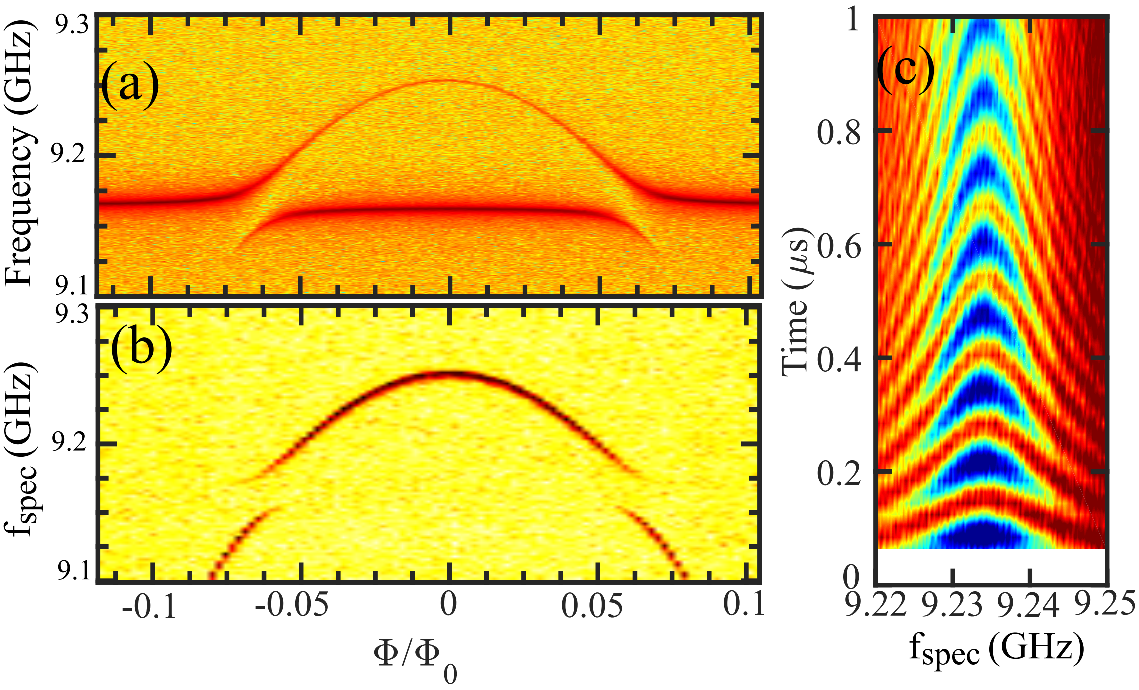

Figure 47: (a) Density plot of magnitude of transmission through metamaterial resonator vs. qubit flux bias in vicinity of upper sweetspot. (b) Spectroscopy of qubit 0-1 transition vs. flux bias near the upper sweetspot measured using readout resonator. (c) Rabi spectroscopy of qubit for flux bias near upper sweet spot, around 9.235 GHz, measured using readout resonator. Figure taken from Ref. [97].

tone simultaneously [Fig. 22(b)] using heterodyne detection.

Figure 47(a) is a plot of the vacuum Rabi splittings for the highest frequency mode that the qubit passes through, observed in the microwave transmission through the metamaterial resonator between ports M_{in} and M_{out} with network analyzer measurements, as in the previous section. In Fig. 47(b), we use ports R_{in} and R_{out} to measure qubit spectroscopy in the same region of flux bias and frequency by sending a 20-μs-long spectroscopy probe pulse at frequency f_{spec}, followed by a 5-μs-long readout resonator pulse to detect the qubit-state-dependent dispersive shift [Fig. 45(a)]. The two curves are quite similar, with comparable splittings when the bare qubit frequency passes through the 9.15 GHz mode.

We can also use the separate readout resonator for conventional coherent manipulation of the qubit state. Figure 47(c) shows a Rabi spectroscopy measurement of the qubit near its maximum transition frequency with a Rabi pulse of variable duration and frequency driven to the readout resonator, again followed by a resonator readout pulse [Fig. 45(b)]. Thus, the qubit remains coherent in this frequency region, despite being biased in the middle of the complex resonance spectrum produced by the metamaterial resonator.

6.5 Purcell losses in a multimode enviroment

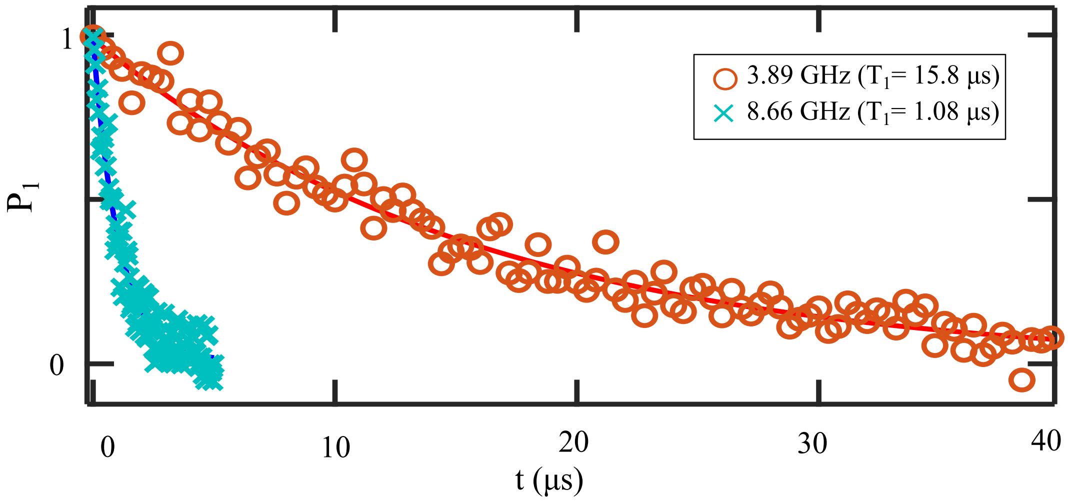

Figure 48: Plots of two example measurements of qubit relaxation measured for a bias point below f_{IR} of the metamaterial and a bias point in between two modes at higher frequencies. Figure taken from Ref. [97].

A π-pulse tuned up from rabi measurement allows us to excite the qubit and characterize its lifetime as it relaxes back to the ground state [Fig. 45(d)]. Figure 48 show the plot of two qubit relaxation measured for a bias point below f_{IR} of the metamaterial and a bias point in between two modes at higher frequencies. By stepping through the qubit flux bias and tuning up a π-pulse at each point, we are able to map out the qubit $T_1(f)$ in the structured environment of our hybrid metamaterial resonator [Fig. 49(a)]. With the qubit biased below $\omega_{IR}/2\pi$, the qubit has a reasonably long lifetime, with T_1 ranging between $10 - 19\,\mu$s, with a gradual decrease for larger

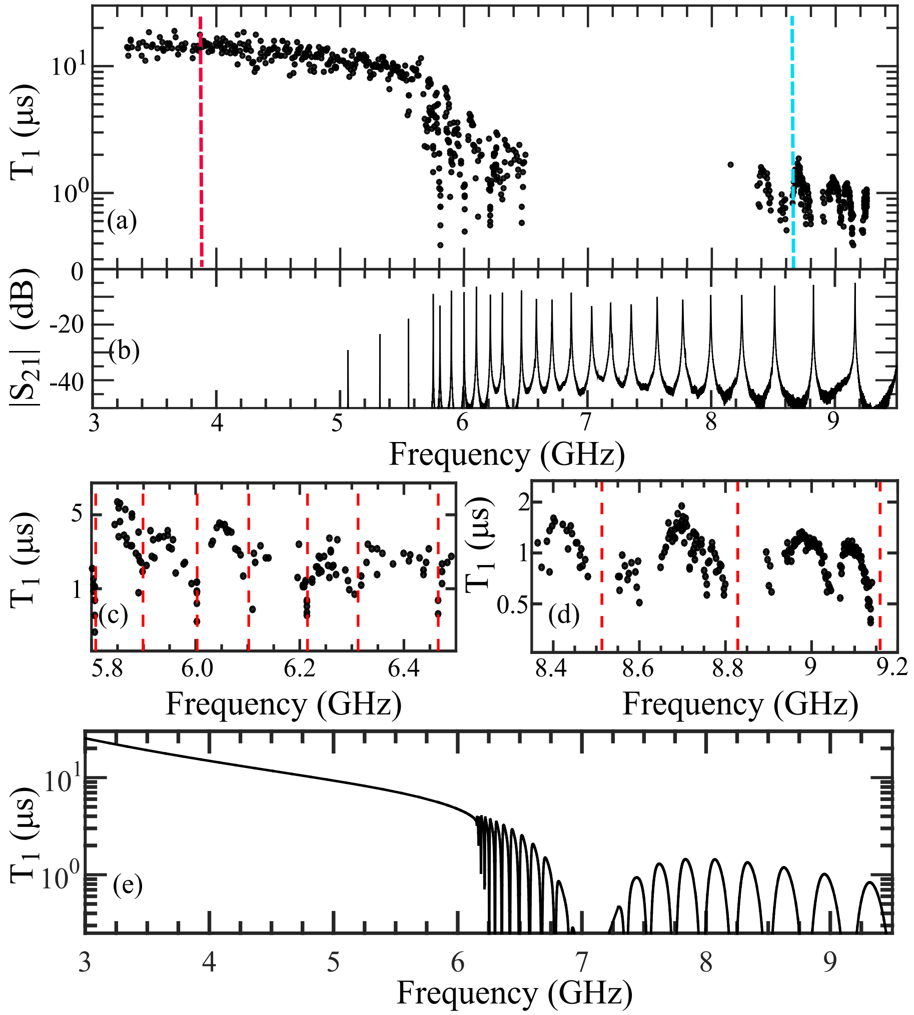

Figure 49: (a) T_1 vs. frequency measured over span of 6.5 GHz. Vertical dashed lines indicate the loaction of the two T_1 decay curves shown in Fig. 48. (b) Transmission spectrum of metamaterial resonator for comparison with structure in $T_1(f)$ plot. (c, d) zoomed-in $T_1(f)$ plots of data from (a) with red vertical dashed lines indicating location of metamaterial resonator modes. (e) Calculated $T_1(f)$ from multi-mode Purcell loss simulation of qubit coupled to metamaterial resonator. Figure adapted from Ref. [97].

frequencies. For frequencies near $\omega_{IR}/2\pi$ and slightly below 6 GHz, T_1 begins to drop significantly, although notably the lowest three metamaterial modes, which are particularly high Q and low transmission, do not strongly influence T_1 [Fig. 49(b)].

Beyond the fourth lowest mode, $T_1(f)$ is characterized by a series of sharp dips to sub-μs levels when the bare qubit frequency matches the various metamaterial resonances; there is a partial recovery of T_1 in between the modes [Fig. 49(c, d)]. The gap in Fig. 49(a) around 7-8 GHz is a result of the strong coupling to the readout resonator, which makes it difficult to address the qubit directly.

The complex frequency dependence of the qubit lifetime that we observe is characteristic of Purcell loss for a qubit coupled to a series of lossy resonant modes [101]. We note that the quality factors of the metamaterial modes in our device are entirely dominated by coupling losses to external circuitry. In this case, we chose $C_{cM}^{in/out}$ to be rather large to make it feasible to observe vacuum Rabi splittings in transmission measurements through the metamaterial while tuning the qubit frequency. For future devices, these coupling capacitances could be made significantly smaller if one were focused instead on probing the metamaterial modes via the qubit, rather than by direct transmission through the metamaterial. In this case, the mode quality factors would be significantly higher and the Purcell losses much smaller, particularly when the qubit is tuned in between the modes.

Following the approach outlined in Ref. [101], we model the multi-mode Purcell effect as $T_1^{Purcell}(f) = C/\mathrm{Re}[Y(f)]$, where C is the qubit shunt capacitance and $Y(f)$ is the frequency-dependent complex admittance of the qubit environment. The detailed calculation are given in the next Chapter. The resulting $T_1(f)$ dependence from our model plotted in Fig. 49(e) qualitatively follows our measurements, although we do not quantitatively reproduce the locations of the T_1 dips due to the difficulty of capturing the experimental metamaterial spectrum in our circuit model, particularly near $\omega_{IR}/2\pi$, without accounting for the effects of the staggered inductor configuration and non-ideal grounding of the metamaterial chip, as described in Ref. [39]. Nonetheless, the Purcell modeling provides a route for describing the frequency-dependent lifetime for a qubit coupled to a complex metamaterial, including the relatively long T_1 values that can be attained in the bandgap of the metamaterial spectrum.

6.6 Qubit decoherence

We also study the coherence of the transmon as a function of flux near the maximum frequency of the qubit. Figure 50(a) shows T_2^* and T_2 as function of flux measured

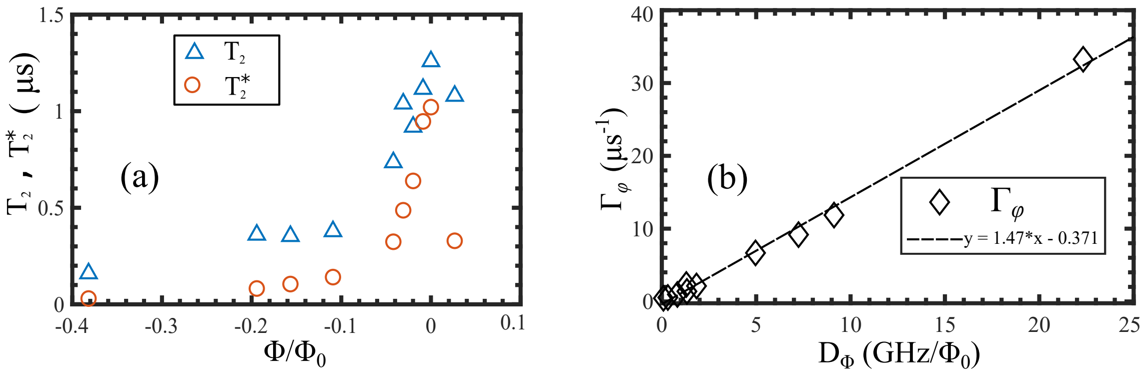

Figure 50: (a) Qubit T_2 and T_2^* measured as function of flux. (b) Qubit dephasing measured as a function of D_Φ.

using Ramsey interferometry [Fig. 45(e)] and Hahn Echo techinique [Fig. 45(f)]. We observe that T_2^* and T_2 are higher near $\Phi/\Phi_0 = 0$, where the qubit's frequency gradient as a function of flux, $D_\Phi = |\partial f_{01}/\partial\Phi| = 0$. Thus, this is a bias point where the qubit is first-order insensitive to flux noise.

From the qubit T_1 and T_2^* we can calculate pure dephasing $\Gamma_\phi = 1/T_2^* - 1/2T_1$ as a function of flux. To assess the effect of flux noise on pure dephasing, we observe how the pure dephasing relates to qubit's frequency gradient as a function of flux D_Φ. Figure 50(b) shows the plot of Γ_ϕ vs D_Φ. Following the approach in Ref. [48], we apply a linear fit of form $mD_\Phi + b$ to the plot of Γ_ϕ as function of D_Φ and compare it to $\Gamma_\phi = 2\pi\sqrt{A_\Phi|\ln(2\pi f_{IR}t)|}D_\Phi$. Here, the flux noise spectrum is $S_\Phi(f) = A_\Phi/|f|$, f_{IR} is the infrared cutoff frequency, which we take to be 1 Hz and t is on the order of $1/\Gamma_\phi$, which we take to be 1 μs in our calculations. We find a flux noise level $A_\Phi^{1/2} \sim 6.7\ \mu\Phi_0$, which is somewhat high, but within the range of other flux noise measurements from transmons [48], flux qubits [102, 103], phase qubits [104], and dc SQUIDs [105].

6.7 Stark shift measurements

With the ability to perform dispersive measurements of the qubit with the readout resonator (using $R_{in/out}$) while simultaneously driving a separate microwave signal to the hybrid metamaterial resonator (using $M_{in/out}$), we are able to observe the ac Stark shift of the qubit 0-1 transition [52] for different average numbers of photons

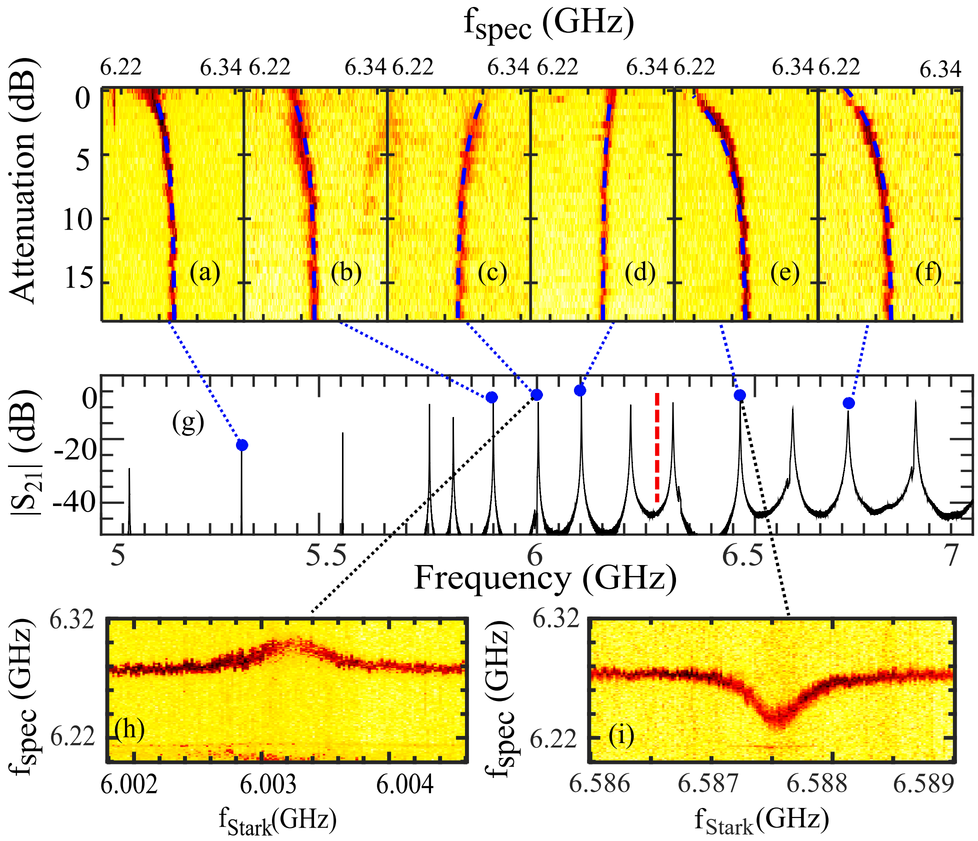

Figure 51: (a-f) Stark shifts of qubit transition through driving of 6 different metamaterial modes at a range of microwave powers for a flux bias corresponding to the unshifted qubit transition at 6.275 GHz; Stark shift theoretical curves shown by blue dashed lines. For the 6 plots, 0 dB attenuation corresponds to a power at the chip of (a) -86 dBm, (b) -126 dBm, (c) -128 dBm, (d) -123 dBm, (e) -121 dBm, and (f) -113 dBm. (g) $|S_{21}(f)|$ measured through metamaterial to indicate the 6 modes driven in (a-f) (blue dots and dotted lines) and the bias point of the qubit (red dashed line). Plots of qubit spectroscopy frequency vs. Stark drive frequency for fixed power for (h) mode near 6.003 GHz at -129 dBm, (i) mode near 6.588 GHz at -122 dBm; metamaterial mode near 6.22 GHz visible as a faint, sharp line near bottom of plots. Figure taken from Ref. [97].

in each of the metamaterial modes [Fig. 45(g)]. With the qubit biased at 6.275 GHz, as indicated in Fig. 51(g), we measure the qubit transition in spectroscopy while driving one of the six different metamaterial modes and scanning over 18 dB of power for the Stark drive to generate the plots in Fig. 51(a-f). Additionally, for two of these metamaterial modes, we again perform qubit spectroscopy while scanning the frequency of the Stark drive for fixed power [Fig. 51(h,i)].

The observed shift of the qubit transition increases in magnitude with the power of the Stark drive when the frequency is resonant with a metamaterial mode, as with a qubit coupled to a single resonator [52]. Moreover, if the metamaterial mode being driven falls between the qubit 0-1 and 1-2 transition frequencies, the straddling regime identified in Ref. [44], we observe a change in the sign of the Stark shift. The observed Stark shifts of the qubit with microwave driving of various metamaterial modes can be explained well by a model of a transmon qubit coupled dispersively to a single mode resonator, corresponding to the particular mode being driven (mode i), according to

$$H/\hbar = \omega_i \hat{\mathbb{M}}_i + \left(\frac{\omega_q}{2} + \chi \hat{\mathbb{M}}_i\right)\sigma_z, \tag{6.2}$$

where ω_i is the frequency of the relevant (single) metamaterial mode, $\hat{\mathbb{M}}_i = \sum_{m_i} m_i |m_i\rangle\langle m_i|$ is the number operator for mode i, ω_q is the qubit 0-1 transition frequency, $\chi = g_i^2\eta/(\delta_i\eta - \delta_i^2)$ is the qubit frequency shift per photon, $\delta_i = \omega_q - \omega_i$ is the detuning between the qubit and the metamaterial mode, and η is the anharmonicity of the transmon, defined as the difference between the 1-2 and 0-1 transition frequencies.

The Stark tone at frequency ω_d drives the resonator to a coherent steady state with average photon number

$$\bar{n}_i = \langle \hat{\mathbb{M}}_i \rangle = \frac{\Omega_i^2}{(\omega_i - \omega_d)^2 + \frac{\kappa_i^2}{4}}. \tag{6.3}$$

Here, Ω_i is the effective drive amplitude for mode i and κ_i is the mode decay rate from separate measurements of the linewidth of each metamaterial mode (Fig. 41). Thus, $\bar{n}_i$ is proportional to the power delivered to the mode. Making a semiclassical approximation to the Hamiltonian in Eq. (6.2), one finds the qubit Stark shift to be given by $\chi\bar{n}_i$. A single-parameter linear fit between the power measured at the chip for each mode frequency from a separate baseline cooldown and the observed Stark shift for each driven mode gives a map from the input drive power for each mode and the actual power delivered to the mode, Ω_i^2. This fit parameter then allows us to compute the theory curves included in Fig. 52.

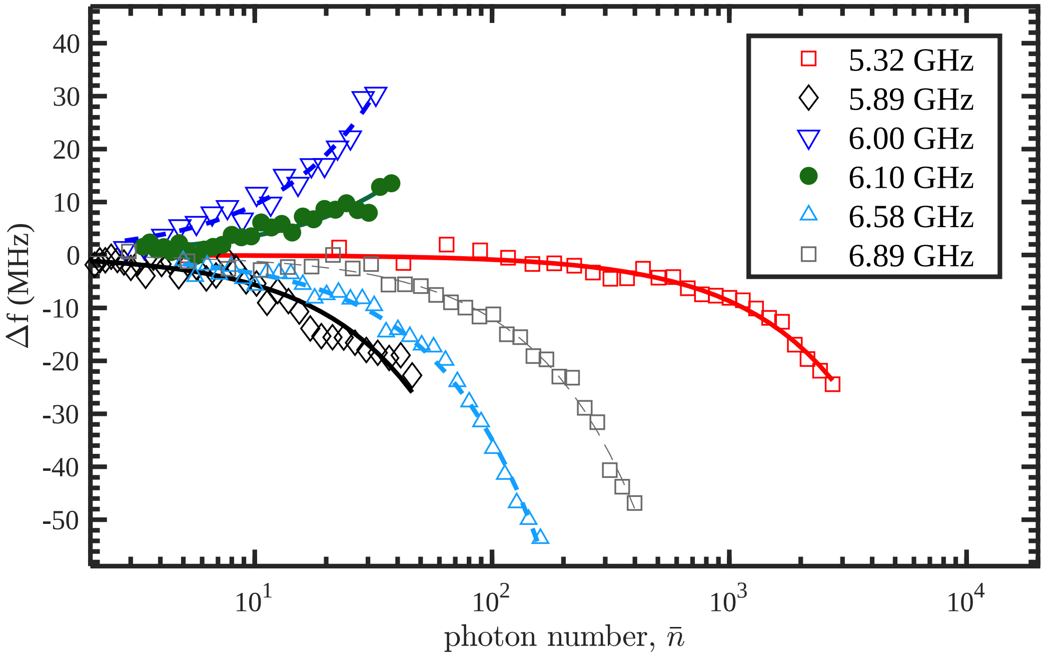

Figure 52: Extracted Stark shifts in qubit transtion frequency from Fig. 51(a-f) plotted vs. mean photon number for each of the 6 metamaterial modes, as described in text. Figure taken from Ref. [97].

Chapter 7

Numerical Simulations

In this chapter, I present several simulations of metamaterial resonators and qubits and their comparison with measurements, whenever applicable. We employ two powerful simulations tools, AWR Microwave Office [100] and Sonnet [106], to study the properties of the metamaterial resonator. AWR uses a lumped-element approach for simulations, so it is a fast way to model the metamaterial resonator. We also use scripts [107] to automate the tuning of various circuit parameters, run the simulation, and record the results in data files for analysis. However, AWR has limitations, as it cannot capture the effects related to the electromagnetic (EM) field distribution, such as simulation of geometrical effects of staggered inductors, non-ideal grounding, and the short-wavelength effects that deviate from ideal lumped-element behavior.

Sonnet, on the other hand, uses finite-element method to solve the Maxwell's EM field equations to simulate the actual sample layout with high accuracy but requires much longer time and massive computing resources. We take advantage of a Sonnet software cluster at Syracuse University with 10 nodes, each with 64 GB of memory. Still, it takes from several days to a couple of weeks to simulate the full spectrum of only the LHTL section of our device. The challenge also comes from the fact that our devices consist of a large array of capacitors made from interdigited fingers with narrow width/gaps and inductors made from narrow width meander lines.

7.1 Numerical simulations of mode structure of metamaterials

Here, I show the simulated spectra from AWR and Sonnet and how they compare with measurements for Device A () and Device B. Figure 53 compares the measured transmission spectrum for the LHRH hybrid metamaterial (Device B) with a circuit simulation of $S_{21}(f)$ using AWR with the parameters in the table 1 and 2. The spectra are reasonably close, with the most significant deviation at the low-frequency end, where the measured device has a softer infrared cutoff due to the staggered inductor configuration.

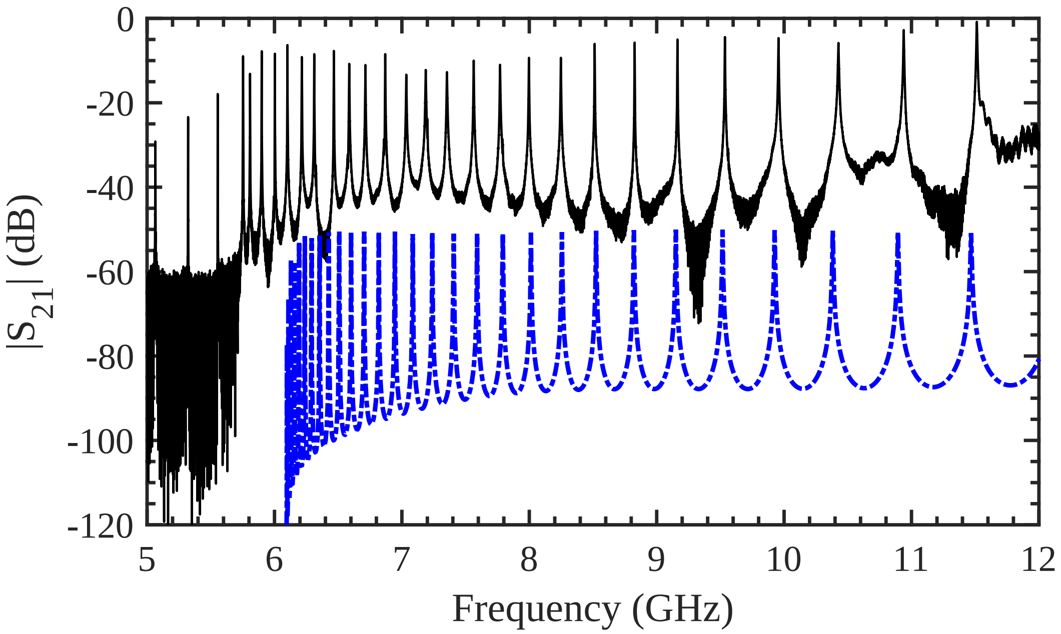

Figure 53: Measured transmission spectrum (black line) for Device B (LHRH hybrid metamaterial with non staggered inductors) compared with spectrum from circuit simulation using AWR (blue dashed line, with -50 dB offset for clarity). Figure adapted from Ref. [97].

7.1.1 Effects of staggered inductor layout

As described in Chapter 4, we chose to use a staggered layout for the inductors in our metamaterial resonators for Device A and Device B, as shown in the device images of Fig. 23 and 20, while Device C had a non-staggred layout of inductors (Fig. 25).

Here, we present summary of Sonnet simulations to examine the effects of the inductor layout configuration on the resonator spectrum [59, 39]. We compare the simulated spectrum from Sonnet with the measured spectrum. Sonnet simulations include only the LHTL section of the hybrid metamaterial resonator (Device B).

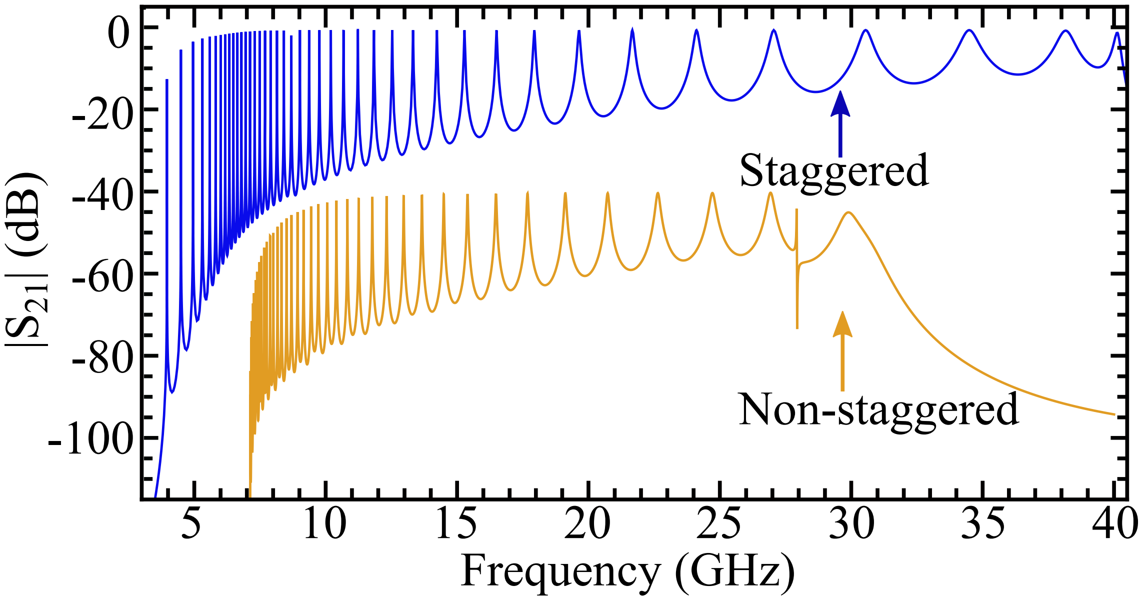

Figure 54: Sonnet simulations of $S_{21}(f)$ for non-staggered (orange, with -40 dB offset for clarity) and staggered (blue) inductor layouts. Figure taken from Ref. [39].

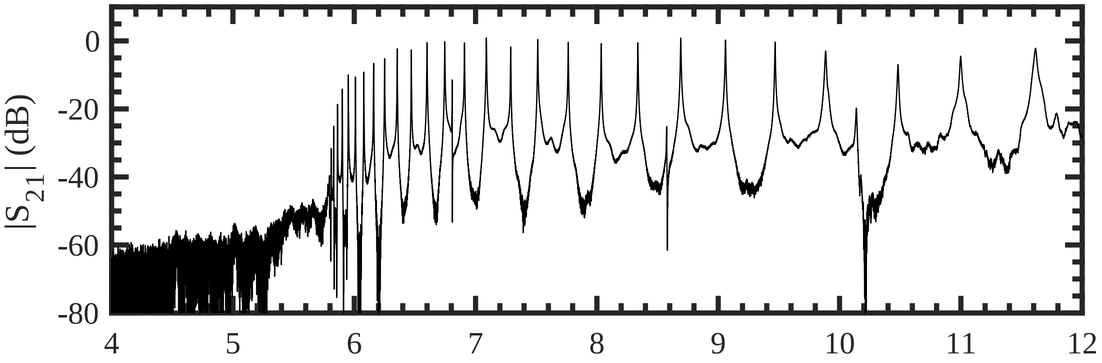

Figure 55: Measurement spectrum of Device C that has all inductors on one side of the capacitors that form the LHTL.

In Fig. 54, we compare the $S_{21}(f)$ spectrum simulated using Sonnet for the original staggered and non-staggered inductor configurations. Although both spectra follow the overall pattern expected for an LHRH resonator, as presented earlier, there are clear differences between the spectra for the two inductor layouts. In the non-staggered configuration, the modes just above $\omega_{IR}/2\pi$ have the highest density. This is in contrast to the staggered inductor spectrum, where the modes reach their highest density for a frequency about 2 GHz above $\omega_{IR}/2\pi$. This discrepancy between the spectra for the two inductor configurations can also be seen in our measurements for Device B (Fig. 39) and Device C (Fig. 55), where the mode frequencies of the non-staggered inductor configuration follow the theoretical dispersion relation closely, while the lowest frequency and highest n modes of the staggered inductor configuration fall below the theoretical curve. Based on the Sonnet simulations, we conclude that the distribution of the currents through the staggered inductors for the shortest wavelength modes causes deviations from ideal lumped-element behavior, leading to reduced resonance frequencies.

7.1.2 Effects of imperfect grounding

In our experimental setups, the ground plane of the chips is connected to the ground plane of our sample holders through a series of short aluminum wirebonds around the perimeter of the chip. Multiple jumper wirebonds are also used across the LHTL and the CPW segments on either end to ensure that the different discontinous sections of ground plane are as close to a uniform equipotential as possible. However, it is a common issue with superconducting thin-film microwave circuits [108], that the nonzero self-inductance of the wirebonds can lead to imperfect grounding over the entire area of the device. Using Sonnet, we have simulated the effects of different grounding conditions to study how this affects the spectrum and coupling quality factor of the metamaterial resonances. The details of simulations setup can be found in Ref. [39].

Figure 56 shows the results of the Sonnet simulations of a 42-cell LHTL resonator for the various grounding configurations. We compare the frequency of the resulting modes (56(a)) and coupling loss (56(b)) for each mode from $n = 24 - 41$. We observe that the mode frequencies and the coupling loss are only influenced significantly for the highest mode numbers.

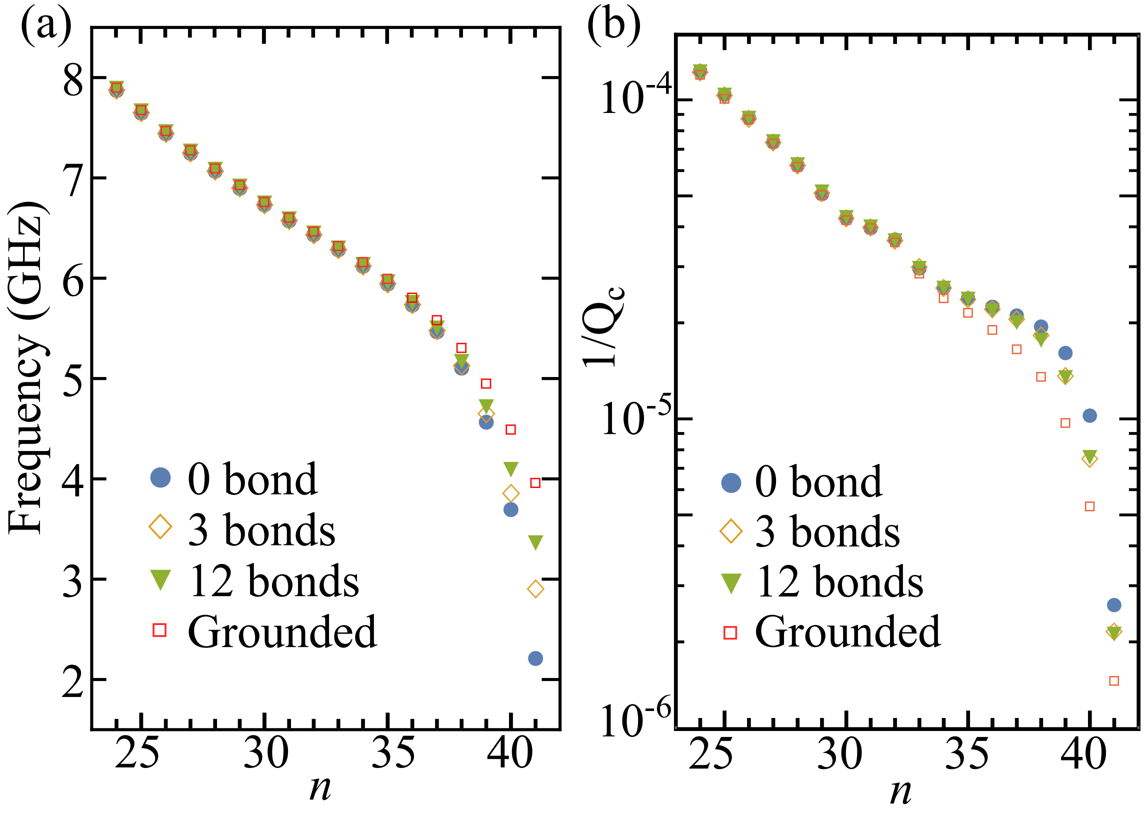

Figure 56: Sonnet simulations for different grounding configurations for a 42-cell LHTL resonator for (a) resonance frequency vs n, (b) coupling loss $1/Q_c$ vs n. Figure taken from Ref. [39].

7.2 Extraction of qubit-metamaterial mode couplings from spectra

We consider a metamaterial resonator as a system of uncoupled quantum harmonic oscillators. When coupled to a qubit, the closed system can be described by the Hamiltonian:

$$\hat{H}/\hbar = \frac{1}{2}\omega_q\hat{\sigma}_z + \sum_m \left[\omega_m \hat{a}_m^\dagger \hat{a}_m + g_m(\hat{\sigma}_+ + \hat{\sigma}_-)(\hat{a}_m^\dagger + \hat{a}_m)\right], \tag{7.1}$$

where ω_q is the qubit frequency, $\hat{\sigma}_z$ is the Pauli pseudo-spin z operator and m represents cavity mode number. $\hat{a}_m^\dagger$ and $\hat{a}_m$ are raising and lowering operators for mode m. $\hat{\sigma}_+$ and $\hat{\sigma}_-$ are raising and lowering operators for the qubit, and g_m is the coupling strength of the qubit to the mode m. Here, we assume the ideal qubit with two energy levels, but in our calculations for extracting coupling strength between a transmon and multiple modes of the resonator, we include higher energy levels, as explained below.

In order to determine the coupling strength g_i between the transmon and mode i of the metamaterial with frequency ω_i, we assume each mode can be represented as an independent harmonic oscillator coupled capacitively to the transmon. We utilize standard circuit quantization [44, 33] to derive the Hamiltonian for the transmon-coupled metamaterial, which, when written in the basis of transmon charge $|n\rangle$ and resonator excitation number $|m_i\rangle$ is given by

$$\begin{aligned}\hat{H} = &\left[\sum_n \left(4E_C(n-n_g)^2|n\rangle\langle n| - \frac{E_J}{2}\left(|n+1\rangle\langle n| + |n\rangle\langle n+1|\right)\right)\right] \otimes \hat{\mathbb{I}}_m + \\ &\sum_i \left(\sum_{m_i} \hat{\mathbb{I}}_n \otimes \hbar\omega_i \left(|m_i\rangle\langle m_i| + \frac{1}{2}\right) + \right. \\ &\left.\sum_{n,m_i} \hbar g_i n|n\rangle\langle n| \otimes \sqrt{m_i+1}(|m_i+1\rangle\langle m_i| + |m_i\rangle\langle m_i+1|) \otimes \hat{\mathbb{I}}_{m_{j\neq i}}\right).\end{aligned} \tag{7.2}$$

Here, $\hat{\mathbb{I}}_m$ is the product of metatmaterial mode identity operators, $\hat{\mathbb{I}}_{m_i}$ is the identity operator for metamaterial mode i, $\hat{\mathbb{I}}_n$ is the charge basis identity operator, $E_C = e^2/2C_\Sigma$ where $(C_\Sigma = C_Q + 2C_J + C_{QR} + C_{QM})$ is the transmon charging energy, n_g is the transmon polarization charge, and E_J is the flux-tunable Josephson energy, which, for the case of symmetric junctions, is given by

$$E_J = E_{J0}\left|\cos\left(\pi\frac{\Phi}{\Phi_0}\right)\right|, \tag{7.3}$$

where E_{J0} is the maximum Josephson energy, Φ is the external flux applied to the transmon, and $\Phi_0 \equiv h/2e$ is the flux quantum. For our device, $E_C/h = 0.31$ GHz and $E_{J0}/h = 37$ GHz. Note that due to the large ratio of E_J/E_C , the dependence on n_g for the qubit 0-1 transition is ~ 2 kHz, which is negligible compared to the qubit 0-1 transition , between 3-9.25 GHz for the measurements reported. Junction asymmetry is assumed to be negligible due to the uniformity achieved in the Josephson junction fabrication. So, we can ignore the effect of junction asymmetry and the dependence on n_g in the model for the fitting routine discussed here.

Next, we implement a numerical minimization routine in Matlab to fit the lowest two eigenvalues of the model Hamiltonian to the frequency response of metamaterial transmission measurements versus flux Φ (Fig. 42) in the vicinity of each vacuum Rabi splitting. For each fit, we truncate the transmon Hilbert space to 21 charge states and each resonator mode to 4 number states. In order to reduce the convergence time of the fit to an acceptable duration, for each vacuum-Rabi splitting i, we include just a single metamaterial mode in the model (i.e., mode i with frequency ω_i). Note that in each fit, g_i is the only free parameter, with all other parameters in the Hamiltonian determined via independent measurements.

In several trial cases, to estimate the error that results from neglecting the full spectrum of metamaterial modes, we performed fits where we solved the Hamiltonian including two nearest neighbor modes, rather than only one mode. We found the extracted value of each g_i in these cases to be within 5% of the value from the fits with only a single metamaterial mode. This is compatible with the coupling regime for our present device, where g_i remains less than the intermode spacing $\Delta\omega_i$ between modes i and $i+1$ over the range of our measurements.

7.3 Calculation of qubit-metamaterial mode couplings

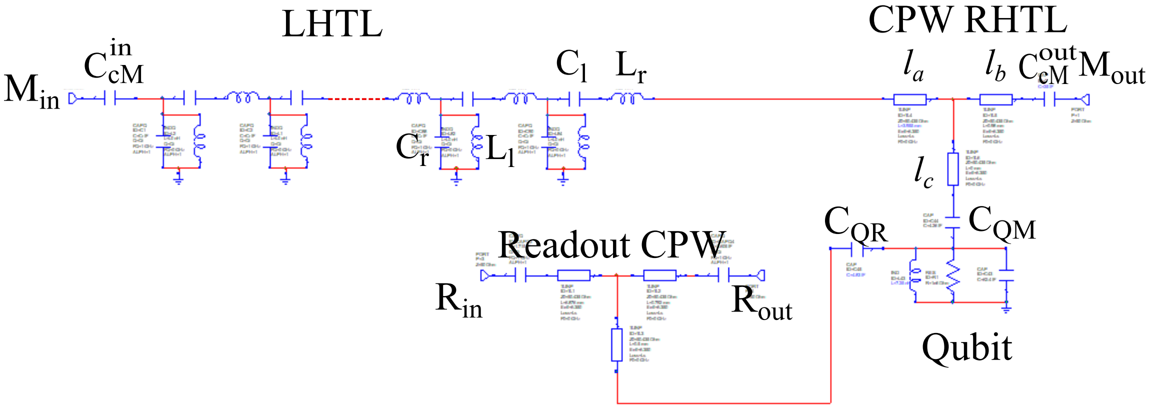

Figure 57: AWR circuit model of Device B.

For modeling g_i, the coupling between metamaterial mode i and the transmon qubit, we use a semi-classical approach involving AWR simultions. As shown in Fig. 57, the LHTL section of the metamaterial resonator consists of 42 unit cells of series

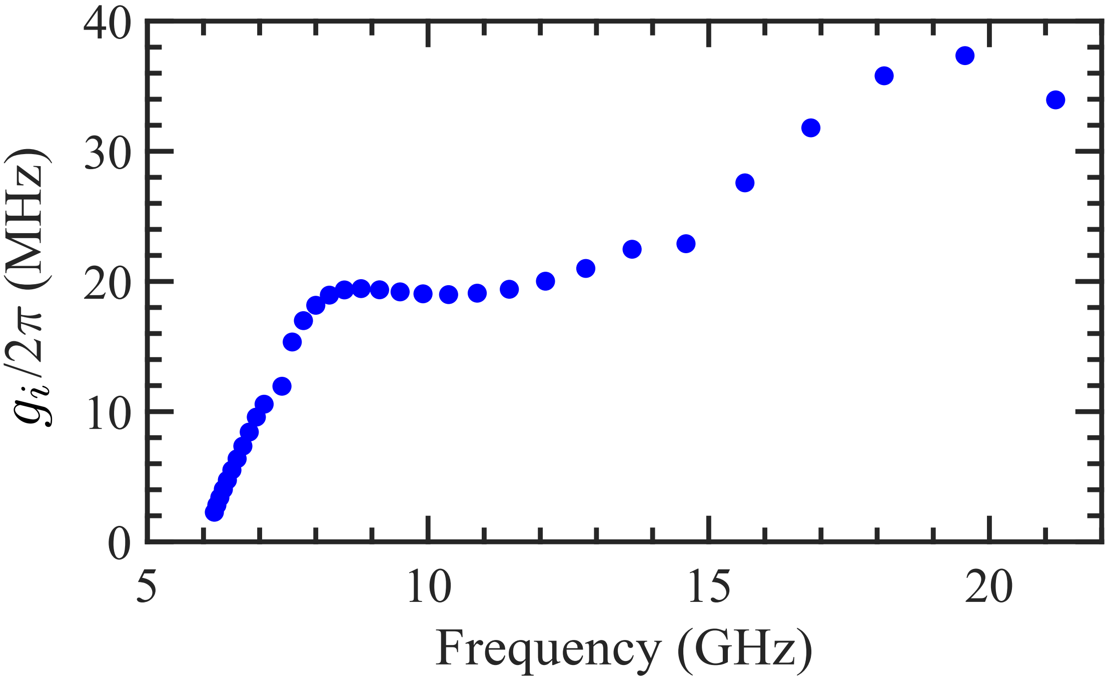

Figure 58: Simulated g_i from AWR/circuit model extended out to higher frequency for a hypothetical qubit with higher upper sweetspot. The slight deviation at 7.5 GHz and 15 GHz is due to the mode frequency approaching fundamental and first harmonic modes of readout resonator. Figure adapted from Ref. [97].

capacitors C_l and inductors L_l to ground, as in the measured device. In addition, we include parasitic effects in each cell consisting of a small lumped-element inductor L_r in series with C_l that accounts for the stray inductance of the interdigitated capacitor; a small lumped-element capacitor C_r in parallel with L_l accounts for the stray capacitance from the meander-line inductors. The values for these circuit parameters used in the simulations were chosen based on our earlier modeling of LHTL resonators [39], including simulations with Ansys Q3D [109] and Sonnet [106]. We set the loss in the capacitors in AWR to correspond to an internal quality factor of 10^5 [39].

For the AWR modeling, we treat the transmon as a tunable, lumped-element LC oscillator, with L being flux-tunable and the L and C values determined by the measured device. The coupling between the qubit and the RHTL CPW portion of the metamaterial resonator is set by the coupling capacitor C_{QM}, as listed in Table 3. The simulation also includes the separate CPW readout resonator (Fig. 57), using parameters corresponding to the measured device, with coupling capacitor C_{QR} to the qubit.

To extract the value of g_i, we simulate S_{21} transmission measurements through the metamaterial (i.e., between M_{in} and M_{out} in Fig. 57). We adjust L for the qubit to simulate flux tuning and bring the qubit near resonance with mode i. We then scan the qubit L to sweep it through resonance with mode i, and thus generate a simulated vacuum Rabi splitting. We thus determine the coupling strength to mode i from the minimum spacing in the avoided-level crossing with the qubit, corresponding to twice the simulated coupling strength, $2g_i$. With this technique, we can simulate the frequency dependence of g_i vs. mode frequency ω_i, as in Fig. 44.

Unlike our measured device, where the upper sweet spot of the qubit is 9.25 GHz, the circuit simulations allow us to explore an artificial qubit with a much higher maximum frequency, so that we can study g_i further along the metamaterial resonance spectrum. The resulting plot of g_i vs. frequency (Fig. 58) exhibits multiple dips, where the reduction that we observe in our experiment around $\sim 8-9\,\mathrm{GHz}$ is the first dip, due to the standing-wave structure in the RHTL portion. As the standing-wave pattern in the RHTL portion changes, the voltage level coupled to the qubit through C_{QM}, and hence the coupling strength g_i, can change. This effect will be explored in more detail in next section. The slight deviations in g_i near 7.5 GHz and 15 GHz are due to metamaterial modes being very close to the readout resonator frequency or its harmonics.

7.4 Approaches for increasing qubit-metamaterial mode couplings

Although on our present device the coupling strength between the qubit and each metamaterial mode was always less than the spacing between modes $\Delta\omega_i$, in this section we consider the parameters for a hypothetical qubit-metamaterial device that could reach superstrong coupling [32], where $g_i/\Delta\omega_i > 1$. In this regime, the qubit can be strongly coupled to multiple modes simultaneously. In this section, we consider various modifications to the metamaterial and qubit, some of which enhance g_i and others that decrease $\Delta\omega_i$.

One approach for increasing g_i involves increasing C_{QM}, as $g_i \propto C_{QM}/C_{\Sigma}^{1/2}$ [44].

Table 4: Modified metamaterial parameters for hypothetical device with enhanced coupling strength used in AWR simulation.

Label	Description	Value for measured chip	New value
N_l	Number of LHTL unit cells	42	82
Z_M	Metamaterial impedance	50 Ω	200 Ω
N_r	Number of RHTL unit cells	N/A	20
L_{RH}	RHTL unit cell inductance	N/A	0.35 nH
C_{RH}	RHTL unit cell inductance	N/A	9.5 fF
C_{QM}	Qubit-metametarial coupling capacitance	4.3 fF	50 fF
C_Q	Qubit capacitance	48 fF	50 fF

We note that large coupling strengths between a qubit and resonator can also be achieved through inductive coupling [30], but for now, we will restrict our design considerations to capacitive coupling. Another route for enhancing g_i involves increasing the impedance of the metamaterial resonator. For the LHTL portion, this is straightforward to achieve by adjusting the values of L_l and C_l. However, making a significant increase in the impedance for the RHTL portion is difficult with a CPW configuration. For example, a CPW impedance of 120 Ω requires a center conductor width of 500 nm and a 10-μm gap to the ground plane, which can be challenging to fabricate. As an alternative, we consider using a lumped-element implementation for the RHTL portion, which allows for larger impedances by choosing the inductor and capacitor values appropriately. We note that a lumped-element RHTL is a departure from our present design, but this should not introduce any complications since our device layout already includes chains of similar lumped-element inductors and capacitors for the LHTL and these would all get fabricated at the same time. In addition to increasing the coupling capacitance and resonator impedance, the total length of the RHTL portion and the positon where the qubit is coupled also impacts the coupling strength through the variation of the standing-wave amplitude at the location of the qubit (as shown in Figs. 59 and 60). The length of the RHTL portion and the

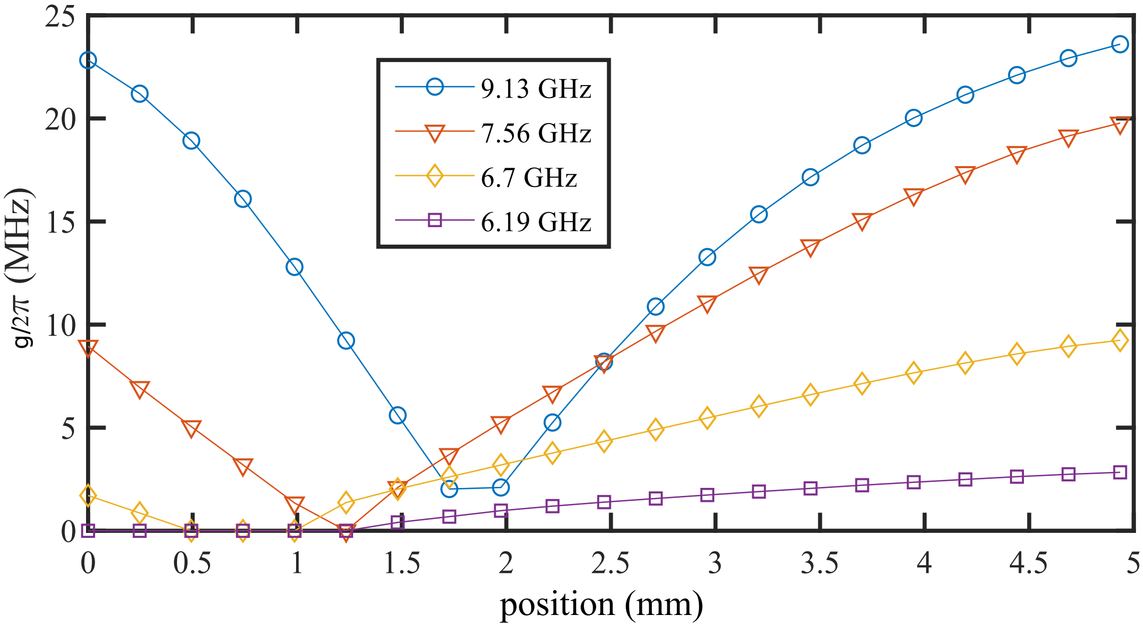

Figure 59: Coupling strength of four metamaterial modes to the qubit as function of the position on the RHTL where the qubit is coupled. The total length of RHTL section is 6 mm. The coupling strength reduces to zero at different locations for different modes due to variations in the position where the standing-wave amplitude for the modes corresponds to a node.

positon where the qubit is coupled should be chosen so that the maximum coupling is near the infra red frequency region where the modes are spaced closely. Besides increasing g_i, we can also decrease $\Delta\omega_i$ by adding more unit cells to the LHTL or by using a superlattice arrangement for the LHTL [110], both of which increase the mode density since the number of modes between the IR and UV cutoff frequencies corresponds to the number of unit cells. Table 4 summarizes the various parameters for our hypothetical qubit-metamaterial device capable of achieving $g_i/\Delta\omega_i > 1$.

With the parameters of our hypothetical device described above, we characterize the coupling by simulating the microwave transmission through the metamaterial while tuning the qubit frequency. In order to build intuition about the splittings in the spectrum for the superstrong coupling regime, we also study the system Hamiltonian for various values of g_i. Because the size of the Hilbert space grows exponentially with the number of modes, in order to keep the numerical simulation tractable, we

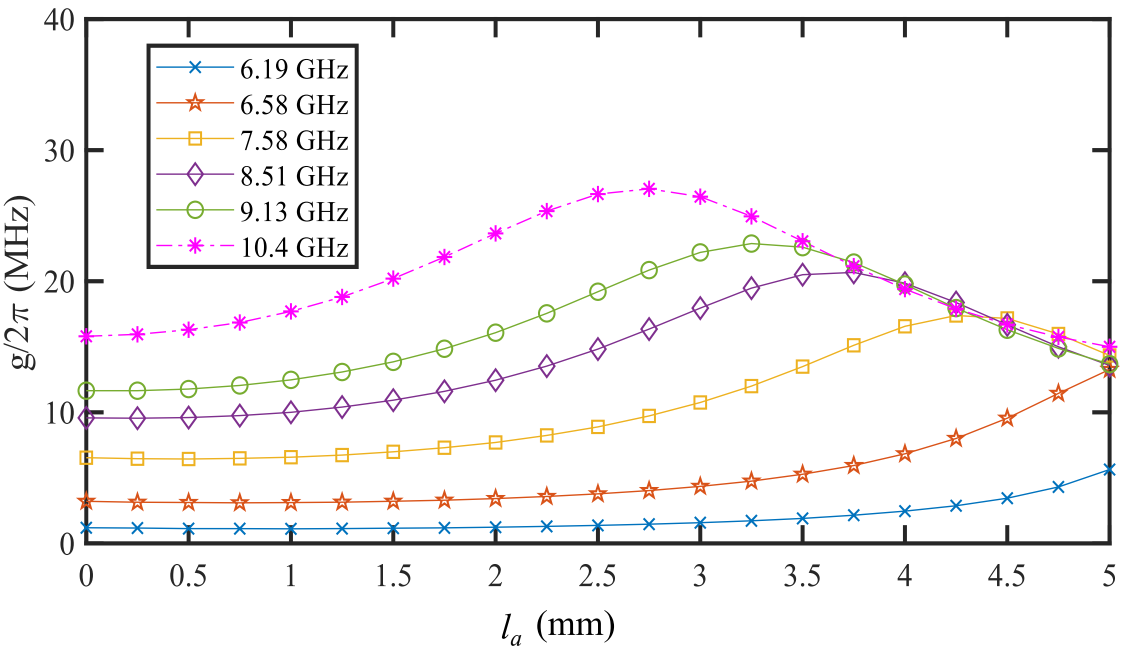

Figure 60: Coupling strength of six metamaterial modes to the qubit as function of the length of the RHTL section. The total length of RHTL section is 1 mm longer than l_a since it also includes the section from the location where the qubit is coupled to the output coupling capacitor C_{cM}^{out}. The maximum of coupling strength occurs at different lengths of RHTL for different modes due to variation of standing-wave amplitude for the modes.

restrict the system to four modes spaced by 100 MHz for the simulations shown in Fig. 61. For small g_i, such as the 16 MHz and 32 MHz plots, the solutions exhibit conventional vacuum Rabi splittings as the qubit passes through each of the individual metamaterial modes. For larger g_i, the splitting from one mode begins to merge with the splitting from the next mode, and by the point with 164 MHz couplings, the splittings become difficult to distinguish from the strongly shifted modes.

Figure 62 contains a 500-MHz segment of the simulated transmission spectrum for our hypothetical device with the parameters from Table 4 as a function of the qubit flux. We then run a numerical solution to the system Hamiltonian with four modes, corresponding to the bare mode frequencies in the frequency window of Fig. 62, and adjust the coupling strengths g_i in the Hamiltonian for these four modes to match the

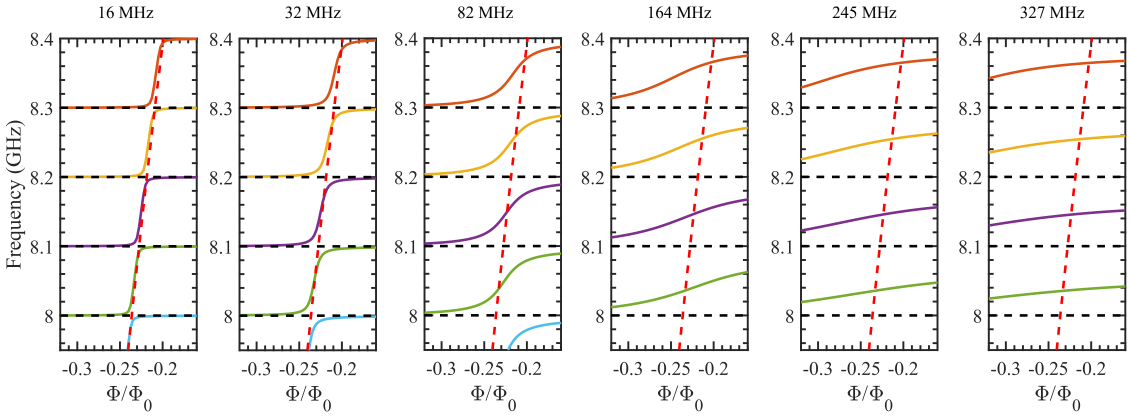

Figure 61: Numerical solutions for a transmon coupled to four modes with 100 MHz intermode spacing; bare mode frequencies are indicated by horizontal dashed lines. Nearly vertical red dashed line corresponds to bare transmon frequency. Label at the top of each plot indicates the coupling strength $g_i/2\pi$ between each of the four modes and the transmon. Figure adapted from from Ref. [97].

features in the AWR simulation. The blue dashed lines follow the Hamiltonian solutions and correspond to coupling strengths of between 178-220 MHz. Thus, $g_i/\Delta\omega_i$ ranges between 1.28 and 1.84, so that the hypothetical device with experimentally feasible parameters is capable of reaching the superstrong multimode coupling regime. In the next chapter, I will discuss our initial experimental plans for taking these next steps towards the superstrong coupling regime.

7.5 Calculation of Purcell loss

The complex frequency dependence of the qubit lifetime that we observe in Fig. 49 can be described by a combination of Purcell loss for a qubit coupled to a series of lossy resonant modes [101] and dielectric loss with a frequency-independent loss tangent that is typically observed in frequency-tunable transmons [111, 48]:

$$\frac{1}{T_1} = \frac{1}{T_1^{Purcell}} + \frac{1}{T_1^{non-Purcell}}, \tag{7.4}$$

where $T_1^{non-Purcell}(\omega) = A/\omega$ for some constant A. This, of course, is a simplification, as even simple real devices with a single qubit coupled to a single resonator mode can

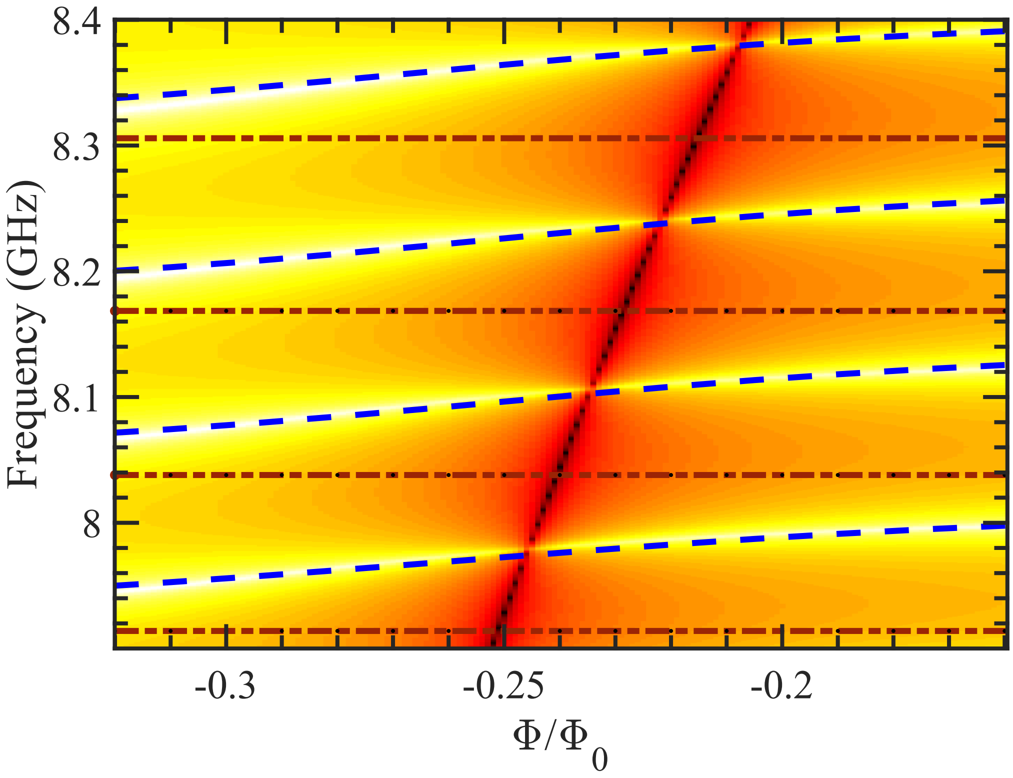

Figure 62: Simulation of hypothetical qubit-metamaterial device to achieve superstrong coupling through AWR circuit simulation of device described in text using parameters in Table 4 and numerical solution to Hamiltonian (blue dashed lines) with adjusted coupling strength values to match features in AWR simulation. Black dotted line corresponds to bare qubit transition frequency. The brown horizontal dashed-dotted lines show the bare frequencies for each of the four modes, 7.91 GHz, 8.04 GHz, 8.17 GHz, and 8.31 GHz, with extracted $g_i/2\pi$ values 220 MHz, 193 MHz, 180 MHz, and 178 MHz, respectively. Figure adapted from from Ref. [97].

exhibit structure in a measurement of $T_1(\omega)$ as the qubit passes through strongly coupled two-level system (TLS) or other spurious resonances at various frequencies [111]. Nonetheless, this gives us a starting point for modeling the frequency dependence of T_1 on our device.

Following the approach outlined in Ref. [101], we model the multi-mode Purcell effect as

$$T_1^{Purcell}(\omega) = (C_Q + 2C_J)/\mathrm{Re}[Y(\omega)], \tag{7.5}$$

where C_Q is the qubit shunt capacitance, C_J is the single junction capacitance, and $Y(\omega)$ is the frequency-dependent complex admittance of the qubit environment. By modeling $Y(\omega)$ for our qubit environment and computing T_1 from Eqs. (7.4, 7.5), we are able to compute the multi-mode Purcell loss curve in Fig. 49(e). The environment for our qubit consists of the impedance of the readout resonator coupled to the qubit $Z_R(\omega)$ and the hybrid metamaterial resonator coupled to the qubit $Z_M(\omega)$: $Y(\omega) = 1/Z_R(\omega) + 1/Z_M(\omega)$. From the coupling to the readout resonator, we have:

$$Z_R(\omega) = \frac{1}{i\omega C_{QR}} + \frac{1}{\frac{1}{Z_{RA}} + \frac{1}{Z_{RB}}}, \tag{7.6}$$

where Z_{RA} and Z_{RB} are the impedances of the two segments of the readout resonator on either side of the coupling element with length $l_A = 6.88$ mm and $l_B = 0.792$ mm, respectively, and given by the standard expression from Ref. [57]:

$$Z_{RA}(\omega) = Z_0 \frac{Z_{LA} + iZ_0 \tanh(\gamma l_A)}{Z_0 + iZ_{LA} \tanh(\gamma l_A)}, \tag{7.7}$$

where $Z_0 = 50\,\Omega$ is the characterstic impedance of the readout resonator transmission line, $Z_{LA} = 1/i\omega C_{cR}^{in} + R_0$ and R_0 is the source impedance on the input line, which is also 50 Ω; $\gamma = \alpha + i\beta$ is the propagation constant, where $\alpha = 10^{-5}\pi/2l_A$ accounts for internal transmission line losses; $\beta = \omega\sqrt{\epsilon}/c$, where ϵ is the effective relative permittivity for the transmission line and c is the speed of light. We get a similar expression for $Z_{RB}(\omega)$, except $Z_{LB} = 1/i\omega C_{cR}^{out} + R_0$.

The impedance coupled to the qubit by the metamaterial resonator is given by

$$Z_M(\omega) = \frac{1}{i\omega C_{QM}} + \frac{1}{\frac{1}{Z_{MA}} + \frac{1}{Z_{MB}}}, \tag{7.8}$$

where Z_{MA} is the impedance of the RHTL segment of length 0.9 mm between the coupling point of the qubit along the RHTL and the output coupling capacitor of the metamaterial, which is described by a similar expression to Eq. (7.7) with $Z_L = 1/i\omega C_{cM}^{out} + R_0$; Z_{MB} is the series impedance of the LHTL line and RHTL segment of length 4 mm.

$$Z_{MB}(\omega) = Z_{0r} \frac{Z_{LHTL} + iZ_{0r} \tanh(\gamma l)}{Z_{0r} + iZ_{LHTL} \tanh(\gamma l)}, \tag{7.9}$$

where Z_{0r} is again 50 Ω and γ is the same as discussed previously following Eq. (7.7); Z_{LHTL} represents the impedance of a LHTL with N unit cells and unit cell length Δx, which we derived previously in Ref. [39]:

$$Z_{LHTL} = Z_{0l} \frac{e^{ikN\Delta x} + \Gamma e^{-ikN\Delta x}}{e^{-ik(-N+\frac{1}{2})\Delta x} - \Gamma e^{ik(-N+\frac{1}{2})\Delta x}}, \tag{7.10}$$

with reflection coefficient

$$\Gamma = \frac{Z_s e^{\frac{-ik\Delta x}{2}} - Z_{0l}}{Z_s e^{\frac{ik\Delta x}{2}} + Z_{0l}}, \tag{7.11}$$

and input impedance

$$Z_s = 1/i\omega C_{cM}^{in} + R_0, \tag{7.12}$$

where R_0 is the source impedance connected to the LHTL input; the characteristic impedance is given by

$$Z_{0l} = \left(i\omega L_r + \frac{1}{i\omega C_l} \right) \Big/ 2i \sin(k\Delta x/2) \ , \tag{7.13}$$

and the wavenumber k can be obtained from the LHTL dispersion relation

$$k(\omega)\Delta x = \cos^{-1} \left[1 - \frac{1}{2} \left(\omega L_r - \frac{1}{\omega C_l} \right) \left(\omega C_r - \frac{1}{\omega L_l} \right) \right]. \tag{7.14}$$

This analysis provides a good qualitative comparison with the measurement (Fig. 49). We see longer T_1 below $\omega_{IR}/2\pi$ and a gradual decrease in T_1 with frequency. We see sharp dips to sub-μs levels when the bare qubit frequency matches the various metamaterial resonances. The analysis also suggests that there the Purcell loss will increase if we go to a qubit-metamaterial system with much larger g_i to be in the superstrong regime. Therefore, it is important to change the other parameters of the device to minimize the Purcell loss as much as possible. For example, if we reduce the metamaterial external coupling capacitors, the impact from Purcell loss on qubit can be reduced.

Chapter 8

Ongoing and Future Work

Here, I briefly discuss the ongoing and future work for metamaterial resonators.

8.1 Next-generation devices and preliminary results

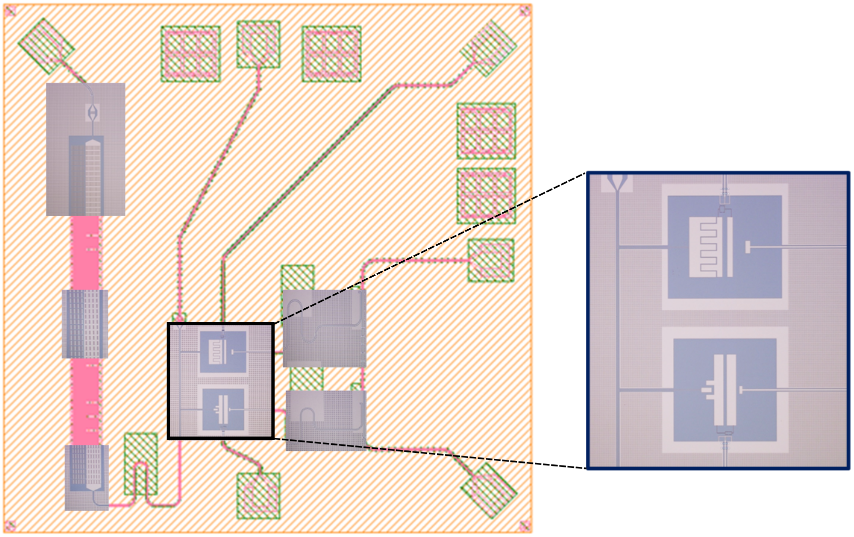

Figure 63: The layout of next-generation qubit-metamaterial device and a few optical images for some of the sections of chip. The zoomed-in image on the right shows the qubit pockets and shunt capacitor pads for the two qubits. The top qubit is more strongly coupled to the metamaterial, while the bottom qubit is weakly coupled to the modes and can be used as a probe. Figure taken from Ref. [112].

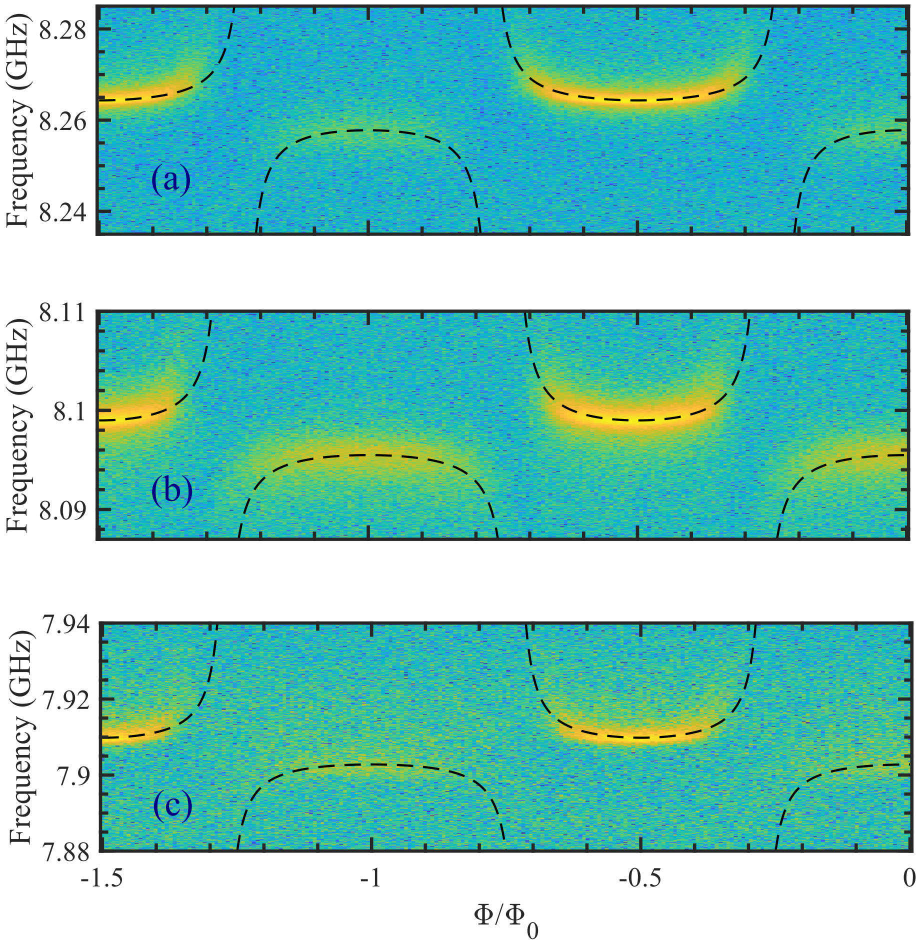

Figure 64: Vacuum Rabi splittings for metmaterial modes (a) 8.26 GHz, (b) 8.1 GHz, and (c) 7.9 GHz. The black dashed line of each plot correspond to the solutions of the Hamiltonian for one mode coupled to one qubit, as described in Sec.7.2. The extracted coupling strength values for the modes are 74 MHz, 54 MHz and 86 MHz respectively. Figure adapted from Ref. [112]

As described in Sec. 7.4, with several improvements to the design of the devices discussed in earlier chapters, it might be possible to achieve superstrong coupling, where $g_i/\Delta\omega_i > 1$, and thus the qubit is strongly coupled to multiple modes simultaenously. Figure 63 shows the layout and optical images for our next generation devices. These devices contain 75 cell LHTL with options to patch either staggered and non-staggered configuration of inductors from the mask. The impedance of metamaterial resonator has been increased to 90 Ohms. The metamaterial is now coupled to two qubits, where one of the qubit is designed to have stronger coupling to possibly acheive multimode coupling; the second qubit is more weakly coupled to the metamaterial for probing the modes individually. Each qubit has a separate readout resonator that is coupled to a feedline for multiplexed readout. Both qubits have on-chip flux bias lines for fast qubit tuning, which could enable us to perform new experiments with the qubit pulsed quickly between operating points below the metmaterial bandgap and resonance with different metamaterial modes [113]. To achieve larger C_{QM}, we are exploring devices with both Xmon and floating design transmons coupled to the metamaterial resonator.

We are currently performing measurements on an ADR for preliminary characterization of these devices and in the future, we will be moving some of these devices to a DR for coherent qubit measurements. Figure 64 shows the vacuum Rabi splitngs for three modes in one of our new devices. We observe that the largest measured g_i value in these devices is ~80 MHz compared to 22 MHz in Device B, a factor of four improvement in the coupling between the qubit and the metamaterial resonator, a step closer to achieve superstrong coupling.

8.2 Ring resonators and preliminary results

Another direction we are exploring is the development of metamaterial ring resonators that are formed from a LHTL wrapped into a ring geometry. Such a structure will have a fundamental resonance corresponding to a full wavelength, but with the same dispersion relation as an LHTL in a linear geometry. Compared to a ring resonator formed from a conventional CPW [114], such a metamaterial ring resonator will have a much more compact physical footprint with more resonant modes in the same frequency range. This ring resonator could then be used to selectively excite the qubits which are coupled around the resonator. A microwave tone at the frequency of one of the ring resonator modes can excite the qubits that are coupled at locations corresponding to voltage antinodes of the particular mode.

Figure 66 show the dispersion relation for a metamaterial ring resonator found using simulation by AWR. We see that the mode frequency decreases with increase in mode number. We see five modes in span of of 2 GHz near the bandedge. The circuit used in the simulations had a 24-cell ring resonator coupled to a feedline

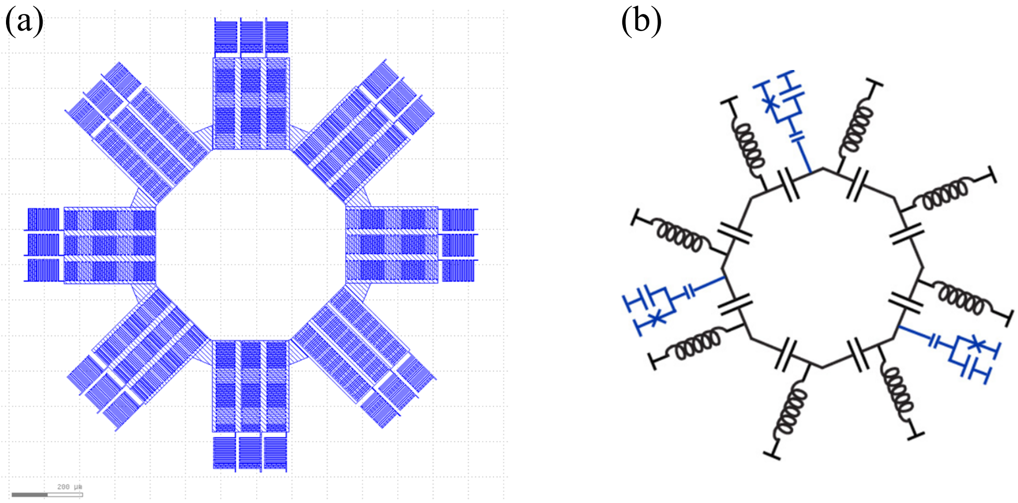

Figure 65: (a) Figure shows a layout for 24 cell metamaterial ring resonator. The diameter of the ring is 1.3 mm. Based on Q3D simulations, each cell is made from a series capacitor C_l=200 fF and L_l=0.5 nH (b) A circuit representation of a metamaterial resonator with three qubits coupled around the ring.

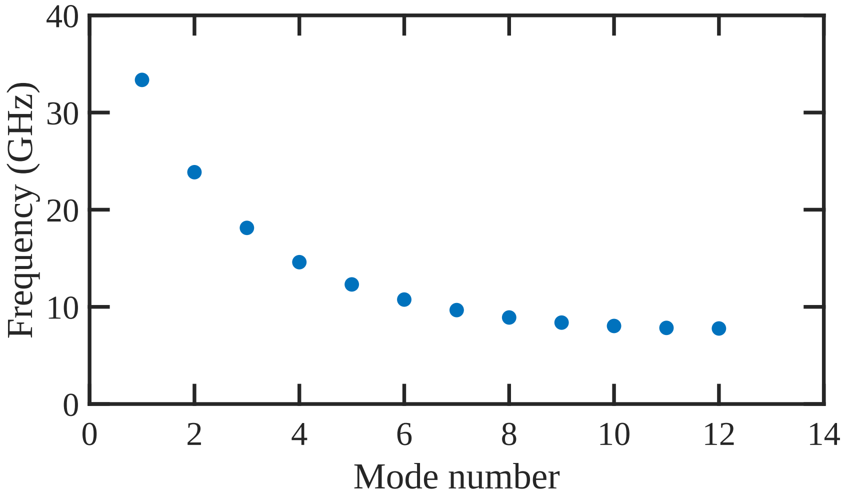

Figure 66: Dispersion relation for a metamterial ring resonator simulated using AWR. Between 8 and 10 GHz, where the band flattens, we can see 5 metamaterial modes.

with coupling capacitor C_c=25 fF. To account for stray reactances, in each cell, we included an inductor L_r=0.03 nH connected in series with capacitor C_l and capacitor

C_r=25 fF conncted in parallel to the inductor L_l. The values are based on the Sonnet simulations done in previous work. Our research group is beginning to fabricate and measure these ring resonators now.

8.3 Outlook

In this thesis, we have studied how to design and characterize a device with qubit coupled to a metamaterial resonator. We have also provided details for increasing the coupling between the qubit and metamaterial resonator. Additonally, we have shown several configurations of the metamaterial resonators that can be used. Using on-chip flux-bias line on the future devices, we could explore new experiments in which, the qubit frequency can be pulsed quickly between operating points below the metamaterial bandgap and resonance with different metamaterial modes [113]; alternatively, for such a device the qubit could be parametrically modulated at the sideband frequency between the qubit transition and a particular metamaterial mode [115]. Both approaches could be used for swapping excitations between the qubit and the metamaterial. Such capabilities would allow for the preparation of complex multimode photonic states in the metamaterial that could be used for analog quantum simulations with microwave photons [33, 110, 116], which could be made to interact through the nonlinearity coupled from the qubit when biased near the mode frequencies. Additionally, this system could be used for a quantum storage with microwave excitations in different metamaterial modes serving as memory elements [35].

It might be possible to make more compact superconducting metamaterial resonators using kinetic inductors made from granular aluminum [117] or NbTiN [118] or Jospephson junctions [116]. Vacuum gap based capacitors can also be used instead of interdigitated capacitors [119].

Appendices

Appendix A

Fabrication

A.1 Fabrication of Device A

This device has only one metal layer.

1. Design the mask:
   - ☐ Design the mask in a layout editor. Klayout editor and several python scripts were used for designing the mask in our case.
   - ☐ Flatten all the layers into a single layer and ensure that all the image objects have atleast 750 μm separation.
2. Make the Mask:
   - ☐ Convert the pattern, so it is compatible with Heidelberg Mask Writer - DWL2000. This include merging the frame file and the pattern file. Frame generator is used to create a barcode and reticle alignment marks.
   - ☐ Write the pattern on a 0.250" thick, 9×9 inch^2 reticle with a photosensitive Cr thin film. Written pattern is scaled 4× of the original dimensions to be compatible with the stepper.
   - ☐ Write the pattern on Heidelberg ask Writer - DWL2000.
   - ☐ Develop and etch Cr using the Hamatech, then strip resist.
3. Photolithography:
   - ☐ Spin 120 nm thick layer of DSK-101-312 photo resist, which is a anti-reflective coating.

☐ 60 second bake at 175 Celsius.
☐ Spin 600 nm thick layer of UV210-0.6 photo resist, which is a positive resist.
☐ 60 second bake at 135 Celsius.
☐ Transfer it to ASML 300C DUV Stepper.
☐ Expose the wafer.
☐ Post exposure bake at 135 Celsius for 90 seconds.
☐ Develop it using AZ 726 MIF.
☐ Descum the wafer Glen 1000 Resist Strip at 100 watts for 120 seconds .

4. Sputtering:

   ☐ Deposit 80 nm thick film of Nb using a sputter system

5. Lift off:

   ☐ Wash it with acetone to remove Nb and UV210-0.6 underlayer.
   ☐ Use AZ726 or heated microposit remover 1165 to remove the bottom DSK-101-312 resist layer.

A.2 Fabrication of Device B

1. Design the mask :

   ☐ Design the mask in layout editor. Klayout used for designing the mask in our case.
   ☐ Flatten all the layers into a single layer and ensure that all the image objects have atleast 750 μm separation.

2. Make the Mask:

   ☐ Convert the pattern, so it is compatible with Heidelberg Mask Writer - DWL2000. This include merging the frame file and the pattern file. Frame generator is used to create a barcode and reticle alignment marks.
   ☐ Write the pattern on a 0.250" thick, 9×9 inch^2 reticle with a photosensitive Cr thin film. Written pattern is scaled 4× of the original dimensions to be compatible with the stepper.
   ☐ Write the pattern on Heidelberg ask Writer - DWL2000.

- ☐ Develop and etch Cr using the Hamatech, then strip resist.

3. Sputtering:
   - ☐ Deposit 80 nm thick film of Nb using a sputter system

4. Photolithography:
   - ☐ Spin DUV42 antireflection (ω=1000, α=500) for 10 seconds.
   - ☐ Bake at 205 C for 60 seconds.
   - ☐ Spin 600 nm thick layer of UVN2300 deep-UV negative resist.
   - ☐ 110 second bake at 60 Celsius.
   - ☐ Transfer it to ASML 300C DUV Stepper.
   - ☐ Expose the wafer.
   - ☐ Post exposure bake at 110 Celsius for 60 seconds.
   - ☐ develop it using AZ 726 MIF.
   - ☐ descum the wafer Glen 1000 Resist Strip at 100 watts for 120 seconds .

5. Etching:
   - ☐ Season the chamber of an inductively coupled plasma etcher (Oxford 80)for 10 minutes with a mixer of BCl_3,Cl_2 and Ar.
   - ☐ Etch the Nb on actual wafer with same recipe.

6. E-beam lithography:
   - ☐ Deposit 600 nm thick layer of methyl metharcylate (MMA) polymer.
   - ☐ Bake at 170 C for 10 minutes.
   - ☐ Deposit 100 nm thick layer of polymethyl metharcylate (PMMA) polymer.
   - ☐ Bake at 170 C for 10 minutes.
   - ☐ Write the pattern using JEOL JBX9500FS Electron Beam Lithography System.

7. Dicing:
   - ☐ Deposit 20 nm thick layer of Al layer using an evaporator (Done with resistive heating CHA evaporator).
   - ☐ Spin UVN2300 for 1 min at 3000 rpm. Bake at 90 C for 2 minutes.
   - ☐ Apply Dicing tape.

- ☐ Dice the wafer into $6.25 \times 6.25\,\mathrm{mm}^2$ chips using DISCO dicing saw.

8. Evaporation:
    - ☐ Develop a single chip for 60 seconds using methyl isobutyl ketone (MIBK).
    - ☐ Load the sample into an Al evaporator.
    - ☐ Ion mill for 13 sec to clean the surface.
    - ☐ Deposit 30 nm thick layer of Al at -12°.
    - ☐ Expose the wafer to a mix Ar/Oxygen for time specific to get desired Al oxide thickness.
    - ☐ Deposit 60 nm thick layer of Al at +11°.
9. Lift off:
    - ☐ Lift off the unwanted Al by soaking chip into dichloromethane (DCM) kept at 40 C for 20 minutes
    - ☐ Clean the chip using isopropyl alcohol.

For future devices, that include on-chip flux bias lines for the qubits, ground straps across all feedlines and bias lines are fabricated to prevent interference from undefined return paths of the current from flux bias lines and to maintain the equipotential across the ground plane of the chip.

Bibliography

[1] https://www.computerhistory.org/timeline/computers/.

[2] Tom Mitchell. *Machine Learning.* McGraw Hills, 1997.

[3] Gordon E. Moore. Cramming more components onto integrated circuits, reprinted from electronics, volume 38, number 8, april 19, 1965, pp.114 ff. *IEEE Solid-State Circuits Society Newsletter*, 11(3):33–35, 2006.

[4] B. Doris, Meikei Ieong, T. Kanarsky, Ying Zhang, R.A. Roy, O. Dokumaci, Zhibin Ren, Fen-Fen Jamin, Leathen Shi, W. Natzle, Hsiang-Jen Huang, J. Mezzapelle, A. Mocuta, S. Womack, M. Gribelyuk, E.C. Jones, R.J. Miller, H.-S.P. Wong, and W. Haensch. Extreme scaling with ultra-thin si channel mosfets. In *Digest. International Electron Devices Meeting,*, pages 267–270, 2002.

[5] TSMC foundary. `https://www.tsmc.com/english/dedicatedFoundry/technology/logic/l_7nm`.

[6] Peter W Shor. Polynomial-time algorithms for prime factorization and discrete logarithms on a quantum computer. 26(5):1484–1509, 1997.

[7] Y. Nakamura, Yu A. Pashkin, and J. S. Tsai. Coherent control of macroscopic quantum states in a single-Cooper-pair box. *Nature*, 398(6730):786–788, 1999.

[8] D. Vion, A. Aassime, A. Cottet, P. Joyez, H. Pothier, C. Urbina, D. Esteve, and M. H. Devoret. Manipulating the quantum state of an electrical circuit. *Science*, 296(5569):886–889, 2002.

[9] J. A. Schreier, A. A. Houck, Jens Koch, D. I. Schuster, B. R. Johnson, J. M. Chow, J. M. Gambetta, J. Majer, L. Frunzio, M. H. Devoret, S. M. Girvin,

and R. J. Schoelkopf. Suppressing charge noise decoherence in superconducting charge qubits. *Phys. Rev. B*, 77:180502, 2008.

[10] Nicolai Friis, Oliver Marty, Christine Maier, Cornelius Hempel, Milan Holzäpfel, Petar Jurcevic, Martin B. Plenio, Marcus Huber, Christian Roos, Rainer Blatt, and Ben Lanyon. Observation of entangled states of a fully controlled 20-qubit system. *Phys. Rev. X*, 8:021012, 2018.

[11] Rainer Blatt and David Wineland. Entangled states of trapped atomic ions. *Nature*, 453(7198):1008–1015, 2008.

[12] E. Knill, R. Laflamme, and G. J. Milburn. A scheme for efficient quantum computation with linear optics. *Nature*, 409(6816):46–52, 2001.

[13] J M Arrazola, V Bergholm, K Brádler, T R Bromley, M J Collins, I Dhand, A Fumagalli, T Gerrits, A Goussev, L G Helt, J Hundal, T Isacsson, R B Israel, J Izaac, S Jahangiri, R Janik, N Killoran, S P Kumar, J Lavoie, A E Lita, D H Mahler, M Menotti, B Morrison, S W Nam, L Neuhaus, H Y Qi, N Quesada, A Repingon, K K Sabapathy, M Schuld, D Su, J Swinarton, A Száva, K Tan, P Tan, V D Vaidya, Z Vernon, Z Zabaneh, and Y Zhang. Quantum circuits with many photons on a programmable nanophotonic chip. *Nature*, 591, 2021.

[14] Jonathan C.F. Matthews, Alberto Politi, André Stefanov, and Jeremy L. O'Brien. Manipulation of multiphoton entanglement in waveguide quantum circuits. *Nature Photonics*, 3(6):346–350, 2009.

[15] M. Saffman, T. G. Walker, and K. Mølmer. Quantum information with rydberg atoms. *Rev. Mod. Phys.*, 82:2313–2363, 2010.

[16] Antoine Browaeys and Thierry Lahaye. Many-body physics with individually controlled Rydberg atoms. *Nature Physics*, 16(2):132–142, 2020.

[17] Sepehr Ebadi, Tout T. Wang, Harry Levine, Alexander Keesling, Giulia Semeghini, Ahmed Omran, Dolev Bluvstein, Rhine Samajdar, Hannes Pichler, Wen Wei Ho, Soonwon Choi, Subir Sachdev, Markus Greiner, Vladan Vuletić, and Mikhail D. Lukin. Quantum phases of matter on a 256-atom programmable quantum simulator - Nature. *Nature*, 595:227–232, Jul 2021.

[18] Rutger Vrijen, Eli Yablonovitch, Kang Wang, Hong Wen Jiang, Alex Balandin, Vwani Roychowdhury, Tal Mor, and David DiVincenzo. Electron-spin-resonance transistors for quantum computing in silicon-germanium heterostructures. *Phys. Rev. A*, 62:012306, 2000.

[19] Jun Yoneda, Kenta Takeda, Tomohiro Otsuka, Takashi Nakajima, Matthieu R Delbecq, Giles Allison, Takumu Honda, Tetsuo Kodera, Shunri Oda, Yusuke Hoshi, Noritaka Usami, Kohei M Itoh, and Seigo Tarucha. A quantum-dot spin qubit with coherence limited by charge noise and fidelity higher than 99.9%. *Nature Nanotechnology*, 13, 2018.

[20] A.Yu. Kitaev. Fault-tolerant quantum computation by anyons. *Annals of Physics*, 303(1):2–30, 2003.

[21] Torsten Karzig, William S. Cole, and Dmitry I. Pikulin. Quasiparticle poisoning of majorana qubits. *Phys. Rev. Lett.*, 126:057702, 2021.

[22] Frank Arute, Kunal Arya, Ryan Babbush, Dave Bacon, Joseph C. Bardin, Rami Barends, Rupak Biswas, Sergio Boixo, Fernando G.S.L. Brandao, David A. Buell, Brian Burkett, Yu Chen, Zijun Chen, Ben Chiaro, Roberto Collins, William Courtney, Andrew Dunsworth, Edward Farhi, Brooks Foxen, Austin Fowler, Craig Gidney, Marissa Giustina, Rob Graff, Keith Guerin, Steve Habegger, Matthew P. Harrigan, Michael J. Hartmann, Alan Ho, Markus Hoffmann, Trent Huang, Travis S. Humble, Sergei V. Isakov, Evan Jeffrey, Zhang Jiang, Dvir Kafri, Kostyantyn Kechedzhi, Julian Kelly, Paul V. Klimov, Sergey Knysh, Alexander Korotkov, Fedor Kostritsa, David Landhuis, Mike Lindmark, Erik Lucero, Dmitry Lyakh, Salvatore Mandrà, Jarrod R. McClean, Matthew McEwen, Anthony Megrant, Xiao Mi, Kristel Michielsen, Masoud Mohseni, Josh Mutus, Ofer Naaman, Matthew Neeley, Charles Neill, Murphy Yuezhen Niu, Eric Ostby, Andre Petukhov, John C. Platt, Chris Quintana, Eleanor G. Rieffel, Pedram Roushan, Nicholas C. Rubin, Daniel Sank, Kevin J. Satzinger, Vadim Smelyanskiy, Kevin J. Sung, Matthew D. Trevithick, Amit Vainsencher, Benjamin Villalonga, Theodore White, Z. Jamie Yao, Ping Yeh, Adam Zalcman, Hartmut Neven, and John M. Martinis. Quantum supremacy using a programmable superconducting processor. *Nature*, 574(7779):505–510, 2019.

[23] Yulin Wu, Wan-Su Bao, Sirui Cao, Fusheng Chen, Ming-Cheng Chen, Xiawei Chen, Tung-Hsun Chung, Hui Deng, Yajie Du, Daojin Fan, Ming Gong, Cheng Guo, Chu Guo, Shaojun Guo, Lianchen Han, Linyin Hong, He-Liang Huang, Yong-Heng Huo, Liping Li, Na Li, Shaowei Li, Yuan Li, Futian Liang, Chun Lin, Jin Lin, Haoran Qian, Dan Qiao, Hao Rong, Hong Su, Lihua Sun, Liangyuan Wang, Shiyu Wang, Dachao Wu, Yu Xu, Kai Yan, Weifeng Yang, Yang Yang, Yangsen Ye, Jianghan Yin, Chong Ying, Jiale Yu, Chen Zha, Cha Zhang, Haibin Zhang, Kaili Zhang, Yiming Zhang, Han Zhao, Youwei Zhao, Liang Zhou, Qingling Zhu, Chao-Yang Lu, Cheng-Zhi Peng, Xiaobo Zhu, and Jian-Wei Pan. Strong quantum computational advantage using a superconducting quantum processor. *arXiv*, 2021.

[24] R. Barends, J. Kelly, A. Megrant, A. Veitia, D. Sank, E. Jeffrey, T. C. White, J. Mutus, A. G. Fowler, B. Campbell, Y. Chen, Z. Chen, B. Chiaro, A. Dunsworth, C. Neill, P. O'Malley, P. Roushan, A. Vainsencher, J. Wenner, A. N. Korotkov, A. N. Cleland, and John M. Martinis. Superconducting quantum circuits at the surface code threshold for fault tolerance - Nature. *Nature*, 508:500–503, 2014.

[25] John Preskill. Quantum Computing in the NISQ era and beyond. *Quantum*, 2:79, 2018.

[26] Kishor Bharti, Alba Cervera-Lierta, Thi Ha Kyaw, Tobias Haug, Sumner Alperin-Lea, Abhinav Anand, Matthias Degroote, Hermanni Heimonen, Jakob S Kottmann, Tim Menke, Wai-Keong Mok, Sukin Sim, Leong-Chuan Kwek, and Alán Aspuru-Guzik. Noisy intermediate-scale quantum (NISQ) algorithms.

[27] Matthew P. Harrigan, Kevin J. Sung, Matthew Neeley, Kevin J. Satzinger, Frank Arute, Kunal Arya, Juan Atalaya, Joseph C. Bardin, Rami Barends, Sergio Boixo, Michael Broughton, Bob B. Buckley, David A. Buell, Brian Burkett, Nicholas Bushnell, Yu Chen, Zijun Chen, Ben Chiaro, Roberto Collins, William Courtney, Sean Demura, Andrew Dunsworth, Daniel Eppens, Austin Fowler, Brooks Foxen, Craig Gidney, Marissa Giustina, Rob Graff, Steve Habegger, Alan Ho, Sabrina Hong, Trent Huang, L. B. Ioffe, Sergei V. Isakov, Evan

Jeffrey, Zhang Jiang, Cody Jones, Dvir Kafri, Kostyantyn Kechedzhi, Julian Kelly, Seon Kim, Paul V. Klimov, Alexander N. Korotkov, Fedor Kostritsa, David Landhuis, Pavel Laptev, Mike Lindmark, Martin Leib, Orion Martin, John M. Martinis, Jarrod R. McClean, Matt McEwen, Anthony Megrant, Xiao Mi, Masoud Mohseni, Wojciech Mruczkiewicz, Josh Mutus, Ofer Naaman, Charles Neill, Florian Neukart, Murphy Yuezhen Niu, Thomas E. O'Brien, Bryan O'Gorman, Eric Ostby, Andre Petukhov, Harald Putterman, Chris Quintana, Pedram Roushan, Nicholas C. Rubin, Daniel Sank, Andrea Skolik, Vadim Smelyanskiy, Doug Strain, Michael Streif, Marco Szalay, Amit Vainsencher, Theodore White, Z. Jamie Yao, Ping Yeh, Adam Zalcman, Leo Zhou, Hartmut Neven, Dave Bacon, Erik Lucero, Edward Farhi, and Ryan Babbush. Quantum approximate optimization of non-planar graph problems on a planar superconducting processor. *Nature Physics*, 17(3):332–336, 2021.

[28] Google. Hartree-Fock on a superconducting qubit quantum computer. *Science*, 369:1084–1089, 2020.

[29] D.F. Walls and G.J. Milburn. *Quantum Optics*. Springer, 1994.

[30] T. Niemczyk, F. Deppe, H. Huebl, E. P. Menzel, F. Hocke, M. J. Schwarz, J. J. Garcia-Ripoll, D. Zueco, T. Hümmer, E. Solano, A. Marx, and R. Gross. Circuit quantum electrodynamics in the ultrastrong-coupling regime. *Nat. Phys.*, 6(10):772–776, 2010.

[31] Sal J. Bosman, Mario F. Gely, Vibhor Singh, Daniel Bothner, Andres Castellanos-Gomez, and Gary A. Steele. Approaching ultrastrong coupling in transmon circuit QED using a high-impedance resonator. *Physical Review B*, 95(22):1–4, 2017.

[32] Roman Kuzmin, Nitish Mehta, Nicholas Grabon, Raymond Mencia, and Vladimir E Manucharyan. Superstrong coupling in circuit quantum electrodynamics. *npj Quant. Inform.*, 5(20):20, 2019.

[33] D. J. Egger and F. K. Wilhelm. Multimode circuit quantum electrodynamics with hybrid metamaterial transmission lines. *Phys. Rev. Lett.*, 111:163601, 2013.

[34] Juha Leppäkangas, Jochen Braumüller, Melanie Hauck, Jan-Michael Reiner, Iris Schwenk, Sebastian Zanker, Lukas Fritz, Alexey V. Ustinov, Martin Weides, and Michael Marthaler. Quantum simulation of the spin-boson model with a microwave circuit. *Phys. Rev. A*, 97:052321, May 2018.

[35] RK Naik, N Leung, S Chakram, Peter Groszkowski, Y Lu, N Earnest, DC McKay, Jens Koch, and DI Schuster. Random access quantum information processors using multimode circuit quantum electrodynamics. *Nat. Commun.*, 8(1):1904, 2017.

[36] Tzu-Chieh Wei and Paul M. Goldbart. Geometric measure of entanglement and applications to bipartite and multipartite quantum states. *Phys. Rev. A*, 68:042307, 2003.

[37] George V Eleftheriades, Ashwin K Iyer, and Peter C Kremer. Planar negative refractive index media using periodically lc loaded transmission lines. *IEEE Trans. Microwave Theory Tech.*, 50(12):2702–2712, 2002.

[38] Chrirtophe Caloz and T Itoh. Transmission line approach of left-handed (LH) materials and microstrip implementation of an artificial lh transmission line. *IEEE Trans. Antennas Propag.*, 52(5):1159–1166, 2004.

[39] H. Wang, A. P. Zhuravel, S. Indrajeet, B. G. Taketani, M. D. Hutchings, Y. Hao, F. Rouxinol, F. K. Wilhelm, M. D. LaHaye, A. V. Ustinov, and B. L. T. Plourde. Mode structure in superconducting metamaterial transmission-line resonators. *Phys. Rev. Applied*, 11:054062, 2019.

[40] J. Bardeen, L. N. Cooper, and J. R. Schrieffer. Theory of superconductivity. *Physical Review*, 108(5):1175–1204, 1957.

[41] Michael Tinkham. *Introduction to Superconductivity,*. Dover Publications, 1996.

[42] Vinay Ambegaokar and Alexis Baratoff. Tunneling between superconductors. *Phys. Rev. Lett.*, 10:486–489, Jun 1963.

[43] P. Krantz, M. Kjaergaard, F. Yan, T. P. Orlando, S. Gustavsson, and W. D. Oliver. A quantum engineer's guide to superconducting qubits. *Applied Physics Reviews*, 6(2), 2019.

[44] Jens Koch, M Yu Terri, Jay Gambetta, Andrew A Houck, DI Schuster, J Majer, Alexandre Blais, Michel H Devoret, Steven M Girvin, and Robert J Schoelkopf. Charge-insensitive qubit design derived from the cooper pair box. *Phys. Rev. A*, 76(4):042319, 2007.

[45] Jerry M Chow, Jay M Gambetta, Easwar Magesan, David W Abraham, Andrew W Cross, B R Johnson, Nicholas A Masluk, Colm A Ryan, John A Smolin, Srikanth J Srinivasan, and M Steffen. Implementing a strand of a scalable fault-tolerant quantum computing fabric. *Nature communications*, 5:4015, 2014.

[46] Jerry M. Chow, Srikanth J. Srinivasan, , Easwar Magesan, A. D. Córcoles, David W. Abraham, Jay M. Gambetta, and Matthias Steffen. Characterizing a four-qubit planar lattice for arbitrary error detection. In *Quantum Information and Computation XIII*, volume 9500. International Society for Optics and Photonics, 2015.

[47] A. D. Córcoles, Easwar Magesan, Srikanth J. Srinivasan, Andrew W. Cross, M. Steffen, Jay M. Gambetta, and Jerry M. Chow. Demonstration of a quantum error detection code using a square lattice of four superconducting qubits. *Nature Communications*, 6(1):1–10, 2015.

[48] M. D. Hutchings, J. B. Hertzberg, Y. Liu, N. T. Bronn, G. A. Keefe, Markus Brink, Jerry M. Chow, and B. L. T. Plourde. Tunable superconducting qubits with flux-independent coherence. *Phys. Rev. Appl.*, 8:044003, Oct 2017.

[49] E.T. Jaynes and F.W. Cummings. Comparison of quantum and semiclassical radiation theories with application to the beam maser. *Proceedings of the IEEE*, 51(1):89–109, 1963.

[50] Alexandre Blais, Ren-Shou Huang, Andreas Wallraff, S. M. Girvin, and R. J. Schoelkopf. Cavity quantum electrodynamics for superconducting electrical circuits: An architecture for quantum computation. *Phys. Rev. A*, 69:062320, 2004.

[51] D. I. Schuster, A. A Houck, J. A. Schreier, A. Wallraff, J M Gambetta, A Blais, L Frunzio, J Majer, B Johnson, M H Devoret, S M Girvin, and R J

Schoelkopf. Resolving photon number states in a superconducting circuit. *Nature*, 445(7127):515–518, 2007.

[52] D. I. Schuster, A. Wallraff, A. Blais, L. Frunzio, R.-S. Huang, J. Majer, S. M. Girvin, and R. J. Schoelkopf. ac stark shift and dephasing of a superconducting qubit strongly coupled to a cavity field. *Phys. Rev. Lett.*, 94:123602, Mar 2005.

[53] Andreas Wallraff, David I Schuster, Alexandre Blais, L Frunzio, R-S Huang, J Majer, S Kumar, Steven M Girvin, and Robert J Schoelkopf. Strong coupling of a single photon to a superconducting qubit using circuit quantum electrodynamics. *Nature*, 431(7005):162, 2004.

[54] Hanhee Paik, DI Schuster, Lev S Bishop, G Kirchmair, G Catelani, AP Sears, BR Johnson, MJ Reagor, L Frunzio, LI Glazman, et al. Observation of high coherence in josephson junction qubits measured in a three-dimensional circuit qed architecture. *Phys. Rev. Lett.*, 107(24):240501, 2011.

[55] Matthew Reagor, Wolfgang Pfaff, Christopher Axline, Reinier W. Heeres, Nissim Ofek, Katrina Sliwa, Eric Holland, Chen Wang, Jacob Blumoff, Kevin Chou, Michael J. Hatridge, Luigi Frunzio, Michel H. Devoret, Liang Jiang, and Robert J. Schoelkopf. Quantum memory with millisecond coherence in circuit qed. *Phys. Rev. B*, 94:014506, Jul 2016.

[56] M Göppl, A Fragner, M Baur, R Bianchetti, S Filipp, JM Fink, PJ Leek, G Puebla, L Steffen, and Andreas Wallraff. Coplanar waveguide resonators for circuit quantum electrodynamics. *J. Appl. Phys.*, 104(11):113904, 2008.

[57] David M Pozar. *Microwave Engineering.* John Wiley & Sons, 2009.

[58] A P Sears, A Petrenko, G Catelani, L Sun, Hanhee Paik, G Kirchmair, L Frunzio, L I Glazman, S M Girvin, and R J Schoelkopf. Photon shot noise dephasing in the strong-dispersive limit of circuit QED. *RAPID COMMUNICATIONS PHYSICAL REVIEW B*, 86(5):180504, 2012.

[59] Haozhi Wang. *Fabrication and Characterization of Superconducting Metamaterial Resonators.* PhD thesis, Syracuse University, 2018.

[60] Viktor G Veselago. The electrodynamics of substances with simultaneously negative values of ϵ and μ. *Soviet Physics Uspekhi*, 10(4):509–514, 1968.

[61] R. A. Shelby, D. R. Smith, and S. Schultz. Experimental verification of a negative index of refraction. *Science*, 292(5514):77–79, 2001.

[62] John Brian Pendry. Negative refraction makes a perfect lens. *Phys. Rev. Lett.*, 85(18):3966, 2000.

[63] Xiaoyu Zheng, Howon Lee, Todd H. Weisgraber, Maxim Shusteff, Joshua DeOtte, Eric B. Duoss, Joshua D. Kuntz, Monika M. Biener, Qi Ge, Julie A. Jackson, Sergei O. Kucheyev, Nicholas X. Fang, and Christopher M. Spadaccini. Ultralight, ultrastiff mechanical metamaterials. *Science*, 344(6190):1373–1377, 2014.

[64] Zhengyou Liu, Xixiang Zhang, Yiwei Mao, Y. Y. Zhu, Zhiyu Yang, C. T. Chan, and Ping Sheng. Locally resonant sonic materials. *Science*, 289(5485):1734–1736, 2000.

[65] Shu Zhang, Leilei Yin, and Nicholas Fang. Focusing ultrasound with an acoustic metamaterial network. *Phys. Rev. Lett.*, 102:194301, 2009.

[66] Alexander A. High, Robert C. Devlin, Alan Dibos, Mark Polking, Dominik S. Wild, Janos Perczel, Nathalie P. De Leon, Mikhail D. Lukin, and Hongkun Park. Visible-frequency hyperbolic metasurface. *Nature*, 522(7555):192–196, 2015.

[67] John D. Joannopoulos, Steven G. Johnson, Joshua N. Winn, and Robert D. Meade. *Photonic Crystals: Molding the Flow of Light.* Princeton University Press, 2008.

[68] J.D. Jackson. *Classical Electrodyanmics.* Wiley, New York, NY, 1991.

[69] Ming Lun Tseng, Hui Hsin Hsiao, Cheng Hung Chu, Mu Ku Chen, Greg Sun, Ai Qun Liu, and Din Ping Tsai. Metalenses: Advances and Applications. *Advanced Optical Materials*, 6(18), 2018.

[70] Zhaoyi Li, Peng Lin, Yao-Wei Huang, Joon-Suh Park, Wei Ting Chen, Zhujun Shi, Cheng-Wei Qiu, Ji-Xin Cheng, and Federico Capasso. Meta-optics achieves RGB-achromatic focusing for virtual reality. *Sci. Adv*, 7:4458–4485, 2021.

[71] Atsushi Sanada, Christophe Caloz, and Tatsuo Itoh. Novel zeroth-order resonance in composite right/left-handed transmission line resonators. In *Proc. 2003 Asia-Pacific Microwave Conf.*, volume 3, pages 1588–1591, 2003.

[72] Christophe Caloz, Atsushi Sanada, and Tatsuo Itoh. A novel composite right-/left-handed coupled-line directional coupler with arbitrary coupling level and broad bandwidth. *IEEE Trans. Microwave Theory Techn.*, 52(3):980–992, 2004.

[73] Christophe Caloz and Tatsuo Itoh. *Electromagnetic Metamaterials: Transmission Line Theory and Microwave Applications.* John Wiley & Sons, 2005.

[74] Neereja M. Sundaresan, Yanbing Liu, Darius Sadri, László J. Szőcs, Devin L. Underwood, Moein Malekakhlagh, Hakan E. Türeci, and Andrew A. Houck. Beyond strong coupling in a multimode cavity. *Phys. Rev. X*, 5:021035, Jun 2015.

[75] Mohammad Mirhosseini, Eunjong Kim, Vinicius S. Ferreira, Mahmoud Kalaee, Alp Sipahigil, Andrew J. Keller, and Oskar Painter. Superconducting metamaterials for waveguide quantum electrodynamics. *Nat. Commun.*, 9(1):3706, 2018.

[76] Javier Puertas Martinez, Sebastien Leger, Nicolas Gheeraert, Remy Dassonneville, Luca Planat, Farshad Foroughi, Yuriy Krupko, Olivier Buisson, Cecile Naud, Wiebke Guichard, Serge Florens, Izak Snyman, and Nicolas Roch. A tunable Josephson platform to explore many-body quantum optics in circuit-QED. *npj Quant. Inform.*, 5(1):19, 2019.

[77] Carsten Hutter, Erik A. Tholén, Kai Stannigel, Jack Lidmar, and David B. Haviland. Josephson junction transmission lines as tunable artificial crystals. *Phys. Rev. B*, 83(1):1–8, 2011.

[78] J Majer, JM Chow, JM Gambetta, Jens Koch, BR Johnson, JA Schreier,

L Frunzio, DI Schuster, AA Houck, Andreas Wallraff, et al. Coupling superconducting qubits via a cavity bus. *Nature*, 449(7161):443, 2007.

[79] Zenghui Bao, Zhiling Wang, Yukai Wu, Yan Li, Cheng Ma, Yipu Song, Hongyi Zhang, and Luming Duan. On-Demand Storage and Retrieval of Microwave Photons Using a Superconducting Multiresonator Quantum Memory. *Phys. Rev. Lett.*, 127(1):010503, 2021.

[80] BLT Plourde, Haozhi Wang, Francisco Rouxinol, and MD LaHaye. Superconducting metamaterials and qubits. In *Quantum Information and Computation XIII*, volume 9500, page 95000M. International Society for Optics and Photonics, 2015.

[81] Jay Gambetta, Alexandre Blais, M Boissonneault, A A Houck, D I Schuster, and S M Girvin. Quantum trajectory approach to circuit QED: Quantum jumps and the Zeno effect.

[82] R. Meservey and P. M. Tedrow. Measurements of the kinetic inductance of superconducting linear structures. *Journal of Applied Physics*, 40(5):2028–2034, 1969.

[83] D C Mattist and J Bardeen. Theory of the Anomalous Skin Effect in Normal and Superconducting Metals*. *Physical Review*, 111(2):412–417, 1958.

[84] B T Matthias, T H Geballe, and V B Compton. Superconductivity. *Rev. Mod. Phys.*, 35(1):1, 1963.

[85] David P Pappas, Michael R Vissers, David S Wisbey, Jeffrey S Kline, and Jiansong Gao. Two level system loss in superconducting microwave resonators. *IEEE Trans. Appl. Supercond.*, 21(3):871–874, 2011.

[86] David S. Wisbey, Jiansong Gao, Michael R. Vissers, Fabio C.S. Da Silva, Jeffrey S. Kline, Leila Vale, and David P. Pappas. Effect of metal/substrate interfaces on radio-frequency loss in superconducting coplanar waveguides. *Journal of Applied Physics*, 108(9), 2010.

[87] Jiansong Gao. *The physics of superconducting microwave resonators.* PhD thesis, 2008.

[88] Ibrahim Nsanzineza. *Vortices and Quasiparticels in Superconducting Microwave Resonators*. PhD thesis, 2016.

[89] Aaron D O'Connell, M Ansmann, Radoslaw C Bialczak, Max Hofheinz, Nadav Katz, Erik Lucero, C McKenney, Matthew Neeley, Haohua Wang, Eva M Weig, et al. Microwave dielectric loss at single photon energies and millikelvin temperatures. *Appl. Phys. Lett.*, 92(11):112903, 2008.

[90] John M Martinis, Ken B Cooper, Robert McDermott, Matthias Steffen, Markus Ansmann, KD Osborn, Katarina Cicak, Seongshik Oh, David P Pappas, Raymond W Simmonds, et al. Decoherence in Josephson qubits from dielectric loss. *Phys. Rev. Lett.*, 95(21):210503, 2005.

[91] Cihan Kurter, Alexander P Zhuravel, Alexey V Ustinov, and Steven M Anlage. Microscopic examination of hot spots giving rise to nonlinearity in superconducting resonators. *Phys. Rev. B*, 84(10):104515, 2011.

[92] Alexander P Zhuravel, Steven M Anlage, and Alexey V Ustinov. Measurement of local reactive and resistive photoresponse of a superconducting microwave device. *Appl. Phys. Lett.*, 88(21):212503, 2006.

[93] AP Zhuravel, AG Sivakov, OG Turutanov, AN Omelyanchouk, Steven M Anlage, A Lukashenko, AV Ustinov, and D Abraimov. Laser scanning microscopy of hts films and devices. *Low Temperat. Phys.*, 32(6):592–607, 2006.

[94] James C Culbertson, Harvey S Newman, and Charles Wilker. Optical probe of microwave current distributions in high temperature superconducting transmission lines. *J. Appl. Phys.*, 84(5):2768–2787, 1998.

[95] Frank Pobell. *Matter and Methods at Low Temperatures.* Springer, Berlin, Heidelberg, 2007.

[96] Raytheon BBN Technologies. Qlab measurement and control software. https://github.com/BBN-Q/Qlab.

[97] S. Indrajeet, H. Wang, M. D. Hutchings, B. G. Taketani, Frank K. Wilhelm, M. D. LaHaye, and B. L.T. Plourde. Coupling a Superconducting Qubit to a

Left-Handed Metamaterial Resonator. *Physical Review Applied*, 14(6):064033, 2020.

[98] A Wallraff, D Schuster, A Blais, L Frunzio, R Huang, J Majer, S Kumar, S Girvin, and R Schoelkopf. Strong coupling of a single photon to a superconducting qubit using circuit quantum electrodynamics. *Nature*, 431(7005):162–167, 2004.

[99] David Isaac Schuster. *Circuit Quantum Electrodynamics*. PhD thesis, Yale University, 2007.

[100] Cadence. AWR Design Enviroment. version 12.03.

[101] A. A. Houck, J. A. Schreier, B. R. Johnson, J. M. Chow, Jens Koch, J. M. Gambetta, D. I. Schuster, L. Frunzio, M. H. Devoret, S. M. Girvin, and R. J. Schoelkopf. Controlling the spontaneous emission of a superconducting transmon qubit. *Phys. Rev. Lett.*, 101:080502, Aug 2008.

[102] J.-L. Orgiazzi, C. Deng, D. Layden, R. Marchildon, F. Kitapli, F. Shen, M. Bal, F. R. Ong, and A. Lupascu. Flux qubits in a planar circuit quantum electrodynamics architecture: Quantum control and decoherence. *Phys. Rev. B*, 93(10):104518, Mar 2016.

[103] M. Stern, G. Catelani, Y. Kubo, C. Grezes, A. Bienfait, D. Vion, D. Esteve, and P. Bertet. Flux Qubits with Long Coherence Times for Hybrid Quantum Circuits. *Phys. Rev. Lett.*, 113(12):123601, Sep 2014.

[104] Radoslaw C. Bialczak, R. McDermott, M. Ansmann, M. Hofheinz, N. Katz, Erik Lucero, Matthew Neeley, A. D. O'Connell, H. Wang, A. N. Cleland, and John M. Martinis. $1/f$ Flux Noise in Josephson Phase Qubits. *Phys. Rev. Lett.*, 99(18):187006, Nov 2007.

[105] Frederick C. Wellstood, Cristian Urbina, and John Clarke. Low-frequency noise in dc superconducting quantum interference devices below 1 K. *Appl. Phys. Lett.*, 50(12):772–774, Mar 1987.

[106] Sonnet. Sonnet suites. version 16.52.

[107] Cadence Design Systems. Awr api scripting guide. `www.awrcorp.com/download/faq/english/docs/ApiReference/API.htm`.

[108] J Wenner, M Neeley, Radoslaw C Bialczak, M Lenander, Erik Lucero, A D O'Connell, D Sank, H Wang, M Weides, A N Cleland, and John M Martinis. Wirebond crosstalk and cavity modes in large chip mounts for superconducting qubits. *Supercond. Sci. Technol.*, 24(6):065001, 2011.

[109] ANSYS. ANSYS Q3D Extractor. Version.

[110] A. Messinger, B. G. Taketani, and F. K. Wilhelm. Left-handed superlattice metamaterials for circuit QED. *Phys. Rev. A*, 99:032325, 2019.

[111] R. Barends, J. Kelly, A. Megrant, D. Sank, E. Jeffrey, Y. Chen, Y. Yin, B. Chiaro, J. Mutus, C. Neill, P. O'Malley, P. Roushan, J. Wenner, T. C. White, A. N. Cleland, and John M. Martinis. Coherent josephson qubit suitable for scalable quantum integrated circuits. *Phys. Rev. Lett.*, 111:080502, Aug 2013.

[112] T McBroom, S. Indrajeet, B. Cole, and B Plourde. Superstrong coupling between a transmon and a metamaterial resonator. In *APS March Meeting 2021, R30.00007*, 2021.

[113] Max Hofheinz, E. M. Weig, M. Ansmann, Radoslaw C. Bialczak, Erik Lucero, M. Neeley, A. D. O'Connell, H. Wang, John M. Martinis, and A. N. Cleland. Generation of Fock states in a superconducting quantum circuit. *Nature*, 454(7202):310–314, 2008.

[114] Wenhui Huang, Yuxuan Zhou, Ziyu Tao, Libo Zhang, Song Liu, Yuanzhen Chen, Tongxing Yan, and Dapeng Yu. A superconducting coplanar waveguide ring resonator as quantum bus for circuit quantum electrodynamics. *Appl. Phys. Lett.*, 118(18):184001, 2021.

[115] J. D. Strand, Matthew Ware, Félix Beaudoin, T. A. Ohki, B. R. Johnson, Alexandre Blais, and B. L. T. Plourde. First-order sideband transitions with flux-driven asymmetric transmon qubits. *Phys. Rev. B*, 87(22):220505, 2013.

[116] Marco Scigliuzzo, Giuseppe Calajò, Francesco Ciccarello, Daniel Perez Lozano, Andreas Bengtsson, Pasquale Scarlino, Andreas Wallraff, Darrick Chang, Per Delsing, and Simone Gasparinetti. Extensible quantum simulation architecture based on atom-photon bound states in an array of high-impedance resonators. *arXiv*, Jul 2021.

[117] H Rotzinger, S T Skacel, M Pfirrmann, J N Voss, J Münzberg, S Probst, P Bushev, M P Weides, A V Ustinov, and J E Mooij. Aluminium-oxide wires for superconducting high kinetic inductance circuits. *Superconductor Science and Technology*, 30(2):025002, 2016.

[118] N. Samkharadze, A. Bruno, P. Scarlino, G. Zheng, D. P. DiVincenzo, L. DiCarlo, and L. M. K. Vandersypen. High-kinetic-inductance superconducting nanowire resonators for circuit qed in a magnetic field. *Phys. Rev. Applied*, 5:044004, 2016.

[119] Katarina Cicak, Michael S. Allman, Joshua A. Strong, Kevin D. Osborn, and Raymond W. Simmonds. Vacuum-gap capacitors for low-loss superconducting resonant circuits. *IEEE Transactions on Applied Superconductivity*, 19(3):948–952, 2009.

Curriculum Vitae

Personal Details

Name: Indrajeet
Place of Birth: Taoru, Haryana, India
Date of Birth: August 5, 1991
Email: sagar5891indra@gmail.com

Education

Syracuse University

Doctor in Philosophy in Physics
Advisor: Dr. Britton Plourde
Expected graduation date: Aug 2021

Indian Institute of Science Education and Research, Mohali

BS-MS with major in Physics
Graduation date: May 2014

Publications

- Temperature Dependent Non-linear Damping in Palladium Nano-mechanical Resonators, Shelender Kumar, S. Rebari, Satyendra.P. Pal , S.S. Yadav, Abhishek Kumar, A.Aggarwaal, S. Indrajeet, et. al, Nano Letters 21, 7, 2975–2981 (2021).

- Coupling a Superconducting Qubit to a Left-Handed Metamaterial Resonator, S.Indrajeet, H. Wang, et al., Phys. Rev. Applied 14, 064033 (2020).

- Mode Structure in Superconducting Metamaterial Transmission Line Resonators, H. Wang, A.P. Zhuravel, S.Indrajeet, et al., Phys. Rev. Applied 11, 054062 (2019).

- Tunable low temperature dissipation scenarios in palladium nano-mechanical resonators, S.Rebari, Shelender Kumar, S.Indrajeet, et. al, Phys. Review B 95, 214113 (2017).

- Dissipation in palladium nanomechanical resonator at ultra low temperatures, Masters Thesis, Supervisor: Dr. A. Venkatesan , IISER Mohali (2014).